

# Northumbria Research Link

Citation: Omotosho, Emmanuel Olubambi (2023) Studies on dynamic behaviours of magnetic shape memory single crystal NiMnGa alloys for actuator applications. Doctoral thesis, Northumbria University.

This version was downloaded from Northumbria Research Link:  
<https://nrl.northumbria.ac.uk/id/eprint/51631/>

Northumbria University has developed Northumbria Research Link (NRL) to enable users to access the University's research output. Copyright © and moral rights for items on NRL are retained by the individual author(s) and/or other copyright owners. Single copies of full items can be reproduced, displayed or performed, and given to third parties in any format or medium for personal research or study, educational, or not-for-profit purposes without prior permission or charge, provided the authors, title and full bibliographic details are given, as well as a hyperlink and/or URL to the original metadata page. The content must not be changed in any way. Full items must not be sold commercially in any format or medium without formal permission of the copyright holder. The full policy is available online: <http://nrl.northumbria.ac.uk/policies.html>



**Northumbria**  
**University**  
NEWCASTLE

**STUDIES ON DYNAMIC BEHAVIOURS OF MAGNETIC  
SHAPE MEMORY SINGLE CRYSTAL NIMNGA ALLOYS  
FOR ACTUATOR APPLICATIONS**

**Emmanuel Olubambi Omotosho**

**PhD**

**Supervisors**

**Dr. Xue Chen (Principal supervisor)**

**Prof. Ben Xu (2<sup>nd</sup> supervisor)**

**2023**

**STUDIES ON DYNAMIC BEHAVIOURS OF MAGNETIC  
SHAPE MEMORY SINGLE CRYSTAL NIMNGA ALLOYS  
FOR ACTUATOR APPLICATIONS**

**By Emmanuel Olubambi Omotosho**

**A thesis submitted in partial fulfilment of the requirements of the**

**University of Northumbria at Newcastle for the degree of**

**Doctor of Philosophy**

**Research undertaken in the Department of Mechanical and**

**Construction Engineering, Faculty of Engineering and**

**Environment**

**September 2023**

## Abstract

Single crystal NiMnGa alloys present potential applications as sensors and actuators due to their high-frequency response and significant reversible strain. The aim of this dissertation is to study the thermo-magneto-mechanical behaviours of single crystal NiMnGa alloys. In this regard, both experimental and theoretical analysis are performed.

Firstly, the effects of thermo-magnetic loading conditions on the high-frequency, long-term ( $>100$  s, achieving steady state), dynamic behaviour of single crystal NiMnGa alloys that are driven by cyclic magnetic fields are studied. A dynamic model that incorporates both magnetic-field-induced martensite reorientation and temperature-driven martensitic phase transformation simulates the material's dynamic behaviour at various degrees of ambient heat-transfer, ambient temperature, applied magnetic field frequency, and amplitude. An analytical expression of the material's long-term steady-state behaviour (i.e., stable strain amplitude and temperature) as a function of the thermal environment and the magnetic loading circumstances is further developed from the dynamic model. Weak ambient heat transfer, high ambient temperature, and high magnetic field amplitude are found to lead to large net heat generation from dissipative martensite reorientation and thus increase the material's stable temperature, which reduces twinning stress and increases stable strain amplitude.

Secondly, the experimental part presents the temperature-induced phase transformations of single crystal NiMnGa alloys. Two sets of experiments are carried out. At the start of both experiments, the sample is in the state of single martensite variant. For Experiment 1, the sample is heated and when the martensite-to-austenite transformation takes place by the propagation of an austenite-martensite interface (A-M interface), the heat supply is turned off, and the sample temperature drops below the austenite start temperature  $A_s$ . It is observed that the A-M interface continues propagating even below  $A_s$ . Experiment 2 involves cooling of the

sample from above the austenite finish temperature  $A_f$  when the austenite phase has been fully formed in the sample. During cooling when the austenite-to-martensite transformation starts to propagate below the martensite start temperature  $M_s$ , the sample is supplied with heat. It is observed that the sample temperature rises above the  $M_s$  temperature before the A-M interface stops. With these tests, two new critical temperatures are formulated: (1) the austenite stop temperature  $A_{stop}$  from Experiment 1, at which the martensite-to-austenite transformation stops after the heat source is switched off, and (2) the martensite stop temperature  $M_{stop}$  from Experiment 2, at which the austenite-to-martensite transformation stops after the heat supply is turned on. It is found that  $A_{stop}$  is below the  $A_s$  temperature and  $M_{stop}$  is above the  $M_s$  temperature. This new phenomenon happens to be in analogy with the stress-induced phase transformation of shape memory alloys (super-elasticity).

*Keywords:* magnetic shape memory alloys; Ni-Mn-Ga single crystal; thermo-magneto-mechanical behaviours; martensite reorientation; temperature-induced martensitic phase transformation.

## **Acknowledgements**

First and foremost, I would like to thank my PhD advisor, Dr. Xue Chen, for her loving and profound support that she gave to me. There are no words to express how much I am thankful for her support. her care and encouragement were very supportive at time when I felt like giving up. I also want to thank Professor Ben Bin Xu who was greatly helpful in my research.

I would like to express my thanks to the technical staffs, Gavin, Rebecca, Simon, Phil, Sam for their valuable advice and experience and making my research life more enthusiastic and homely. I thank all the members of staff and academics who I have worked with in Northumbria University. I appreciate to Northumbria University for providing me the RDF PhD studentship and the access to research facilities.

I would also like to thank everyone who has been working in the same lab and office with me, for their valuable advice and discussions on my research and study. Furthermore, I would like to express my thanks to the staffs in the lab, workshop for their help. I appreciate the lab facilities and computing resources that are provided by Northumbria University.

Finally, appreciation goes to my wife, Anuoluwapo for her emotional support and encouragement. A special thanks also to my extended families; daddies, mummies, and my siblings for their undying inspiration and support.

## **Dedication**

This thesis work is dedicated to God, the redeemer and saviour of my soul.

## Declaration

I declare that the work contained in this thesis has not been submitted for any other award and that it is all my own work. I also confirm that this work fully acknowledges opinions, ideas and contributions from the work of others.

I confirm that appropriate credit has been given within this thesis where reference has been made to the work of others. The work presented in Chapter 4 has been published in **European Journal of Mechanics - A/Solids** as “*Thermo-magnetic loading effects on high-frequency dynamic behaviour of magnetic shape memory alloys*” by me and other authors.

Any ethical clearance for the research presented in this thesis has been approved. Approval has been sought and granted by the Faculty Ethics Committee on 25-01-2020 with reference no: 21576.

I declare that the Word Count of this Thesis is 22,936 words

Name: Emmanuel Olubambi Omotosho

Date: September 2023



## **Achievements**

### **Journal publications (Q1)**

**Omosho, E. O.**, Qin, Z., Birkett, M., Chen, X., Xu, B., 2022. Thermo-magnetic loading effects on high-frequency dynamic behaviour of magnetic shape memory alloys. *European Journal of Mechanics - A/Solids* 96, 104725.

**Omosho, E. O.**, Chen, X., Xu, B., Kinetics of temperature-induced phase transformations in Ni-Mn-Ga single crystal. (In preparation, plan to submit to *Materials & Design* in 2023).

### **Oral presentations at international conferences**

**Omosho, E. O.**, Xu, B., Chen, X., 2022. Effect of thermo-magnetic loading on high-frequency dynamic behaviour of magnetic shape memory alloys. 18th European Mechanics of Materials Conference (EMMC18), 5<sup>th</sup> April 2022, University of Oxford.

**Omosho, E. O.**, Xu, B., Chen, X., 2021. Effect of temperature changing rate on phase transformation in magnetic shape memory alloy. BSSM 15th International Conference on Advances in Experimental Mechanics, 7<sup>th</sup> September 2021. (Online).

**Omosho, E. O.**, Shyha, I., Chen, X., 2020. Coupling dynamics of magnetic shape memory alloys. 27th Annual CSCST-SCI Conference: Sustainable Energy and Manufacturing the Future, 12<sup>th</sup> September 2020. (Online).

# Table of Contents

Abstract.....	iii
Acknowledgements .....	v
Dedication.....	vi
Declaration .....	vii
Achievements .....	viii
List of Figures.....	xiii
List of Tables.....	xvii
List of nomenclature and abbreviations .....	xviii
1. Introduction .....	1
1.1. Project background.....	1
1.2. Research motivation in ferromagnetic shape memory alloys .....	2
1.2.1. Fundamental behaviour of single crystal Ni-Mn-Ga.....	2
1.2.2. Research challenges for ferromagnetic shape memory alloys .....	3
1.3. Research aim and objectives .....	4
1.3.1. Aim.....	4
1.3.2. Objectives .....	5
1.4. Thesis outline .....	5
2. Literature Review .....	7
2.1. Shape Memory Effect.....	7
2.1.1. One-way shape memory effect.....	8
2.1.2. Two-way shape memory effect (reversible SME).....	8
2.1.3. Super-elasticity (SE).....	8
2.2. Shape Memory Material.....	9
2.3. Characteristics of Ni-Mn-Ga alloys .....	20
2.3.1. Crystal structure.....	21
2.3.2. Martensite reorientation.....	24

2.3.3.	Phase transformation .....	27
2.3.4.	Frequency response .....	29
2.3.5.	Ambient effect .....	30
2.4.	Most recent studies .....	31
2.4.1.	Modelling of single crystal NiMnGa alloys .....	32
2.4.2.	Kinetics of temperature-induced phase transformation in NiMnGa alloys 37	
2.5.	Chapter conclusion .....	39
3.	Methodology and Preliminary Study .....	41
3.1.	Theoretical modelling of the magnetic actuator based on magnetic-shape- memory alloys.....	41
3.1.1.	Constitutive model of magnetic shape memory alloys.....	42
3.1.2.	Mass-spring model of the MSMA dynamic system .....	44
3.1.3.	Programme flowchart .....	46
3.2.	Experimental setup for studies on the kinetics of temperature-driven phase transformation.....	46
3.2.1.	Crystal structure.....	47
3.2.2.	Digital Image Correlation (DIC) technique.....	48
3.2.3.	Equipment properties and calibration.....	50
3.2.4.	Experimental setup design.....	52
3.2.5.	Preliminary test.....	56
3.2.6.	Differential scanning calorimetry (DSC) analysis .....	60
3.3.	Chapter conclusion .....	61
4.	Thermo-magnetic loading effects on the high-frequency dynamic behaviour of single crystal NiMnGa alloys.....	62
4.1.	Introduction .....	62
4.2.	Dynamic model .....	63
4.2.1.	Magnetic analysis .....	63

4.2.2.	Mechanical analysis.....	64
4.2.3.	Thermal analysis.....	66
4.3.	Thermo-magnetic loading effects.....	68
4.3.1.	Ambient heat-transfer condition.....	68
4.3.2.	Ambient temperature .....	73
4.3.3.	Magnetic field amplitude.....	75
4.3.4.	Magnetic field frequency.....	76
4.4.	Discussions.....	78
4.4.1.	Austenite state .....	80
4.4.2.	Mixture state where martensite and austenite phases coexist .....	81
4.4.3.	Martensite state.....	83
4.5.	Chapter conclusion.....	89
5.	Kinetics of temperature-induced phase transformations in Ni-Mn-Ga single crystal	91
5.1.	Introduction .....	91
5.2.	Material properties and experimental setup .....	92
5.3.	Results and discussions .....	97
5.3.1.	Test I: martensite-to-austenite transformation triggered by heating .....	97
5.3.2.	Test II: Austenite-to-martensite transformation triggered by cooling.....	101
5.3.3.	Kinetics of phase transformation.....	105
5.4.	Chapter conclusion.....	110
6.	Overall conclusion.....	111
7.	Future work.....	112
	References .....	114
	Appendix .....	121
	Appendix A. Measurement of characteristic phase transformation temperatures of Ni-Mn-Ga single crystal.....	121

Appendix B. Sample temperature measured by thermocouples at different locations .....	128
Appendix C. Experimental data for temperature-induced phase transformation in Ni- Mn-Ga single crystal.....	129
Appendix D. Algorithmic chart.....	135

## List of Figures

Figure 2-1. Three different shape memory effects (Tarng et al., 2019) .....	7
Figure 2-2. Schematic diagram of the lattice structure of the Ni-Mn-Ga single crystal: the martensite variants and the austenite phase. $a_0$ denotes the length of the austenite lattice; $a$ and $c$ represent the lengths of the long (a-axis) and short (c-axis) axis of the martensite lattice. $A_s$ is the austenite start temperature, $A_f$ is the austenite finish temperature, $M_s$ is the martensite start temperature, and $M_f$ is the martensite finish temperature. ....	22
Figure 2-3. Schematic diagram of martensite reorientation through the application of cyclic magnetic field and compressive stress .....	24
Figure 2-4. Stress-induced martensite reorientation. M1 and M2 are martensite variants 1 and 2, respectively. ....	25
Figure 2-5. Magnetic-field-induced martensite reorientation. M1 and M2 are martensite variants 1 and 2, respectively.....	26
Figure 2-6. Frequency response of magnetic memory alloys actuated by magnetic field in a short time ( $< 5$ s). ....	30
Figure 2-7. Summary of the thermo-mechanical responses of the MSMA at different levels of ambient airflow velocity as reported by (Zhang et al., 2018a). ....	31
Figure 3-1. Linear phase transformation kinetics (Chen and He, 2020) .....	43
Figure 3-2. Schematic diagram of a dynamic system (Chen and He, 2020) .....	44
Figure 3-3. MATLAB programme flowchart (Chen and He, 2020) .....	46
Figure 3-4. X-ray diffraction pattern of single crystal $\text{Ni}_{50}\text{Mn}_{28}\text{Ga}_{22}$ .....	47
Figure 3-5. Principles of DIC Analysis .....	48
Figure 3-6. A-M interface and compatible martensite fine-twins on the $x$ - $y$ plane from the compatibility analysis in Zhang et al. (2018b).....	49
Figure 3-7. Typical strain maps from DIC. ....	50

Figure 3-8. Design of experimental setup. ....	53
Figure 3-9. (a): ABAQUS simulation model. (b): Sample temperatures at different levels of sample holder height (simulation): Temperature increase rates of 3, 4, 5, 6, 7 and 8mm are 3.73, 2.94, 2.53, 2.16, 1.91 and 1.70 °C, respectively. ....	54
Figure 3-10. Schematic diagram of experimental setup 1.....	55
Figure 3-11. Schematic diagram of experimental setup 2.....	56
Figure 3-12. A typical heating by the input voltage of 4 V using experiment setup 1...57	
Figure 3-13. A typical heating process by the input voltage of 4 V using experiment setup 2.....	58
Figure 3-14. A typical strain evolution of experiment 1 with their DIC images.....	59
Figure 3-15. DSC curve for the Ni-Mn-Ga sample at the heating/cooling rate of 2 °C/min. ....	60
Figure 4-1. (a) Schematic diagram of the austenite and the martensite variants of Ni-Mn-Ga magnetic shape memory alloy: cubic austenite lattice and pseudo-tetragonal martensite lattice. (b) Martensite reorientation among three martensite variants (M1, M2, M3) and phase transformation between austenite (A) and martensite (M). ....	62
Figure 4-2. (a) Material's responses to the gradual change of heat relaxation time $t_h$ . (b) Magnified views of stable states. The span of each view is 0.02 s. In order to achieve this, the model in MATLAB is performed at a magnetic field amplitude of 0.78 T, magnetic field frequency of 90 Hz (90Hz frequency denotes that the material's response frequency is twice, i.e., $2 \times 90 = 180$ Hz), and ambient temperature of 20 °C.....	71
Figure 4-3. At various levels of heat relaxation time $t_h$ , the material's stable behaviours (such as stable output strain amplitude and stable temperature) are shown. Martensite state (M), mixture state (M&A), when martensite and austenite coexist, and austenite state (A) are the three zones that correspond to the three material states. The ambient temperature is 20 °C, the	

magnetic field amplitude is 0.78 T, the magnetic field frequency is 90 Hz (making the material's response frequency  $2 \times 90 = 180$  Hz), and all simulations are run under these conditions. .73

Figure 4-4. (a) Responses of the material to a change in ambient temperature  $T_0$  over time. (b) Stable behaviours of the material (stable output strain amplitude, stable temperature) at various ambient temperature levels: martensite state (M), mixture state (M&A) (when martensite and austenite coexist), and austenite state (A) are the three zones that correspond to the three material states. All simulations are run using a magnetic field amplitude of 0.8 T, magnetic field frequency of 90 Hz, and a heat relaxation time of 20 s. So the material response frequency is:  $2 \times 90 = 180$  Hz. ....74

Figure 4-5. (a) Responses of the material to gradual changes in the applied magnetic field amplitude  $\mu_0 H_{amp}$ . (b) Stable behaviours of the material, such as stable output strain amplitude and stable temperature, at various magnetic field amplitude levels. There are two zones that correspond to the martensite state (M) and the mixture state (M&A), where austenite and martensite coexist. The MATLAB simulations are run with the following parameters: a heat relaxation time of 30 s, an ambient temperature of 20 °C, and a magnetic field frequency of 120 Hz. So the material response frequency is:  $2 \times 120 = 240$  Hz.....76

Figure 4-6. (a) Martensite state's responses to the magnetic field frequency's gradual change,  $f_H - I$ : martensite state. (b) The stable behaviours of the material (such as stable output strain amplitude and stable temperature) at various magnetic field frequencies. All simulations are run at an ambient temperature of 20 °C, a magnetic field amplitude of 0.8 T, and a heat relaxation time of 10 s. It should be noted that the material's response frequency is two times the frequency of the applied magnetic field, making the response frequency of the simulated material from 100 Hz to 300 Hz. ....77

Figure 4-7. (a) Materials' reactions to the magnetic field frequency's steady shift,  $f_H - II$ : mixing state. (b) The stable behaviours of the material (such as stable output strain amplitude



and stable temperature) at various magnetic field frequencies. All simulations are run using a 0.8 T magnetic field amplitude, a 40 s heat relaxation time, and a 20 °C ambient temperature. It should be noted that the material's response frequency is two times the frequency of the applied magnetic field, making the response frequency of the simulated material from 100 Hz to 300 Hz.....78

Figure 5-1. Temperature-induced phase transformations in shape memory alloys. Four characteristic temperatures are identified:  $A_s$  (austenite start temperature),  $A_f$  (austenite finish temperature),  $M_s$  (martensite start temperature), and  $M_f$  (martensite finish temperature). .....91

Figure 5-2. Schematic diagram of the austenite and the martensite variants of Ni–Mn–Ga shape memory alloys: pseudo-tetragonal martensite lattice with the long axis of length  $a$  and short axis of length  $c$ , and cubic austenite lattice with length  $a_0$ . .....93

Figure 5-3. Photo of experimental setup. ....95

Figure 5-4. Example of austenite-martensite (A-M) interface identified in DIC images .....96

Figure 5-5. Summary of the measured  $A_s$  (characteristic austenite start temperature),  $A_{stop}$  (austenite stop temperature, only defined in the chapter),  $M_s$  (characteristic martensite start temperature), and  $M_{stop}$  (martensite stop temperature, only defined in the chapter) from all tests. .... 105

Figure 5-6. Schematic diagram of typical stress–strain curve for stress-induced phase transformation in shape memory alloys (super-elasticity)..... 107

Figure 5-7. Average A-M interface motion speed at different levels of the average thermodynamic driving force, which is quantified by the average temperature difference here. .... 109

## List of Tables

Table 2-1. Classification of stimulus responsive materials (adapted from Yahia (2015)) .....	14
Table 2-2. Groups of multi-responsive SMM (adopted from Laitinen et al. (2020)) ....	15
Table 3-1. Temperature measurements from thermocouples and digital thermometer..	52
Table 3-2. Abaqus model parameters .....	53
Table 3-3. Typical phase transformation temperatures at different applied voltages ....	59
Table 4-1. Dimensionless parameters adopted in Chapter 4. ....	88
Table 5-1. A typical example of Test I results: sample is heated to the characteristic austenite start temperature ( $A_s$ ) and then cooled down naturally.....	98
Table 5-2. A typical example of Test II results: sample is cooled down naturally from a temperature around 10 °C higher than the characteristic austenite finish temperature ( $A_f$ ) to the characteristic martensite start temperature ( $M_s$ ), and then the sample is heated.....	102

## List of nomenclature and abbreviations

$a_0$	Magnetic susceptibility of austenite	$6 \times 10^2$ (Heczko, 2005)		$M_S^A$	Saturation magnetization of austenite	$3.9 \times 10^5$ (Heczko, 2005)	$A \cdot m^{-1}$
$a_1$	Magnetic susceptibility of martensite variant 1	0.95 (Heczko, 2005)		$M_S^M$	Saturation magnetization of martensite	$5 \times 10^5$ (Heczko, 2005)	$A \cdot m^{-1}$
$a_2$	Magnetic susceptibility of martensite variant 2	$5 \times 10^2$ (Heczko, 2005)		$N$	Demagnetization factor	0.55 (calculated using the formula in (Aharoni, 1998))	
$A_f$	Austenite finish temperature		$^{\circ}C$	$R$	Effective radius of MSMAs sample	1.2 (Zhang et al., 2018b)	mm
$A_s$	Austenite start temperature		$^{\circ}C$	$S$	Cross-sectional area of MSMAs sample	6 (Zhang et al., 2018b)	$mm^2$
$A_{stop}$	Austenite stop temperature		$^{\circ}C$	$T$	MSMAs sample's temperature		$^{\circ}C$

$A_s^0$	Austenite start temperature in free state	41.5 (Zhang et al., 2018b)	$^{\circ}\text{C}$	$T_0$	Ambient temperature	$-20 \sim 50$	$^{\circ}\text{C}$
$c$	Damping coefficient	10.1	$\text{kg} \cdot \text{s}^{-1}$	$T_{PT}$	Characteristic phase transformation temperature	39	$^{\circ}\text{C}$
$c_0$	Internal energy difference between austenite and martensite at 0 K	$1.0768 \times 10^7$	$\text{J} \cdot \text{m}^{-3}$	$t_h$	Characteristic heat relaxation time	$0.1 \sim 1000$	s
$c_1$	Entropy difference between austenite and martensite at 0 K	$3.4534 \times 10^4$	$\text{J} \cdot \text{m}^{-3} \cdot \text{K}^{-1}$	$z_0$	Volume fraction of austenite	Initial value $z_0^{(0)} = 0$	
$E$	Young's modulus of MSMAs sample	50 from mechanical test in (Chen et al., 2013)	GPa	$z_1$	Volume fraction of martensite variant 1	Initial value $z_1^{(0)} = 1$	

$f_H$	Applied magnetic field frequency	50 ~ 150	Hz	$z_2$	Volume fraction of martensite variant 2	Initial value $z_2^{(0)} = 0$	
$H$	Magnitude of the magnetic field strength of MSMA		Hz	$z_{01}$	volume-fraction transformation between austenite and martensite variant 1	Initial value of 0	
$ H $	Absolute value of $H$		Hz	$z_{02}$	volume-fraction transformation between austenite and martensite variant 2	Initial value of 0	
$k$	Interaction parameter accounting for incompatibility among martensite variants	$1.09 \times 10^3$	$J \cdot m^{-3}$	$z_{12}$	volume-fraction transformation between martensite variant 1 and 2	Initial value of 0	
$k_0$	Interaction parameter accounting for incompatibility	$2.3810 \times 10^4$	$J \cdot m^{-3}$	$\varepsilon_0$	Strain change due to martensite reorientation	5.8 (Heczko, 2005)	%

		between austenite and martensite					
$k_s$	Spring stiffness	5.5 from tests in (Zhang et al., 2018a)	$\text{N} \cdot \text{mm}^{-1}$	$\varepsilon_a$	Strain change along long axis of pseudo- tetragonal martensite during martensitic phase transformation	1.9 (Heczko et al., 2002)	%
$L$	Linear coefficient	$1 \times 10^4$	$\text{m} \cdot \text{s} \cdot \text{kg}^{-1}$	$\varepsilon_c$	Strain change along short axis of pseudo- tetragonal martensite during martensitic phase transformation	3.9 (Heczko, 2002)	%
$l_0$	Initial length of MSMAs sample	15 (Zhang et al., 2018a)	mm	$\lambda$	Specific heat per unit volume	$4 \times 10^6$ (Zhang et al., 2018a)	$\text{J} \cdot \text{m}^{-3} \cdot \text{K}^{-1}$
$m$	Mass of the moving parts in MSMAs dynamic system	22.5 from tests in (Zhang et al., 2018a)	g	$\mu_0$	Vacuum permeability	$4\pi \times 10^{-7}$	$\text{T} \cdot \text{m} \cdot \text{A}^{-1}$

$M_f$	Martensite finish temperature	°C	$\mu_0 H_{amp}^{app}$	Amplitude of applied magnetic field	0 T ~ 1 T	T
$M_s$	Martensite start temperature	°C	$\sigma_0$	Initial compressive stress	0.4 (Zhang et al., 2018a)	MPa
$M_{stop}$	Martensite stop temperature	°C	$\sigma_{tw}^{eff}$	Effective twinning stress of martensite reorientation		Pa

# 1. Introduction

## 1.1. Project background

Single crystal Ni-Mn-Ga is a type of shape memory material (SMM). SMMs are smart materials that can change their shape, size, and/or properties in response to external stimuli, such as mechanical stress, temperature variation, heat flux, electric field, and magnetic field (Wei et al., 1998). These alterations to stimuli can be programmed and made specific. Even though these materials have been discovered for a long time, the term "smart" was only first used in the USA in the 1960s when the NiTi shape memory alloy was commercialised by the Naval Ordnance Laboratory (Melton, 1990; Chu et al., 2007; Wang et al., 1965). The material is called "smart" because it responds to its surroundings, and the material's response can be any reaction that manifests as a change in volume, colour, viscosity, etc. (Talbot, 2003). These changes to the external stimuli can be programmed to be reversible. Another term used to describe the degree of "smartness" of the material is "I.Q.". This is the measure of the level of responsiveness and agility of the SMMs to external stimuli (Cao et al., 1999). The types and responsiveness of materials are categorised into two different levels: single-phase materials and composite materials. The single-phase materials' responses like the piezo-electric, electrostrictive, and magneto-strictive materials, are rather low but possess the ability to respond naturally to stimuli. The composite materials are made by mixing different materials, usually to form an alloy. An example is the ferromagnetic shape memory alloys (FSMAs).

The ability of a material to regain its original shape following a pseudo-plastic deformation (so-called shape memory) is what attracts the engineering industry to FSMAs (Duerig et al., 1990). In various FSMAs, the external stimuli for shape change and recovery can vary. For example, when exposed to temperature variation, the traditional NiTi shape memory alloy can deform as a result of temperature-induced martensitic phase transformation



(Liu et al., 1997). The single crystal Ni-Mn-Ga alloy, which is one of the most studied FSMAs, exhibits large strain change (6% ~ 10%) when exposed to a magnetic field (Liu et al., 1997). This type of SMMs is beginning to place significant interest due to this large recoverable deformation when actuated (Zhang et al., 2018a). This large recoverable deformation, which is a unique behaviour, is referred to as the shape memory effect.

## **1.2. Research motivation in ferromagnetic shape memory alloys**

The research motivation in ferromagnetic shape memory alloys (FSMAs) stems from their ability to exhibit the shape memory effect under the magnetic field, where the material can regain its original shape after undergoing a pseudo-plastic deformation. The single crystal Ni-Mn-Ga alloy, in particular, has been considerably studied due to its large recoverable deformation when exposed to a high-frequency magnetic field. This unique behaviour has sparked significant interest in the material for high-speed actuator applications, which are of particular interest in this thesis.

### **1.2.1. Fundamental behaviour of single crystal Ni-Mn-Ga**

The martensite-to-austenite transition in single crystal Ni-Mn-Ga, a reversible solid-state phase transformation that occurs in response to change in temperature, is currently under study. This transition is essential for the control of the following properties:

- Firstly, the martensite-to-austenite transition allows Ni-Mn-Ga alloys to exhibit a shape memory effect, where they can recover their original shape by a change in temperature (at a temperature below  $A_s$ ). This is because the austenite phase is stable at a higher temperature than the martensite phase, and transition between phases is possible with changes in temperature or/and magnetic field.
- Secondly, the martensite-to-austenite transition in single crystal Ni-Mn-Ga is often accompanied by a magnetic field-induced strain (MFIS) effect. This means that the

application of a magnetic field during phase transition can cause a change in the shape of the material. This effect is particularly useful in applications where precise control over the shape of a material is required, such as in micro-electromechanical systems (MEMS) or actuators.

- Finally, the martensite-to-austenite transition is also important for the magnetic properties of FSMAs. In the austenite phase, FSMAs exhibit a high magnetisation, which makes them useful in applications such as magnetic sensors and actuators. The ability to control the transition between the martensite and austenite phases allows for precise control over the magnetic properties of the material.

In conclusion, single crystal Ni-Mn-Ga alloy, a type of FSMAs, is a promising material for actuator and sensor applications due to its unique properties, such as the super-elastic behaviour and the magnetic field-induced strain.

### **1.2.2. Research challenges for ferromagnetic shape memory alloys**

The research challenges in studying ferromagnetic shape memory alloys (FSMAs) include understanding the underlying mechanisms that govern their shape memory effect and identifying ways to optimise their performance for system applications. Researchers are currently investigating the thermo-magneto-mechanical behaviours of FSMAs through a series of experimental studies. These studies have contributed to the development of numerous material models; however, the functionalities are still in early stages and not able to fully describe and simulate the material's behaviour across a wide range of scales, from microscopic to macroscopic. For instance, the effect of various degrees of ambient heat-transfer and ambient temperature on dynamic behaviours of single crystal NiMnGa alloys are still not fully understood. In addition, the kinetics of phase transformation by heating and cooling the Ni-Mn-Ga single crystal samples have not been thoroughly studied. These highlight the need for further research to better understand the behaviour of NiMnGa under different conditions.

Understanding these behaviours will further enhance the material's control and response to external stimuli, and thus harness the unique potential properties of FSMAs to create advanced systems (such as actuators) with improved functionality and reliability. The use of experimental studies that will improve the development of universal models are essential for gaining a deeper understanding. A review of current studies relevant to this PhD research area, covering both experimental findings and material models, are presented in Chapter 2, which will also identify knowledge gaps.

### **1.3. Research aim and objectives**

This thesis is devoted to exploring the dynamic behaviours of Ni-Mn-Ga alloys for the potential actuator application. Existing dynamic model is used to simulate the coupled thermo-magneto-mechanical behaviours of Ni-Mn-Ga single crystals actuated by a high-frequency magnetic field. However, the impact of the ambient heat-transfer condition, ambient temperature, magnetic field amplitude, and magnetic field frequency on the rate of heat generation during the magnetic actuation and their impact on the martensite-to-austenite transformation have not yet been studied in the literature, according to the author's best knowledge. Moreover, the studies on the kinetics of temperature-induced phase transformation occurring during the magnetic actuation, where samples of Ni-Mn-Ga single crystals are heated and cooled, are still limited in the literature. This thesis will fulfil these knowledge gaps. Detailed aim and objectives are given below.

#### **1.3.1. Aim**

The research aim of this project is to study the dynamic behaviours of single crystal Ni-Mn-Ga magnetic shape memory alloys for actuator applications. To reach this ultimate aim, systematic objectives are listed as follows.

### 1.3.2. Objectives

- Improving existing dynamic model to study the coupled thermo-magneto-mechanical behaviours of Ni-Mn-Ga single crystals;
- Investigating the impact of ambient heat-transfer condition, ambient temperature, magnetic field amplitude, and magnetic field frequency on the rate of heat generation during magnetic actuation and their effect on the martensite-to-austenite transformation in Ni-Mn-Ga single crystals;
- Conducting experimental studies to explore the kinetics of temperature-induced phase transformation by heating and cooling Ni-Mn-Ga single crystal samples.

## 1.4. Thesis outline

The whole thesis is organised as follows:

Chapter 1: This chapter introduces the PhD project, outlining its objectives and providing general background of ferromagnetic shape memory alloys.

Chapter 2: This chapter presents a literature review that focuses on the kinetics of temperature-induced phase transformation and material models for single crystal NiMnGa alloys.

Chapter 3: This chapter describes the research methodology used in the thesis, including material model and experimental techniques.

Chapter 4: This chapter is dedicated to exploring the effects of thermo-magnetic loading conditions on the high-frequency dynamic behaviour of magnetic shape memory NiMnGa alloys. A dynamic model that incorporates both magnetic-field-induced martensite reorientation and temperature-driven martensitic phase transformation is used to simulate the material's behaviour under various ambient temperatures, ambient heat-transfer conditions, applied magnetic field frequencies, and amplitudes. New analytical expressions of the material's behaviour in the steady state are developed.

Chapter 5: This chapter presents an experimental study on the kinetics of temperature-induced phase transformation in Ni-Mn-Ga single crystals. The samples are heated or cooled to induce phase transformation, and the velocity of the austenite-martensite interface motion is measured. The thermodynamic driving force is also calculated to relate to the measured velocity.

Chapter 6: This chapter provides an overall conclusion that summarises the main findings and implications of the research.

Chapter 7: This chapter outlines potential future work to further advance the understanding of magnetic shape memory alloys and their applications.

## 2. Literature Review

### 2.1. Shape Memory Effect

Shape memory effect (SME) is the ability of a material to recover to its original shape after being deformed. For instance, Ferromagnetic Shape Memory Alloys (FSMAs) demonstrate SME through large extensional 10% strain (Bruno et al., 2017; Haldar and Lagoudas, 2018; Pagounis et al., 2014; Seiner et al., 2014; Sratongon et al., 2019; Uchimali and Vedantam, 2021; Yu et al., 2018). The SME varies in various SMMs and Mohd Jani et al. (2014) has categorised the SME into three types of memory characteristics as shown in Figure 2-1:

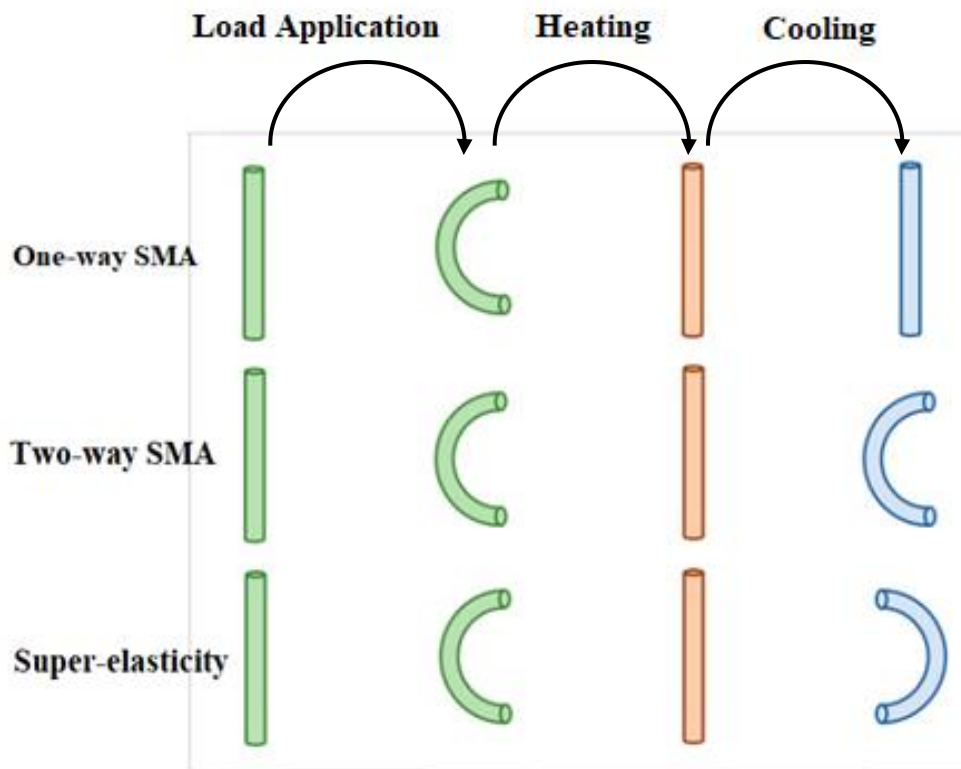


Figure 2-1. Three different shape memory effects (Tarng et al., 2019)

### **2.1.1. One-way shape memory effect**

The one-way shape memory alloy (OWSMA) maintains its distorted state even after the application and removal of an external stimulus; nevertheless, it is able to return to its initial shape when exposed to some form of desired stimuli, such as heating in Figure 2-1.

### **2.1.2. Two-way shape memory effect (reversible SME)**

In addition to the behaviour of the one-way effect, a two-way SMA (TWSMA) can remember its shape at both different temperatures. However, the TWSMA finds less application commercially due to the ‘training’ requirements to achieve reversible behaviour, and it tends to deteriorate quickly, especially when actuated at high temperatures (Wang et al., 1965; Laitinen et al., 2020). Therefore, OWSMA on some occasions, provides a more reliable and economical solution (Wen et al., 2018). Various training methods have been proposed, and two of them are: spontaneous and external load-assisted induction.

### **2.1.3. Super-elasticity (SE)**

The super-elastic (also called pseudo-elastic) material can revert to its original shape after the initially applied external stimulus is removed, without the need for any external intervention or activation (Mohd Jani et al., 2014). Many of these types of materials undergo phase transformation between austenitic and martensitic phases during the shape change (Figure 2-1). Shape memory alloys (e.g., Ni-Ti and Ni-Mn-Ga) are under this category of materials and have drawn immense attention in the last few decades. Also, many industrial applications have been found for them (Wuttig et al., 2001; Faran and Shilo, 2016; Likhachev and Ullakko, 2000).

The ability of FSMA's such as single crystal Ni-Mn-Ga to act as both sensors and actuators is another reason why it is attracting a lot of attention. Although, its use can be limited because of its nonlinear behaviour such as martensitic phase transformation caused by high temperature (Tan and Elahinia, 2008). Moreover, the maximal deformation produced is

significantly greater than that of conventional magneto-strictive materials (Techapiesanchaenroj et al., 2009). Since heating and cooling are slower than applying a magnetic field, magnetic control provides a faster reaction time than some other conventional temperature-driven shape memory alloys (Pirge et al., 2004). In summary, single crystal Ni-Mn-Ga combines both the property of magneto-strictive materials (i.e., high frequency response) and conventional shape memory effects (i.e., strain values of up to 10%). In order for the use in engineering applications to be seamless, there is a need to further understand the behaviour to accelerate their use.

## **2.2. Shape Memory Material**

The shape memory effect (SME) is a phenomenon in which a material recovers to its original size and shape when exposed to a certain characteristic stimulus. According to the actuating stimulus, shape memory materials (SMMs) can be classified into the following categories (Sarvari et al., 2020; Wang et al., 2022):

- Photo-responsive shape memory materials

The photo-responsive SMMs such as Titanium nitride (TiN), Zinc oxide (ZnO) and Copper oxide (CuO) are a type of smart materials that responds to light and undergoes a photo-mechanical deformation that is uniform and isotropic (Iqbal and Samiullah, 2013; Herath et al., 2020). The reaction to light is enabled by optical radiation of wavelength between 1 and 10<sup>6</sup> nm (Herath et al., 2020), and such mechanical deformation is reversible. According to Snyder and Tong (2005), it is possible to create light-activated SMMs that can be deformed at room temperature: retaining the deformed shape by photo-irradiation using one wavelength and returning to the original shape by irradiation with a different wavelength due to the reversible crosslinking process by irradiation. The photo-responsive SMMs are very attractive for medical/biological applications. According to Brill et al. (2022), they can provide contact-free,



precise, and physical behaviour, and the stimuli can be introduced remotely (i.e., without any physical contact with the photo-responsive material), without necessarily being invasive or harmful.

- Thermo-responsive shape memory materials

Many temperature-responsive materials with high IQ smartness can display abrupt and dramatic shifts in their physical properties when exposed to temperature variations (Purwar and Sachan, 2020). The thermo-responsive shape memory materials (e.g., polycaprolactone, polyurethane, polylactic acid) exhibit reversible shape change by temperature variations. For heating-induced shape change and recovery, several cutting-edge heating techniques have been proposed, including Joule heating, inductive heating, light heating, and radio heating (Kim and Matsunaga, 2017).

- Chemo-responsive shape memory materials

Some smart materials have the ability to change their shapes when the appropriate chemicals are applied. If the volume change is small, this property is referred to as the chemo-responsive shape memory (e.g., Tungsten oxide). Most of the time, there is no chemical reaction involved, and by removing the chemical, the materials can return to their original chemical and physical states. According to Lu et al. (2013), the thermo-responsive shape memory behaviour and the chemo-responsive shape memory behaviour in SMMs are similar to each other. However, in a more general sense, the method to trigger the chemo-responsive shape memory behaviour is through the reduction of the interactive forces among macromolecules, while for the thermo-responsive shape memory behaviour, the material's temperature is changed to reach the characteristic phase transformation temperatures. By softening, swelling, or dissolving the chemo-responsive SMMs (e.g., certain polymers), the

interactive forces among macromolecules will inductively lower the polymer's glass transition temperature and increase the flexibility of the macromolecular chains (Lu et al., 2013).

- Magneto-responsive shape memory materials

Magneto-responsive shape memory materials often contain or be composed of, ferromagnetic structures, such as metallic particles and nanowires (e.g., Fe, Co, and Ni, or compounds of these elements), and magnetic particles such as neodymium-iron-boron (NdFeB) (Bril et al., 2022). When under an applied magnetic field, they can exhibit large macroscopic shape changes. There are two types of magneto-responsive shape memory materials (Ze et al., 2019; Thévenot et al., 2013). The first type includes materials that will exhibit strain change as long as they are exposed to the magnetic field. When the magnetic field is removed, the materials will return to their original shapes. This type of magneto-responsive SMMs has applications in fast, tuneable, and reversible modulations. The second type will retain the strain change even when the magnetic field is removed.

- Mechano-responsive shape memory materials

The mechano-responsive shape memory materials can respond to an external stimulus by producing a mechanical response (e.g., piezoelectric poly(vinylidene difluoride)). The characteristics of these materials are dependent on their capacity to maintain their physical integrity and to withstand the accumulation of defects, which would typically induce fatigue after prolonged exposure to external stimuli (Naumov et al., 2015). This kind of material has engineering applications as mechanical sensors to detect damage caused by local stress changes (Kim et al., 2016; McFadden and Robb, 2019).

- Electro-responsive shape memory materials

The electro-responsive shape memory materials demonstrate a change either in their sizes or in their shapes when stimulated by an electric field (e.g., silver nanowire (Ag NW)).

Actuators (Wang et al., 2016) and sensors (Keplinger et al., 2010; Shahinpoor, 2015) are the two major areas in which this sort of material is utilised the most frequently. When subjected to an external electrical field, an electro-responsive material will undergo a significant amount of deformation, which is one of the defining characteristics of this type of material. Currently, the major challenge with electro-responsive SMMs is their poor mechanical strength, such as brittleness (Bril et al., 2022).

- Moisture-responsive shape memory materials

The moisture-responsive shape memory materials react to changes in humidity through the presence of hydrophilic functional groups in the material. The most common example of the moisture-responsive SMMs is hydrogels, which are water-swollen polymers exhibiting significant volume change in response to humidity change. Poly(ethylene glycol), 2-hydroxyethyl methacrylate, polyacrylamide, N-isopropyl acrylamide, chitosan, and hyaluronic acid gels are among the commonly utilised hydrogels (Aswathy et al., 2020). Hydrogels will expand (swell) in the presence of a solvent and contract (de-swell) as a result of the evaporation of the solvent. It has been reported that hydrogels are capable of swelling more than 300 times their dry weight (Fonteno and Bilderback, 1993), which thus provides a simple technique to generate significant changes in volume. However, it can be tricky to produce local swelling and shrinkage, making spatiotemporal alterations problematic (Bril et al., 2022). The challenge also exists in the design as it involves sophisticated 3D polymer structures (Ge et al., 2021). In addition, it is also reported that moisture-responsive SMMs exhibit shape transformation only in the dry state (Ge et al. (2021)).

- pH-responsive shape memory materials

The pH-responsive shape memory materials change in size or shape when the pH of the environment changes. The material must have acidic or basic motifs, such as the carboxylic

group (-COOH), the amine group (-NH<sub>2</sub>), and an atom of hydrogen (-H) (Bril et al., 2022), that can react to the environment's change in pH. There are both natural and artificial pH-sensitive materials due to the natural existence of these functional groups. Hyaluronic acid, dextran, alginic acid, poly(acrylic acid), and poly(L-glutamic acid) are typical examples of pH-responsive SMMs (Li et al., 2015). And their applications are found in biomaterials, smart actuators and sensors (Bril et al., 2022).

- Multi-responsive shape memory materials

Multi-responsive SMMs are materials that can respond to multiple stimuli to produce a pseudo-elastic behaviour. Multi-responsive SMMs can react in a variety of ways, making them feasible to precision and specificity, causing a wide range of material responses and behaviours. The introduction of shape memory materials with multiple memory effects and the investigation of their responses can be of great use in the engineering industry. Multi-responsive SMMs are of great importance in our world today as they have begun to replace conventional systems that use and depend on multiple components to function. Multi-responsive SMMs are capable of producing strain changes and behaving as a single active component, and in many cases, their behaviours do not cause the material to age or fatigue as it takes place in conventional systems.

For a brief summary, Table 2-1 presents the classification of stimulus-responsive materials, and Table 2-2 summarises typical groups of multi-responsive SMMs that are currently researched and newly developed.

Table 2-1. Classification of stimulus responsive materials (adapted from Yahia (2015))

<b>Response</b> <b>Stimulus</b>	<b>Thermal</b>	<b>Photo</b>	<b>Electrical</b>	<b>Magnetic</b>	<b>Mechanical</b>	<b>Chemical</b>	<b>Moisture</b>
<b>Photo</b>	Photothermic	Photostrictive, Photoluminescent, Photo-chromic	Photo-conductive, Photovoltaic	Opto-magnetic	Opto-mechanical  Mechano-chromic	Photo-chemical  Photo-catalyst	
<b>Thermal</b>		Thermo-chromic  Thermo-luminescent	Thermo-electric  Super-conductor, Pyroelectric	Curie point	Shape-memory		
<b>Chemical</b>	Endo-thermic	Litmus, Chemochromic	Magnetochemical		Chemo-mechanical	Catalysis	
<b>Magnetic</b>	Magneto-thermal,	Magneto-optic Piezo-chromic	Magneto-electronics,		Magnetostrictive Magneto-rheological		
<b>Mechanical</b>	Magnetocaloric	Rheo-chromic	Piezoresistive, Piezoelectric	Magnetostrictive			

<b>Electrical</b>	Peltier	Electrochromic	Magneto-	Piezo-electric	Electro-
		Electro-optic	electronics	Electro-rheological,	chemical
<b>Moisture</b>				Electrostrictive	Electrolysis
	Hydro-thermal			Hydrodynamic	

Table 2-2. Groups of multi-responsive SMM (adopted from Laitinen et al. (2020))

<b>Group</b>	<b>Stimulus</b>	<b>Response</b>	<b>Examples of materials</b>
<b>Chemo mechanical polymers</b>	Chemical reaction	Strain	Hydrogels, Shape Memory Polymer.
<b>Electroactive polymers</b>	Electric current	Strain	Polyvinylidene fluoride ((C <sub>2</sub> H <sub>2</sub> F <sub>2</sub> ) <sub>n</sub> ), Silicon rubber and Polyurethane, Polyacetylene.
<b>Electrostrictive</b>	Electric current	Strain	Lead magnesium niobate (MgNb <sub>2</sub> O <sub>9</sub> Pb <sub>3</sub> ), Lead Lanthanum Zirconate Titanate (Pb <sub>0.92</sub> La <sub>0.08</sub> Zr <sub>0.52</sub> Ti <sub>0.48</sub> O <sub>3</sub> ), Barium Titanate (BaTiO <sub>3</sub> ).

<b>Magnetostrictive</b>	Magnetic field	Strain	Cobalt, Cobalt Ferrite ( $\text{CoO} \cdot \text{Fe}_2\text{O}_3$ ), Terfenol-D ( $\text{Tb}_x\text{Dy}_{1-x}\text{Fe}_2$ ), Galfenol ( $\text{Fe}_x\text{Ga}_{1-x}$ ), Alfer ( $\text{Fe}_x\text{Al}_{1-x}$ ), Metglas ( $\text{Fe}_{81}\text{Si}_{3.5}\text{B}_{13.5}\text{C}_2$ ).
<b>Photostrictive</b>	Light	Strain	PLZT (Lead-Lanthanum-Zirconate-Titanate), Antimony Sulphoiodide/Stibnite ( $\text{SbSI}$ ), Bismuth Ferrite ( $\text{BiFeO}_3$ ), Lead Titanate ( $\text{PbTiO}_3$ ).
<b>Shape memory alloys</b>	Shape memory effect temperature	Strain	Ni-Ti, Fe-Mn-Si, Cu-Zn-Al, Cu-Al-Ni
<b>Shape memory polymer</b>	Shape memory effect temperature, electric current, light	Strain	Polyurethane, Polyvinylchloride, Cinnamic acid, Cinnamylidene acetic acid.
<b>Magnetic shape memory alloys</b>	Magnetic shape memory effect, magnetic field	Strain	Fe-Pd, Ni-Mn-Ga, Ni-Mn-Al
<b>Magnetoelectric</b>	Magnetic field	Electric current	Multiferroics, Chromia ( $\text{Cr}_2\text{O}_3$ ), Bismuth ferrite ( $\text{BiFeO}_3$ )
	Electric current	Magnetic field	
<b>Photovoltaic</b>	Light	Electric current	Silicon, Gallium arsenide ( $\text{GaAs}$ ), Copper Indium Gallium (di)Selenide (CIGS), Titanium dioxide ( $\text{TiO}_2$ ), Cadmium telluride ( $\text{CdTe}$ ).

<b>Magnetocaloric</b>	Magnetic field	Temperature change	Iron rhodium (FeRh), Ni-Co-Mn-Sn alloy, NdCo <sub>5</sub> , NdCo <sub>5</sub> H <sub>3</sub> .
<b>Pyroelectric</b>	Temperature	Electric current	Triglycine sulfate (C <sub>6</sub> H <sub>17</sub> N <sub>3</sub> O <sub>10</sub> S), Lead zirconium titanate (PZT), Polyvinylidene difluoride (-(C <sub>2</sub> H <sub>2</sub> F <sub>2</sub> ) <sub>n</sub> -).
<b>Piezoelectric</b>	Mechanical stress	Electric current	Aluminium phosphate (Al(PO <sub>4</sub> )), Gallium arsenide (GaAs), and Barium titanate (BaTiO <sub>3</sub> ).
<b>Piezoresistive</b>	Mechanical stress	Electrical resistance	Germanium, Polycrystalline silicon, Silicon carbide (SiC)
<b>Thermoelectric</b>	Temperature	Electric current	Silicon/SiGe, Bismuth telluride ((Bi <sub>2</sub> Te <sub>3</sub> )), Lead tellurides (PbTe), SrTiO <sub>3</sub> , Cuprokalinitite (CuCr <sub>2</sub> S <sub>4</sub> ).
<b>Electro-chromic/Electro reflective</b>	Electric current	Colour/optical property change	Viologens ((C <sub>5</sub> H <sub>4</sub> NR) <sub>2</sub> <sup>n+</sup> ), Tungsten oxide (WO <sub>3</sub> ), Niobium oxide (Nb <sub>2</sub> O <sub>5</sub> )
<b>Chemo-chromic</b>	Chemical reaction	Colour change	Tungsten oxide (WO <sub>3</sub> ), Molybdenum trioxide (MoO <sub>3</sub> ), Lanthanide Hydrides (LnH <sub>2</sub> ).
<b>Photo-chromic/photo-refractive</b>	Light	Colour change	Silver chloride (AgCl), Zinc halides (ZnCl <sub>2</sub> , ZnBr <sub>2</sub> , ZnI <sub>2</sub> ), Yttrium ox hydride (YHO), and Barium titanate (BaTiO <sub>3</sub> ).



<b>Thermo-chromic</b>	Temperature	Colour change	Titanium dioxide (TiO <sub>2</sub> ), Zinc oxide (ZnO), Indium(III) oxide (In <sub>2</sub> O <sub>3</sub> ), Lead(II) oxide (PbO), Vanadium(IV) oxide (VO <sub>2</sub> ), Titanium(IV) nitrate (Ti(NO <sub>3</sub> ) <sub>4</sub> ).
<b>Mechano-chromic</b>	Mechanical stress	Colour change	Zinc oxide (ZnO), Silicon dioxide (SiO <sub>2</sub> ), Polydiacetylenes (PDAs), Spiropyans, Strontium Aluminate (Sr <sub>3</sub> Al <sub>2</sub> O <sub>6</sub> ).
<b>Photoluminescent</b>	Light	Light emission	Zinc oxide (ZnO), Strontium aluminate (SrAl <sub>2</sub> O <sub>4</sub> ), Zinc sulphide (ZnS).
<b>Thermoluminescent</b>	Temperature	Light emission	Lithium tetraborate (Li <sub>2</sub> B <sub>4</sub> O <sub>7</sub> ), Beryllium oxide (BeO), Lithium fluoride (LiF), Calcium sulphate (CaSO <sub>4</sub> ), and Calcium fluoride (CaF <sub>2</sub> ).
<b>Electroluminescent</b>	Electric current	Light emission	Zinc sulphide (ZnS) doped with terbium (Tb) or manganese, zinc sulphide doped with copper, Gallium nitride (GaN), and Gallium arsenide (GaAs).

**Mechanoluminescent**

Mechanical stress	Light emission	Zinc sulphide (ZnS) doped with copper, Zinc sulphide (ZnS) doped with manganese, Strontium aluminate (SrAl <sub>2</sub> O <sub>4</sub> ).
-------------------	----------------	---

### 2.3. Characteristics of Ni-Mn-Ga alloys

The single crystal Ni-Mn-Ga belongs to the group of magnetic shape memory alloys (MSMAs) whose strain change can be controlled by applying magnetic field. The last few decades have seen a significant rise in the research on shape memory alloys (SMAs), and several new classes have been identified (Buschow, 2013). The SMAs are divided into three types, which are the NiTi, Cu and Fe-based shape memory alloys (Jain et al., 2013; Jetty et al., 2013; Sabahi et al., 2020). NiTi-based SMAs are the industrially preferred choice for biomedical applications. The functional qualities that make them superior for these applications are biocompatibility and resistance to fatigue, although patients' allergies to nickel continue to be a concern (Sabahi et al., 2020). Fe-based SMAs (such as FeMnSi) and Cu-based SMAs (such as CuZnAl and CuAlNi) are commercially available and relatively inexpensive. But their poor thermo-mechanical performance, poor stability, and low corrosion resistance limit their industrial applications. With the increased demand for materials with unique performances, and in particular, materials that can exhibit behaviours with rapid response, magnetic shape memory alloys (MSMAs) are becoming more desirable. They can be actuated by a magnetic field at high frequencies ( $> 100$  Hz) and provide a rapid, reversible strain change (Bruno et al., 2017; Haldar and Lagoudas, 2018; Pagounis et al., 2014; Seiner et al., 2014; Sratongon et al., 2019; Uchimali and Vedantam, 2021; Yu et al., 2018).

Single crystal  $\text{Ni}_2\text{MnGa}$  has aroused a broad range of scientific interest since Ullakko et al. initially reported a 0.2% magnetic-field-induced strain by twin-boundary motion in  $\text{Ni}_2\text{MnGa}$  single crystal in 1996 (Ullakko et al., 1996). The single crystal Ni-Mn-Ga MSMAs are the ones that have been investigated the most thoroughly due to their low twinning stress and high magneto-crystalline anisotropy energy (Chmielus et al., 2011; Faran and Shilo, 2012; Nath and Phanikumar, 2015; Pagounis et al., 2014, 2015). Numerous experimental investigations on the behaviours of Ni-Mn-Ga single crystals under magneto-mechanically

coupled loading conditions have been carried out during the past 20 years. It is demonstrated that there are two potential methods for producing a significant amount of reversible strain in Ni-Mn-Ga single crystals: via a magnetic field and mechanical stress. In the early 2000s, Murray et al. (2000) obtained the nearly maximum theoretical strain of 6% in Ni<sub>2</sub>MnGa single crystal at room temperature, which opened up the possibility for engineering applications.

Ni-Mn-Ga single crystals exhibit a large reversible magnetic-field-induced strain (up to 10%), but they are exceedingly fragile and expensive. The low martensitic transformation temperature of these materials may present another challenge for the potential application as actuators working at room temperature since the strain change due to phase transformation will take place above room temperature (Panda et al., 2008).

According to Liu et al. (2003), the research of MSMA's utilising various preparation methods has undergone a paradigm change. To create Ni-Mn-Ga MSMA's in the form of ribbons, the quick solidification approach using the melt spinning technique has been investigated. It has been discovered that this method, which is often used in metallic glass preparations, works well for freezing the Heusler Ni-Mn-Ga stoichiometry to L21 austenitic (cubic) structure (Liu et al., 2003; Panda et al., 2008).

The focus of this thesis is on the two fundamental features of single crystal Ni-Mn-Ga MSMA's, i.e., magnetic-field-induced martensite reorientation and temperature-induced phase transformation, which are important for potential engineering actuators applications. The detailed characteristics about single crystal NiMnGa alloys are presented below.

### **2.3.1. Crystal structure**

Ni-Mn-Ga single crystals exhibit two distinct phases when subjected to different temperatures: the cubic austenite phase when the temperature is high and the martensite phase when the temperature is low. Ni-Mn-Ga single crystals can have three different martensitic phases: the tetragonal five-layered modulated martensite (5M), the orthorhombic seven-layered

modulated martensite (7M), and the tetragonal non-modulated martensite (NMT) depending on the temperature and material composition (Martynov and Kokorin, 1992). Both the 5M and 7M martensitic phases have shown magnetic-field-induced strain, with 5M martensite being the most extensively researched martensitic phase in the literature. There are three martensite variants for the cubic to tetragonal (5M) martensitic transition in Ni-Mn-Ga: M1, M2, and M3 with their short axes ( $c$ -axis) corresponding to the  $x$ -,  $y$ -, and  $z$ -coordinates of the parent austenite lattice, respectively (Tickle et al., 1999; Webster et al., 1984; Zasimchuk et al., 1990) (see Figure 2-2). Let  $a_0$  denote the edge length of the austenite phase, while the lengths of the long and short edges of the martensite phase are denoted as  $a$  and  $c$ . These lattice parameters are found to be:  $a_0 \approx 0.584$  nm,  $a \approx 0.595$  nm, and  $c \approx 0.561$  nm (Heczko et al., 2002; Straka et al., 2008).

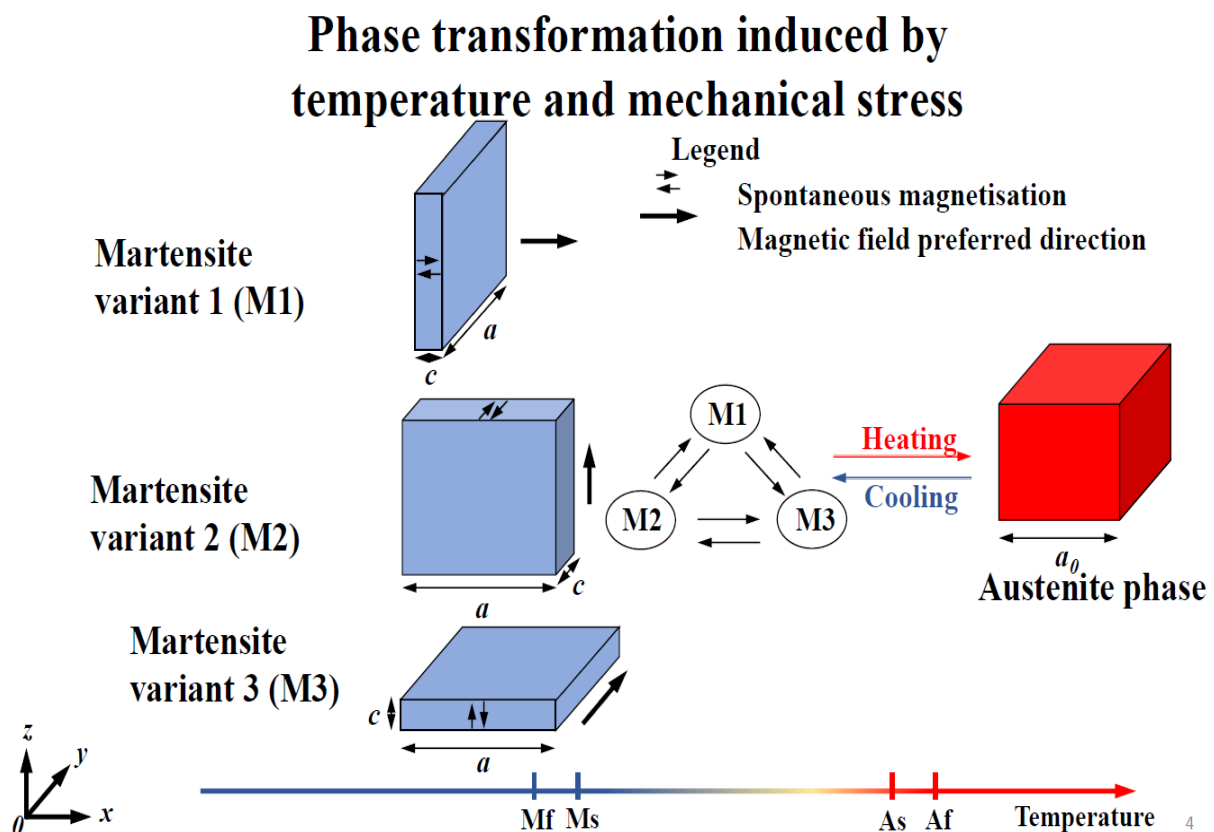


Figure 2-2. Schematic diagram of the lattice structure of the Ni-Mn-Ga single crystal: the martensite variants and the austenite phase.  $a_0$  denotes the length of the austenite lattice;  $a$  and  $c$  represent the lengths of the long ( $a$ -axis) and short ( $c$ -axis) axis of the martensite lattice.  $A_s$  is the austenite start temperature,  $A_f$  is the austenite finish temperature,  $M_s$  is the martensite start temperature, and  $M_f$  is the martensite finish temperature.

The physical mechanism behind the strain change of Ni-Mn-Ga single crystals under a magnetic field is the magnetic-field-induced martensite reorientation (i.e., variant switching): the martensite variant with short crystallographic *c*-axis (also the axis of easy magnetisation) along the applied magnetic field grows at the expense of other variants. The martensite reorientation in MSMA takes place by the twin boundary motion (Figure 2-3). A twin boundary is a single atomic plane that separates two neighbouring martensite variants (Pascan et al., 2015). Two types of twin boundaries are observed in MSMA, i.e., Type I and Type II (Müllner, 2019). The Type I twin is known to have relatively higher motion friction with the twinning stress (regarded as friction) ranging from 0.8 to 1.4 MPa. In comparison, the Type II twin has relatively lower motion friction, with the twinning stress ranging from 0.05 to 0.3 MPa (Pascan et al., 2015). It is reported that the twinning stress plays an important role in the property of Heusler alloys, as it determines the required level of applied stress or magnetic field to induce a twin variant rearrangement (Sozinov et al., 2002). The twinning stress of Type I twin is decreased as the temperature of MSMA increases, and lower twinning stress can result in a higher strain in the MSMA (Karaca et al., 2006; Jugo et al., 2018; Zhang et al., 2018). Another important parameter to quantify the performances of MSMA under the magnetic field is the blocking stress, i.e., the applied stress under which the magnetic field cannot induce martensite reorientation (Murray et al., 2000).

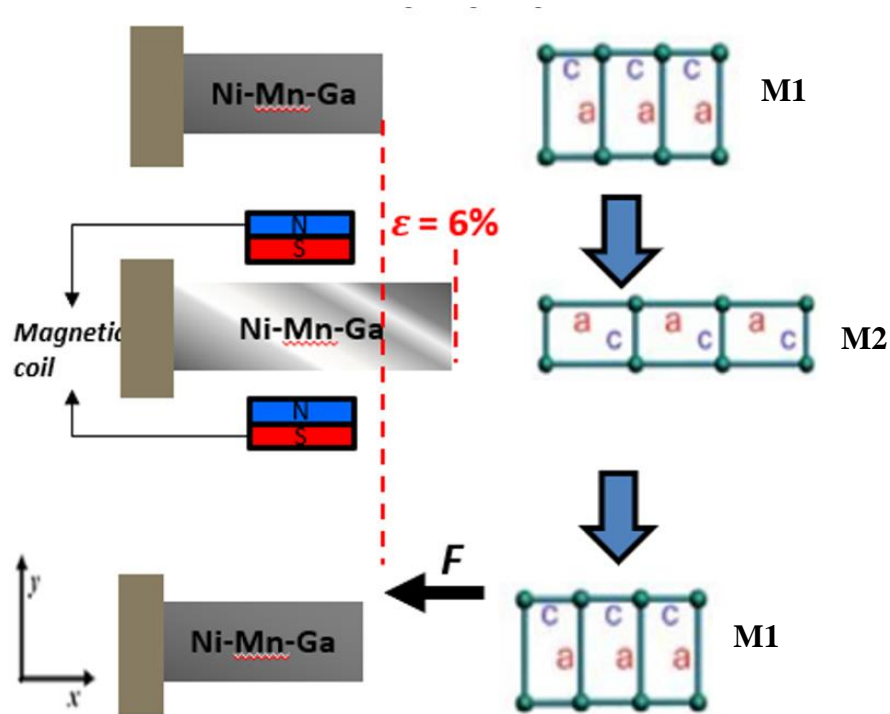


Figure 2-3. Schematic diagram of martensite reorientation through the application of cyclic magnetic field and compressive stress

### 2.3.2. Martensite reorientation

Martensite reorientation is the process by which one martensite variant switches to another. Two types of external loads can induce the martensite reorientation in Ni-Mn-Ga single crystals, i.e., mechanical stress and magnetic field.

- Stress-induced martensite reorientation

The stress-induced martensite reorientation in Ni-Mn-Ga single crystals can be shown in Figure 2-4. The material is under a constant magnetic field when a compressive stress is applied. At the beginning of the mechanical loading (Point A in Figure 2-4), the material is in the initial state of single martensite variant 1. When the applied compressive stress is large enough (Point B), the martensite reorientation from variant 1 to variant 2 is triggered. So, variant 2 nucleates and expands at the expense of variant 1 (from Point B to Point C in Figure 2-4). Finally, the material is in the state of pure variant 2 with a maximum strain change of 6% at Point C in Figure 2-4. According to the degree of tetragonality of the martensitic phase, the

maximum strain change of Ni-Mn-Ga single crystals due to martensite reorientation can theoretically be estimated by:  $\left|1 - \frac{a}{c}\right|$ , with  $a$  and  $c$  being the lattice parameters of the tetragonal martensitic phase in Figure 2-2. With  $a \approx 0.595$  nm and  $c \approx 0.561$  nm (Heczko et al., 2002; Straka et al., 2008), we have:  $\left|1 - \frac{a}{c}\right| \approx 6\%$ . When the compressive stress is released, the reverse martensite reorientation from variant 2 to variant 1 takes place (Point D to Point A), and the strain recovers to 0 at the end since the material returns to the initial state of martensite variant 1.

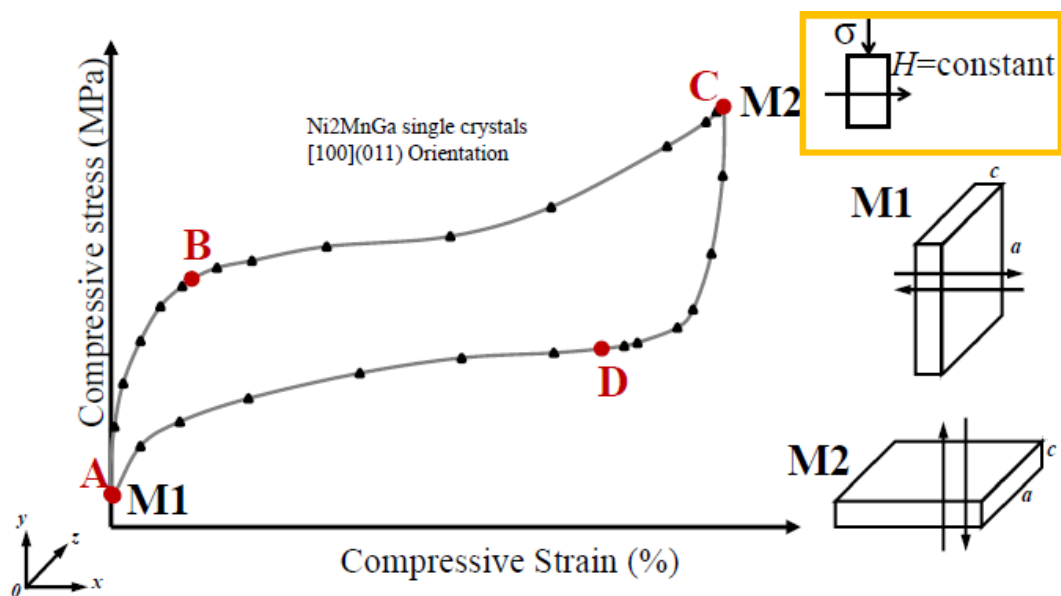


Figure 2-4. Stress-induced martensite reorientation. M1 and M2 are martensite variants 1 and 2, respectively.

- Magnetic field-induced (MFI) martensite reorientation

Under constant compressive stress, a magnetic field is applied to the material. At the beginning of magnetic loading, the material is in the initial state of martensite variant 2 with a short  $c$ -axis along the constant compressive stress (Point A in Figure 2-5). With the increase of the magnetic field, the strain remains unchanged until Point B, where the martensite reorientation from variant 2 to variant 1 (with the easy magnetisation axis ( $c$ -axis) along the applied magnetic field) is triggered. With the nucleation and growth of variant 1, the strain increases (Point B to Point C in Figure 2-5) and finally saturates at a certain level (Point D).



When the magnetic field is released, the reverse martensite reorientation from variant 1 to variant 2 is triggered (Point E to Point F in Figure 2-5), and the strain is partially or fully recovered depending on the level of the constant compressive stress.

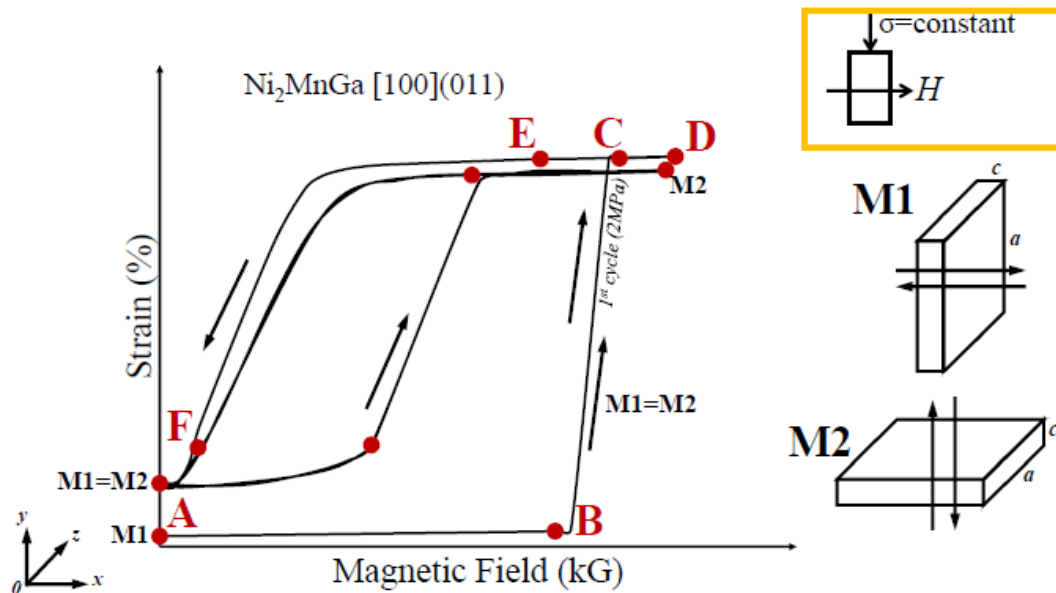


Figure 2-5. Magnetic-field-induced martensite reorientation. M1 and M2 are martensite variants 1 and 2, respectively.

With the combination of stress-induced and magnetic-field-induced martensite reorientations, a cyclic reversible martensite reorientation can be produced (see Figure 2-3). A sample of Ni-Mn-Ga single crystals is in the initial state of single martensite variant M1 with its short  $c$ -axis along the  $x$ -coordinate. Then a magnetic field along the  $y$ -coordinate is applied. When the magnetic field is low, the sample does not undergo any strain change. As the magnetic field is increased to a certain threshold, the magnetic-field-induced martensite reorientation from M1 to M2 (Figure 2-3) will begin. The threshold magnetic field can be estimated by the reorientation criterion:  $\sigma_{mag}(H) \geq \sigma_{comp} + \sigma_{tw}$ , where  $\sigma_{mag}$  is the effective magneto-stress depending on the magnetic field  $H$ ,  $\sigma_{comp}$  is the compressive stress and  $\sigma_{tw}$  is the twinning stress (Heczko and Straka, 2004; Straka et al., 2006). With the continuous increase of the magnetic field, finally, the sample will be in the state of pure martensite M2 with a significant deformation strain of around 6% along the  $x$ -coordinate (Figure 2-3). While the

magnetic field is removed, the sample does not automatically return to its initial shape. In order to obtain the reversible martensite reorientation after the magnetic field is removed, compressive stress along the  $x$ -coordinate must be applied. When the criterion for the reverse martensite reorientation, i.e.,  $\sigma_{comp} \geq \sigma_{tw}$  (Heczko and Straka, 2004; Straka et al., 2006, Zhang, 2018), is satisfied, the stress-induced martensite reorientation from M2 to M1 will take place, and the sample will recover to its initial shape, as shown in Figure 2-3.

### 2.3.3. Phase transformation

Phase transformation between austenite and martensite in magnetic shape memory alloys can be induced by temperature change (thermo-induced phase transformation (Webster et al., 1984; Guilemany and Fernández, 1994)), mechanical stress (stress-induced phase transformation (Karaca et al., 2012; Kim et al., 2006)), and magnetic field (Heczko et al., 2002; Karaca et al., 2007).

- Thermally induced phase transformation

The phase transformation between austenite and martensite phases in shape memory alloys can be induced by temperature variation. When the material in the initial state of martensite is heated to the austenite start temperature  $A_s$ , the martensite-to-austenite transformation is triggered, and the transformation will take place until the material is fully transformed to the austenite phase at the austenite finish temperature  $A_f$ . When the material is cooled down from  $A_f$  temperature to the martensite start temperature  $M_s$ , the austenite-to-martensite transformation is triggered, and the transformation is completed at the martensite finish temperature  $M_f$ . Phase transformation in shape memory alloys usually takes place through two stages: (1) the new phase nucleation and (2) propagation/growth of the new phase (Wang and Du, 2019).

The essential characteristic of shape memory alloys is the ability of the various martensite variants to revert to their original shapes in the austenite phase upon heating without causing a macroscopic shape change (Yang et al., 2019), a phenomenon is known as the *one-way shape memory effect* (see details in Section 2.1.1). During the cooling-induced martensitic phase transformation, shape memory alloys can exhibit a phenomenon called self-accommodation, where multiple martensite variants nucleate in order to reduce the elastic strain energy (Bhattacharya, 1992; Miyazaki et al., 1989). The *two-way shape memory effect* behaviour of shape memory alloys can also be exhibited through the temperature-induced phase transformation, where the material transforms between the austenite phase and martensite phase of certain martensite variants. Although the two-way shape memory effect is not a feature of shape memory alloys by nature, it can be achieved through thermo-mechanical training (Guilemany and Fernández, 1994; Lahoz and Puértolas, 2004; Masdeu et al., 2021). The large strain of the martensite phase during the cyclic mechanical loadings can create flaws or dislocations in the material. These flaws or dislocations are maintained during heating, and they will help create the same martensite microstructure (i.e., same martensite variants) upon cooling, which will result in a significant strain change (LExcellent et al., 2000).

- Mechanically induced phase transformation

The stress-induced martensitic transformation plays a significant role in the shape memory effect in MSMA, and it is the basic property behind the cyclic behaviour of the martensite reorientation, as shown in Figure 2-2. However, the “pseudo-elasticity” behaviour of the MSMA occurs only at temperatures below a critical temperature called austenite start temperature ( $A_s$ ). With the temperature above austenite start temperature ( $A_s$ ), the variant microstructure becomes a cubic structure; therefore, no strain change can occur (Figure 2-2).

- Magnetically induced phase transformation

The magnetic-field-induced phase transformation is associated with the magneto-caloric effect. This effect can be used to attain extremely low temperatures, as well as the ranges used in common refrigerators (Bin et al., 2010). This presents a potential application of MSMA as a refrigerator (Qian et al., 2018; Bin et al., 2010). The drawback of implementing MSMA as a refrigerator is the relatively high magnetic field ( $> 5$  T) required to trigger the phase transformation (Heczko et al., 2016). Researchers (e.g., Karaca et al., 2007) have proposed to solve this limitation by using stress-assisted magnetic-field-induced phase transformation. Results demonstrate that Ni-Mn-Ga MSMA can undergo magnetic-field-induced phase transformation under low field magnitudes and that the transformation is repeatable under cyclic fields (Karaca et al., 2007).

#### **2.3.4. Frequency response**

It is demonstrated by Techapiesanchaenkiy et al. (2009) that Ni-Mn-Ga MSMA can be actuated by a magnetic field at different frequencies in a short time ( $< 5$  s). As the frequency of the applied magnetic field continues to increase, the strain of MSMA will peak at a maximum value (resonance), as shown in Figure 2-6.

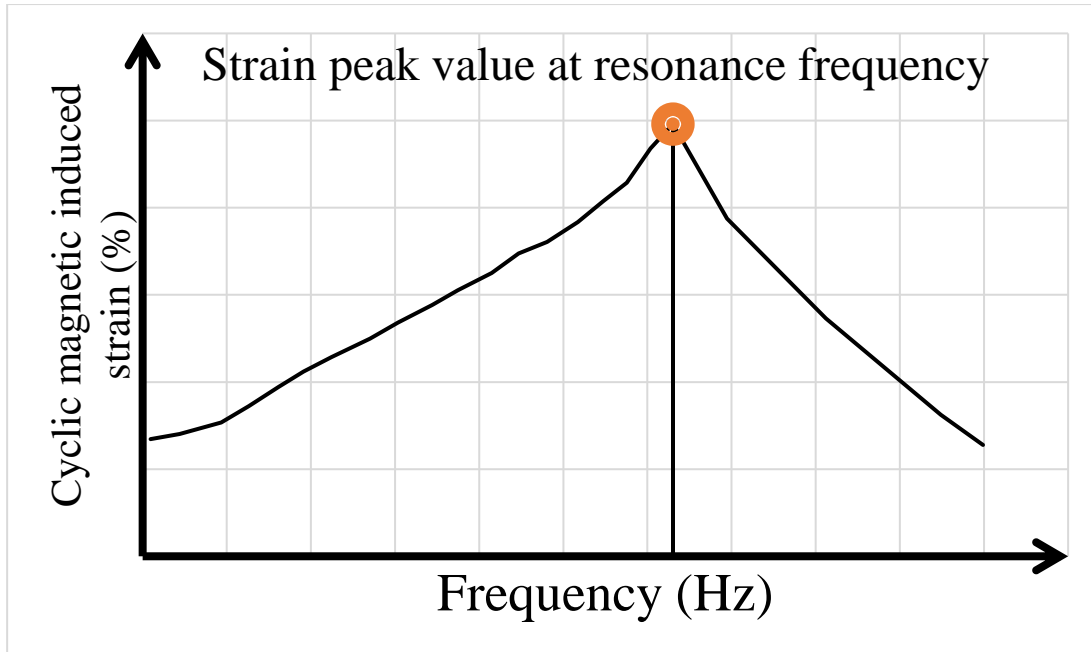


Figure 2-6. Frequency response of magnetic memory alloys actuated by magnetic field in a short time (< 5 s).

### 2.3.5. Ambient effect

It is reported that when Ni-Mn-Ga MSMA are actuated by a cyclic magnetic field for a long time (> 100 s), the accumulated heat from the dissipative martensite reorientation process can result in a significant temperature rise in the material, which has to be controlled because it can hinder the material's performance if its temperature reaches the austenite start temperature  $A_s$  (Pascan et al., 2015). With the appropriate ambient heat transfer condition, such temperature rise of MSMA under a cyclic magnetic field can be controlled (Jugo et al., 2018), as seen in Figure 2-7. A non-monotonic strain evolution with the ambient heat transfer condition in MSMA is also observed (Zhang et al., 2018a), as shown in Figure 2-7.

As demonstrated by Zhang et al. (2018b), in the dynamic test of Ni-Mn-Ga MSMA at still air (i.e., weakest ambient heat transfer condition, Point A to B in Figure 2-7), the material's strain increases rapidly. As the material temperature approaches the phase transformation temperature (Point B in Figure 2-7), strain suddenly drops due to the martensite-to-austenite

transformation. By improving the ambient heat transfer condition through the increase in the ambient air velocity, the material temperature decreases, and its strain increases.

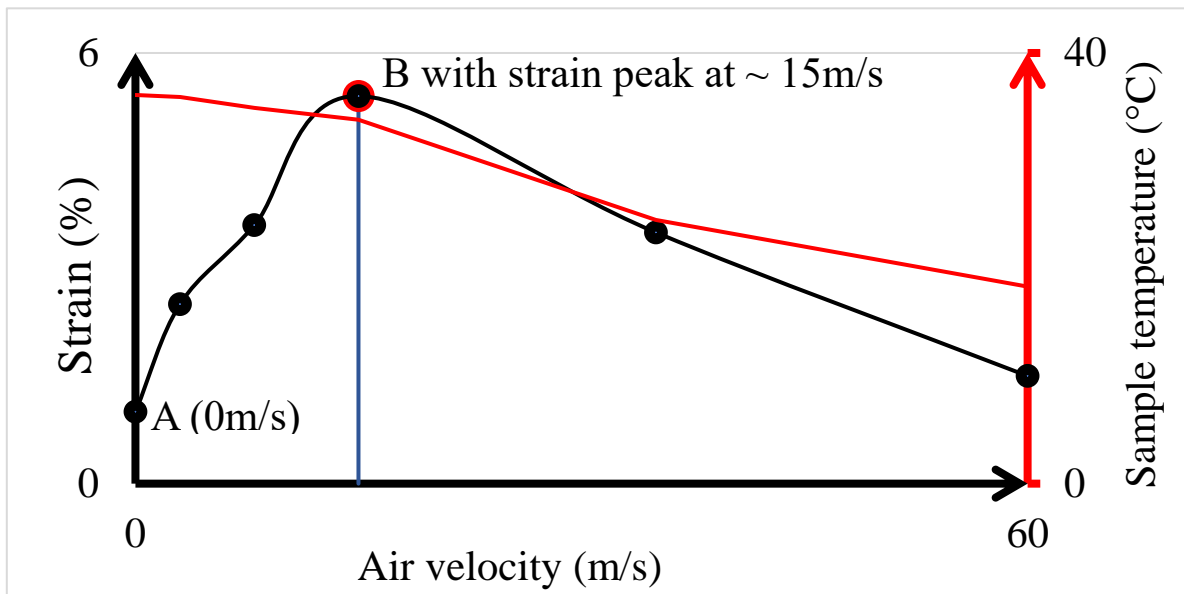


Figure 2-7. Summary of the thermo-mechanical responses of the MSMA at different levels of ambient airflow velocity as reported by (Zhang et al., 2018a).

## 2.4. Most recent studies

As the use of Ni-Mn-Ga alloys in engineering applications, particularly as an actuator, is increasing, there is a need for research to understand the dynamic behaviour of the material. While researchers have previously focused on the quasi-static behaviour of single crystal Ni-Mn-Ga, it has become necessary to investigate the kinetics of phase transformation in the material and its behaviour under high frequency dynamic loadings. Currently, the experimental studies in the literatures are used to develop material models, where researchers can gain important insights into the thermo-magneto-mechanical properties of single-crystalline Ni-Mn-Ga alloys under dynamic loadings, which will aid in the design of NiMnGa-based devices and systems.

### **2.4.1. Modelling of single crystal NiMnGa alloys**

There are several material models of single crystal NiMnGa developed, that are mathematical representations describing the relationship between the material's mechanical response and the external stimuli that it is subjected to (Akintunde et al., 2019). These models are important for understanding the behaviour of the material and predicting its response under different conditions. One common type of material model for NiMnGa is based on the Landau theory of phase transitions (Yu et al., 2020). This model uses a free energy function to describe the relationship between the martensitic and austenitic phases of the material, as well as the effect of external stimuli such as stress and magnetic fields on the phase transformation (Malik et al., 2013). The model can be used to predict the stress-strain behaviour of the material, as well as its magnetic properties.

Another type of material model for NiMnGa is based on micromechanical considerations, which take into account the microstructural features of the material, such as twin boundaries and dislocations (Zhu and Dui, 2007). These models can be used to predict the stress-strain response of the material under different loading conditions and the effect of microstructural features on the material's behaviour.

Recently, machine-learning approaches have been applied to develop data-driven material models of NiMnGa (Fuhg and Bouklas, 2022; Paranjape et al., 2021). These models can be trained on large datasets of experimental data and can accurately predict the material's behaviour under a wide range of conditions. The advantage of data-driven models is that they can capture complex behaviour that may be difficult to describe using traditional physics-based models.

Overall, material models of NiMnGa are important tools for understanding and predicting the behaviour of NiMnGa, and they have important applications in the design and

optimisation of NiMnGa-based devices and systems. The recent material models in the literature related to this study are as follows.

He et al. (2011) present two ways for obtaining magnetic-field induced variant switching: changing the magnitude of a magnetic field with a fixed direction (non-rotating field) and changing the magnetic-field direction with a fixed magnitude (rotating magnetic field). However, the working stress is limited by a small blocking stress (<10 MPa depending on the magnetic anisotropic energy), over which the magnetic field-induced strain (MFIS) is prohibited. Furthermore, based on a 2D energy model on the variant switching, He et al. demonstrate that only the difference between the two stresses (mechanical and actuating/working stress) is limited by the magnetic anisotropic energy and the hysteretic effect—non-zero twinning stress. He et al. also proposes a simple energy model for the 5M (five-layered modulated) martensite variant switching in Ni-Mn-Ga. It compares the energies of the two variants (I and II) under two compressive stresses and a magnetic field and draws phase diagrams to study the variant switching in different loading paths. The energy of each variant (which is assumed to consist of a single magnetic domain) includes the mechanical potential  $E_{mech}$  and the magnetic energy  $E_{mag}$  (Zeeman energy and the magnetic anisotropic energy).

He et al. (2012) presented the 3D criteria of reversible strain, which were seldom reported at the time. The paper extends their earlier energy analysis in He et al. (2011) to study switching among all three tetragonal martensite variants under 3D magneto-mechanical cyclic loadings. The mechanical and magnetic energies of the three tetragonal martensite variants are formulated and compared to determine the energy preference of the variants under 3D magneto-mechanical loadings. A phase diagram is also used to study various 3D cyclic loadings, and the general criteria for obtaining the reversible strain are formulated. The phase diagram consists of stable regions (where only one variant can exist) and meta-stable regions



(where the variant state depends on loading history). The research also focuses on the stable regions of the phase diagrams to derive simple criteria for obtaining reversible strain. It is observed that as the martensite variants are tetragonal, two or more material parameters would be needed to characterise the anisotropic magnetic energy. The energy formulation presented is complex, but it is still useful to study the hysteretic martensite reorientation. The paper concludes that a non-rotating magnetic field cannot induce reversible strain, but uniaxial mechanical stress can. The criteria derived in this paper are sufficient conditions for obtaining reversible strain.

Chen et al. (2014) propose a thermodynamics model to describe the martensite reorientations among the three (5M) tetragonal variants in Ni–Mn–Ga single crystals under 3D magneto-mechanical loading conditions. The model is built within the framework of generalised standard materials with internal constraints and is incorporated into finite element analysis to simulate the samples' behaviours under various loading conditions. It is further used to predict the nonlinear bending behaviours of MSMA beams under mechanical loading and magnetic loading, and the sample-geometry effect and material anisotropic effect are studied. The developed 3D constitutive model of martensite reorientation in MSMA is within the framework of thermodynamics of irreversible processes with internal variables. This model is able to describe all the existing magneto-mechanical behaviours at the time and is validated by existing experiments in the literature. It is also incorporated into finite element analysis and is used to predict the nonlinear bending behaviours of MSMA beams induced by mechanical stress and a non-uniform magnetic field. The sample-geometry effect and the material anisotropic effect are systematically studied and found to be important when designing the MSMA-based bending actuators. However, the nucleation of the twin interface during reorientation is not studied.

Wang and Du (2019) address the issue of predicting the nucleation of twin interfaces in the variant reorientation process. To predict the nucleation of twin interfaces in single-crystalline NiMnGa alloys, a valuable scheme is put forth. Some typical loading conditions are taken into consideration, and the results of numerical simulation are presented, showing a good consistency with the published experimental results, to show the effectiveness of this scheme. Analysing the evolution characteristics of the configurational force also reveals the mechanism of the twin interface nucleation under various loading conditions. Despite the fact that the model presented in the current paper is only applicable for the purely mechanical loading case, the authors suggest that it is possible to use this for the design of smart devices. The authors also claim that this model can also be applied for the variant reorientations or phase transitions in other single-crystalline SMAs.

Chen and He (2020) improve on Chen et al. (2014)'s previous phase-transformable material model by developing a dynamic model that includes the feedback loop that considers the heat balance, introduces proper kinetics of the temperature-dependent martensite reorientation and phase transformation processes, and takes into account the inertial dynamic effect. The model-based simulation mimics the key characteristics of the experimental phenomena and establishes relationships between macroscopic responses (deformation amplitude and temperature evolution) and microscopic physical causes (the kinetics of martensite reorientation and phase transformation). The developed model was compared with experimental results presented by Zhang et al. (2018a), and observation revealed that the dynamic forward/reverse martensitic phase transformation shows little hysteresis, contrasting to the quasi-static cases. Further examination revealed that the phase transformation, due to the coupling dynamics, leads to sudden changes in both deformation and temperature (i.e., the strain-amplitude drop is accompanied by a temperature drop), which was not accurately measured yet in experimental analysis in the literatures at the time.

Xie (2022) investigated the non-uniform demagnetising field within ferromagnetic shape memory alloy and free space during the martensite reorientation. A finite element method was employed in a two-dimensional setting to save huge storage spaces and computational times. In the simulation, the essence of the magnetic-induced martensite reorientation, magnetisation change and their dependency loading level was represented. The model also illustrates the evolution and interaction of martensite domain structure, magnetic domain structure, magnetic potential and demagnetising field. The model revealed that the local demagnetising field within ferromagnetic shape memory alloy and free space is the key to the local nucleation of a new martensite variant. In addition, the main driving force for local nucleation is different from the driving force of the newly formed and growing martensite variant. In a situation of a high loading level, the restriction of martensite reorientation is attributed to the elastic strain energy, while the uniform magnetisation change is driven by Zeeman energy.

In summary, high-frequency electromagnets capable of producing strong magnetic fields are difficult to design, resulting in most dynamic tests being performed at magnetic fields of 0.3 ~ 0.35 T (Henry et al., 2002; Techapiesancharoenkij et al., 2009), which is half of the magnetic field required to produce full magnetic field-induced strain (MFIS) (Heczko and Straka, 2004). It has been discovered that there exist low mobility Type I twin boundaries and high mobility Type II twin boundaries (Straka et al., 2012; Chulist et al., 2013). Additionally, the temperature increase during dynamic actuation has not been systematically studied (Techapiesancharoenkij et al., 2011), but it is suggested that eddy currents and intrinsic dissipation could increase the temperature of the sample up to the martensite-to-austenite transformation. Due to this problem, actuation times are reduced to a few seconds, and there is no observation of the long-time high-frequency actuation of NiMnGa.

According to the author's best knowledge, there has been no research on the effects of ambient temperature, ambient heat-transfer condition, and magnetic loading conditions on the

long-term ( $>100$  s) high-frequency ( $>100$  Hz) dynamic behaviour of NiMnGa actuated by cyclic magnetic fields. Furthermore, no study has presented an analytical representation of the material's behaviour at the long-time steady state. This is particularly important for understanding and predicting long-term behaviour in the design of NiMnGa-based devices and systems. This highlights the need for further research in this area to better understand the behaviour of MSMA under these conditions.

#### **2.4.2. Kinetics of temperature-induced phase transformation in NiMnGa alloys**

In the kinetics of temperature-induced phase transformation, researchers have found that the transformation of the martensite phase to the austenite phase in NiMnGa is influenced by factors such as temperature, strain, and loading conditions (Heczko et al., 2002). The nucleation and growth of the austenite phase during heating and cooling cycles play a crucial role in determining the shape memory effect and super-elasticity of single crystal NiMnGa. Studies related to the kinetics of temperature-induced phase transformation in NiMnGa MSMA are summarised below.

Techapiesancharoenkij et al. (2009) studied the effect of acoustic energy on the twin-boundary mobility of NiMnGa. An acoustic-assist technique was applied to the actuating MSMA to observe the effect on its performance. The acoustic assistance significantly improves the MFIS response of the MSMA actuator by decreasing the required threshold field by 0.7 kOe and increasing the cyclic MFIS from 1.7% to 3.1% with a magnetic-field amplitude of 3.5 kOe. However, at high driving frequencies, the acoustic-assist effect is negligible to no effect on MSMA. Also, the MFIS response over time is nonharmonic and does not follow the sinusoidal response of the magnetic field drive. The study reveals that an actuating MSMA system can achieve large MFIS at higher frequencies.

Yin et al. (2016) studied the electrical resistance change that occurs in an actuating MSMA. The study introduces a linear actuator that uses the magnetic shape memory (MSM) effect and has a built-in position sensing system that detects changes in electrical resistance based on displacement. This study further presents the correlation between strain and the fine twin structure of the actuator material, as investigated using a scanning electron microscope (SEM) under tensile and compressive loads. Under optimal loading conditions, reversible magneto-strains up to 3.6% are achieved. Position sensing accuracy is estimated to be about 2  $\mu\text{m}$  corresponding to 0.3% of full actuation stroke. A demonstrator for positioning is presented using a closed-loop PID control scheme showing a positioning accuracy of about 0.7%. Finally, with consideration for a linear strain-resistance relationship, this performance is simulated using a thermodynamics-based Gibbs free energy simulation model. With a strong magnetic field, the magneto-resistance effect produces a nonlinear contribution to the magneto-strain-resistance properties close to the ends. This research demonstrated that there exists a correlation between magneto-strain, electrical resistance and external stress in an actuating MSMA.

On the other hand, Zhang et al., in their recent studies (Zhang et al., 2018a, 2018b, 2020), presented a long-term dynamic behaviour (greater than 100s) and, in the process, revealed a new phenomenon. In their studies, it was revealed that the temperature of the NiMnGa can be raised by the accumulated heat from the intrinsic dissipation of the cyclic martensite reorientation brought on by a cyclic magnetic field. Therefore, in the situation when there is a weak ambient heat-transfer condition, the material will begin to undergo a phase change at the austenite start temperature ( $A_s$ ). When the  $A_s$  is reached under weak ambient heat transfer conditions, the martensite-to-austenite transformation can be triggered, which will cause a sudden drop in the material's strain. This indicates that the tetragonal structures in the martensite phase are beginning to change to the cubic structure of the austenite phase.

Overall, these recent experimental works in the literature are able to provide valuable insights into the thermo-magneto-mechanical properties of single-crystalline NiMnGa alloys and can contribute to the development of constitutive models and the design of NiMnGa-based devices and systems. Throughout the literature, the general belief is that without external stress, martensite-to-austenite phase transformation cannot occur below  $A_s$  and austenite-to-martensite phase transformation cannot occur above  $M_s$ . Although, recent studies demonstrate how initial condition of martensite can be activated by a high-frequency magnetic field (Zhang et al., 2018a, 2018b) and the phase transformation is observed to occur at temperatures below  $A_s$  and, in certain cases, even close to  $M_s$ .

According to the author's best knowledge, systematic experiments that investigate the temperature-induced austenite-to-martensite transition above  $M_s$  and the martensite-to-austenite transformation below  $A_s$  have not been conducted. Conducting such experiments could provide important insights into the behaviour of the material under different temperature conditions. Also, understanding these behaviours of the material under these conditions could help in the development of more accurate material models and improve the design and optimisation of NiMnGa-based devices and systems.

## **2.5. Chapter conclusion**

In conclusion, the kinetics of temperature-induced phase transformation in shape memory alloys (SMAs) are influenced by factors such as temperature, strain, and loading conditions. The nucleation and growth of the austenite phase during heating and cooling cycles play a crucial role in determining the shape memory effect and super-elasticity of single crystal NiMnGa. The long-term dynamic behaviour of NiMnGa and the phase change from martensite to austenite have also been studied. However, to the best of the author's best knowledge, the effects of ambient temperature, heat-transfer conditions, and magnetic loading on the long-

term, high-frequency dynamic behaviour of single crystal Ni-Mn-Ga actuated by cyclic magnetic fields remain unexplored. Experimental works in the literature provide valuable insights into the thermo-magneto-mechanical properties of single-crystalline NiMnGa alloys and contribute to the development and the design of NiMnGa-based devices and systems. It is worth noting that recent studies have shown that the phase transformation can occur below the austenite start temperature  $A_s$  and even close to the martensite start temperature  $M_s$  under certain conditions. However, systematic experiments investigating the temperature-induced austenite-to-martensite transition above  $M_s$  and the martensite-to-austenite transformation below  $A_s$  have not been conducted. Conducting such experiments will contribute to the research field by providing important insights into the material's behaviour under different temperature conditions and help improve material models.

### **3. Methodology and Preliminary Study**

#### **3.1. Theoretical modelling of the magnetic actuator based on magnetic-shape-memory alloys.**

Chen and He (2020) present a dynamic model that includes a feedback loop to observe the heat balance (i.e., the heat generated by martensite reorientation, latent heat released/absorbed of the phase transformation and the ambient heat transfer conditions). The dynamic model imitates the experimental phenomena, which provides a further understanding of the macroscopic physical responses (the deformation amplitude and temperature evolution) and the microscopic physical mechanisms (the kinetics of martensite reorientation and phase transformation). The dynamic model in Chen and He (2020) is used to simulate and explore the strain modulation strategies in single crystal Ni-Mn-Ga. However, the research in Chen and He (2020) was previously limited due to its lack of consideration for the effects of fluctuating ambient conditions and the gradual application of varying frequencies and amplitudes of magnetic fields on material's long-term steady-state behaviour. This model now factors in the material's response to diverse levels of ambient heat transfer and to a wide temperature range between  $-20\text{ }^{\circ}\text{C}$  and  $50\text{ }^{\circ}\text{C}$ . It also accounts for the effects of applied magnetic field frequencies ranging from 50 Hz to 150 Hz, and amplitudes spanning from 0 T to 1 T. Incorporating the impact of fluctuating environmental conditions, this refined model more accurately mirrors real-world scenarios where ambient temperatures, ambient heat-transfer conditions and magnetic field variations influence the material's behaviour over time. Therefore, this consideration, added to the model, enhances its predictive accuracy for long-term steady-state behaviour. Furthermore, the model was then used to study and develop analytical expressions for the material's enduring steady-state behaviour, taking into account the added environmental thermal and magnetic loading conditions. Further detailed model improvements are presented



in Sections 4.2 – 4.4. This section briefly presents the theoretical modelling of the dynamic behaviours of magnetic shape memory alloys actuated by a high-frequency magnetic field.

### 3.1.1. Constitutive model of magnetic shape memory alloys

For magnetic shape memory alloys, a constitutive formulation based on free energy is taken into consideration. Internal state variables are also introduced, whose evolutions depict the change among different martensite variants and between the martensite phase and the austenite phase.

The constitutive model covers both processes of martensite reorientation and phase transformation, and the martensite reorientation modelling is based on the previous model presented by Chen et al. (2014). The material's Gibbs free energy  $g$  as a function of the absolute temperature  $T$ , the Cauchy stress tensor  $\underline{\underline{\sigma}}$ , the internal magnetic field strength vector  $\underline{H}$ , and the internal state variables (i.e., volume fraction  $z_0$  of austenite and the volume fractions  $z_1$ ,  $z_2$ , and  $z_3$  of the three pseudo-tetragonal 5M martensite variants) are written as:

$$g\left(T, \underline{\underline{\sigma}}, \underline{H}, z_0, z_1, z_2, z_3\right) = g_{therm} + g_{mec} + g_{mag} + g_{int} \quad (3.1)$$

where  $g_{therm}$  is the thermal energy,  $g_{mec}$  is the mechanical energy,  $g_{mag}$  is the magnetic energy and  $g_{int}$  is the interaction energy. The constitutive relations can be obtained from the Gibbs free energy  $g$  as:

- Stress-strain relation

$$\underline{\underline{\varepsilon}} = -\frac{\delta g}{\delta \underline{\underline{\sigma}}} \quad (3.2)$$

where  $\underline{\underline{\varepsilon}}$  is the strain change during thermal-mechanical loadings.

- Magnetisation-magnetic field relation

$$|M| = -\frac{1}{\mu_0} \frac{\delta g}{\delta |H|} \quad (3.3)$$

where  $|M|$  is the magnitude of magnetisation,  $\mu_0$  is the vacuum permeability,  $|H|$  is the magnitude of the magnetic field strength.

- Thermodynamic forces for martensite reorientation

$$A_{i \leftrightarrow j} = \left( -\frac{\delta g}{\delta z_j} \right) - \left( -\frac{\delta g}{\delta z_i} \right) \quad (3.4)$$

where  $A_{i \leftrightarrow j}$  is the thermodynamic driving force for martensite reorientation between variant  $i$  ( $= 1, 2, 3$ ) and  $j$  ( $= 1, 2, 3$ ).

- Thermodynamic forces for phase transformation

$$A_{0i} = \left( -\frac{\delta g}{\delta z_j} \right) - \left( -\frac{\delta g}{\delta z_0} \right) \quad (3.5)$$

where  $A_{0i}$  is the thermodynamic driving force for the phase transformation between austenite and the martensite variant  $i$  ( $= 1, 2, 3$ ). A linear evolution law between  $A_{0i}$  and the volume-fraction transformation rate  $\dot{z}_{0i}$  is taken (see Figure 3-1).

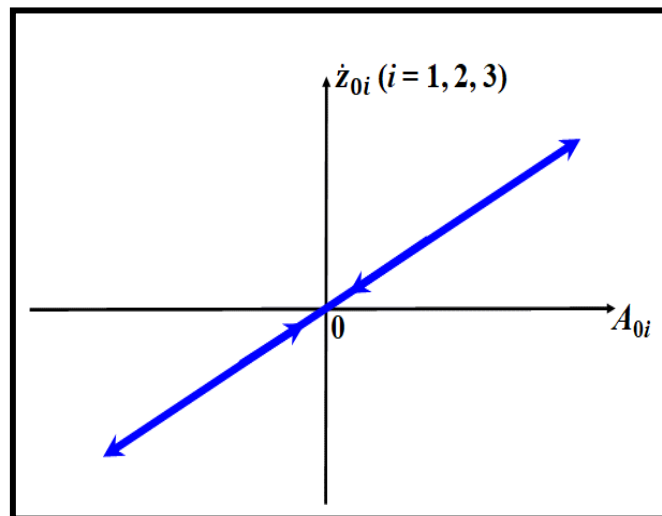


Figure 3-1. Linear phase transformation kinetics (Chen and He, 2020)

### 3.1.2. Mass-spring model of the MSMA dynamic system

A mass-spring-damper model is used to describe the dynamic behaviours of the MSMA system presented in (Zhang et al. (2018)). The constitutive model in Subsection 3.1.1 is embedded in the mass-spring-damper model. Figure 3-2 shows the schematic diagram of the dynamic system: (a) presents the loading conditions for the experimental setup, while (b) is the simplified mass-spring-damper model. Martensite reorientation between M1 and M2 and phase transformation between austenite and martensite variants are considered in the model (see the insert of Figure 3-2(b)). The whole model covers magnetic analysis, mechanical analysis, and thermal analysis, as detailed below.

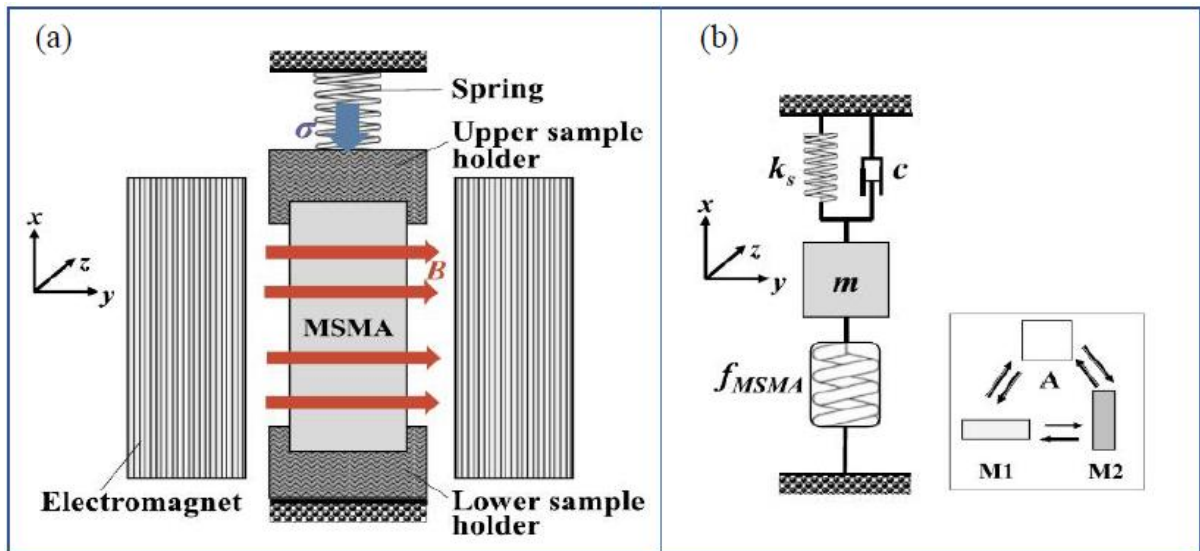


Figure 3-2. Schematic diagram of a dynamic system (Chen and He, 2020)

- Magnetic analysis

From Figure 3-2(a), the MSMA sample is supported at one end using a holder and the other end is compressed by a spring along the x-axis. While the sample is in place, a magnetic field is applied in a fixed direction (Figure 3-2(a)). The y-component of the magnetic field strength vector is the main component. So as to avoid complexity, only the y-component of the magnetic field is considered. Due to the demagnetization effect, the magnetic field inside the

MSMA sample, so-called the internal magnetic field  $H$  (y-component), is smaller than the applied  $H^{app}$ , and  $H$  can then be estimated as:

$$H = H^{app} - NM \quad (3.6)$$

where  $H$  is the internal magnetic field,  $H^{app}$  is the applied magnetic field,  $N$  is the demagnetisation factor,  $M$  is the magnetisation of the material.

- Mechanical analysis

With the application of a cyclic magnetic field, cyclic martensite reorientation is activated between variants 1 and 2, as demonstrated in Figure 3-2(b). As part of the moving pieces, the MSMA sample and the top sample container are regarded as lumped mass, and the appropriate dynamic system is created. The MSMA sample is in the initial state of martensite variant 1. An initial compressive stress  $\sigma_0$  is applied on the sample by a spring with stiffness  $k_s$ . Then, the spring is compressed by an initial distance  $\Delta x_1 = \frac{\sigma_0 S}{k_s}$  and the lumped mass has an initial displacement of  $\Delta x_2 = \frac{\sigma_0}{E} l_0$ . The 1D equilibrium equation of the mass-spring model in Figure 3-2(b) above can be quantified using the following:

$$m\ddot{x} + c\dot{x} + f_{spring} + f_{MSMA} = 0 \quad (3.7)$$

where  $S$  and  $l_0$  are respectively, the cross-sectional area and the initial length of the MSMA sample,  $m$  is the total mass of the dynamic system,  $x$  is the displacement of the mass with respect to its initial displacement,  $f_{spring}$  is the spring force,  $f_{MSMA}$  is the restoring force provided by the MSMA sample itself.

- Thermal analysis

$$\lambda \dot{T} = r_{tot} - \frac{2h}{R}(T - T_0) \quad (3.8)$$

where  $R (= \frac{ab}{a+b})$ , with  $a$  and  $b$  being the width and thickness of the MSMA sample, respectively)

is the effective radius of the MSMA sample,  $h (= \frac{\lambda R}{2t_h})$  is the heat convection coefficient,  $t_h$  is the

ambient heat-transfer time,  $\lambda$  is the specific heat per unit volume,  $r_{tot}$  is the total generation rate.

### 3.1.3. Programme flowchart

The mass-spring-damper model in Subsection 3.1.2 is incorporated into the commercial software MATLAB for the simulation. A triangular magnetic field of fixed amplitude and frequency is applied. For every magnetic loading and unloading, the cycle is divided into 1000 time steps. The flowchart for each step is presented in Figure 3-3, and the full algorithmic chart is presented in Appendix D.

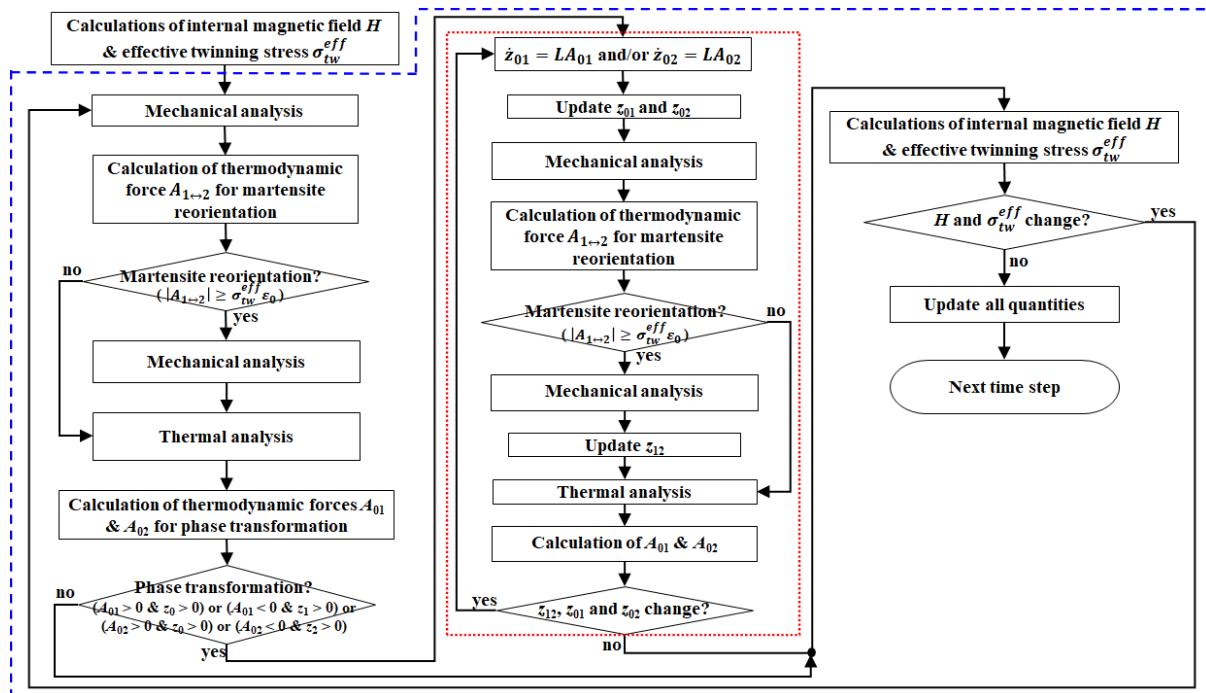


Figure 3-3. MATLAB programme flowchart (Chen and He, 2020)

## 3.2. Experimental setup for studies on the kinetics of temperature-driven phase transformation

Magnetic shape memory alloys possess an attractive property of regaining the original shape after undergoing a pseudo-plastic deformation due to phase transformation and/or

martensite reorientation. Understanding the phenomenon behind this strain change would assist their use in engineering applications. This section presents the experimental setup for studying the kinetics of temperature-induced phase transformation in Ni-Mn-Ga single crystals – the most common magnetic shape memory alloys.

### 3.2.1. Crystal structure

The XRD patterns of the NiMnGa sample can be seen in the Figure 3-4 below. These patterns have been analysed with reference to the indices of the diffracted planes, as documented in the literature for Ni<sub>2</sub>MnGa alloys (Li et al., 2011).

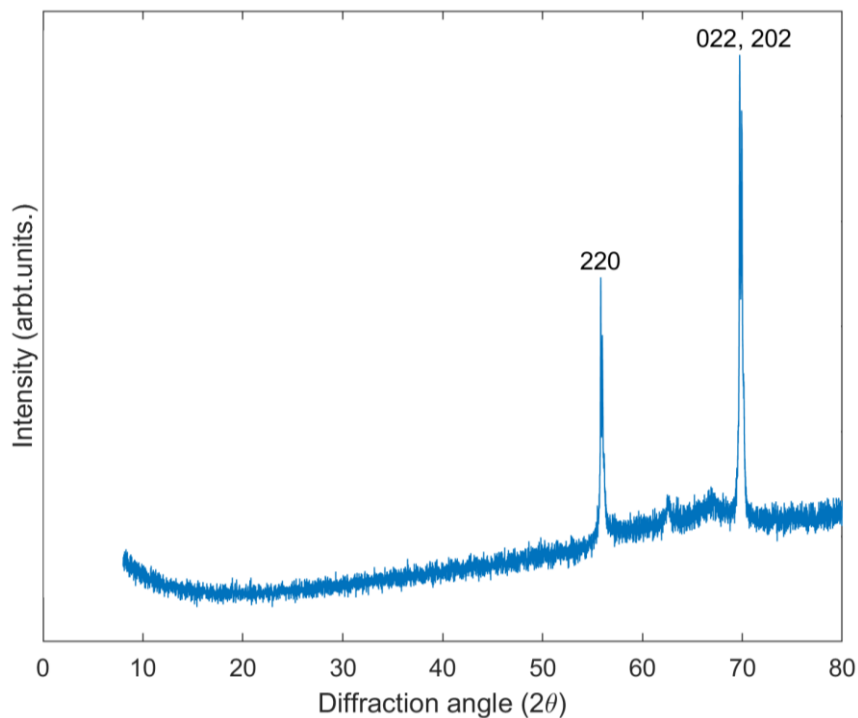


Figure 3-4. X-ray diffraction pattern of single crystal Ni<sub>50</sub>Mn<sub>28</sub>Ga<sub>22</sub>

Upon close inspection of the diffraction peaks and their intensities, there is a strong resemblance to the profiles reported for commensurate 5M modulated martensite with similar compositions (Righi et al., 2007, Mogylnyy et al., 2003, Jiang et al., 2004). The only discernible difference lies in the slight deviation of the recorded peaks. This suggests that the current alloy maintains the same crystal structure, specifically a commensurate 5M modulated structure, characterised by a superlattice composed of a tetragonal martensitic structure.

### 3.2.2. Digital Image Correlation (DIC) technique

To observe the microstructural evolution of magnetic shape memory alloys (MSMA), the optical measuring technique known as Digital Image Correlation (DIC) is employed. Images of sample surface taken from the camera/microscope are divided into subsets, i.e., a series of the grid with a recognisable pattern in each (Figure 3-5). Then, the correlation technique is used to analyse the displacement of each subset, and the local strain is further calculated.

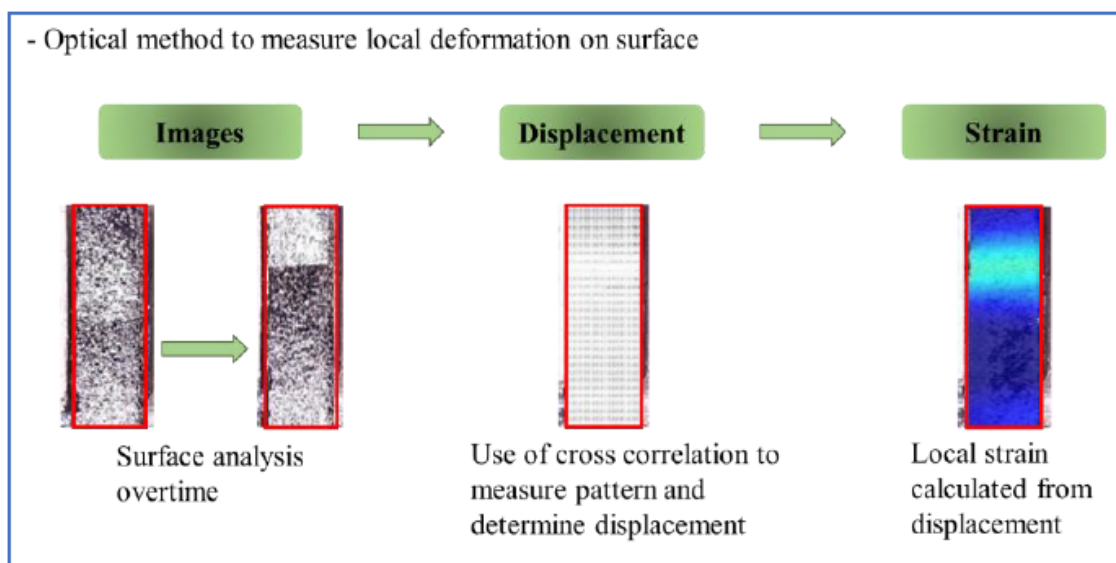


Figure 3-5. Principles of DIC Analysis

To further validate the microstructures obtained from the DIC local strain map, compatibility analysis from (Zhang et al., 2018b) is used. From the compatibility analysis of Ni-Mn-Ga single crystal, the orientations of the twin boundary and the compatible austenite-martensite interface (i.e., phase boundary), which is the interface between the cubic austenite phase and the martensite phase, can be obtained, as exemplified in Figure 3-6. It is seen that the observed austenite-martensite interface and twin boundary in Figure 3-7 have the same orientations as those predicted by the compatibility analysis in Figure 3-6.

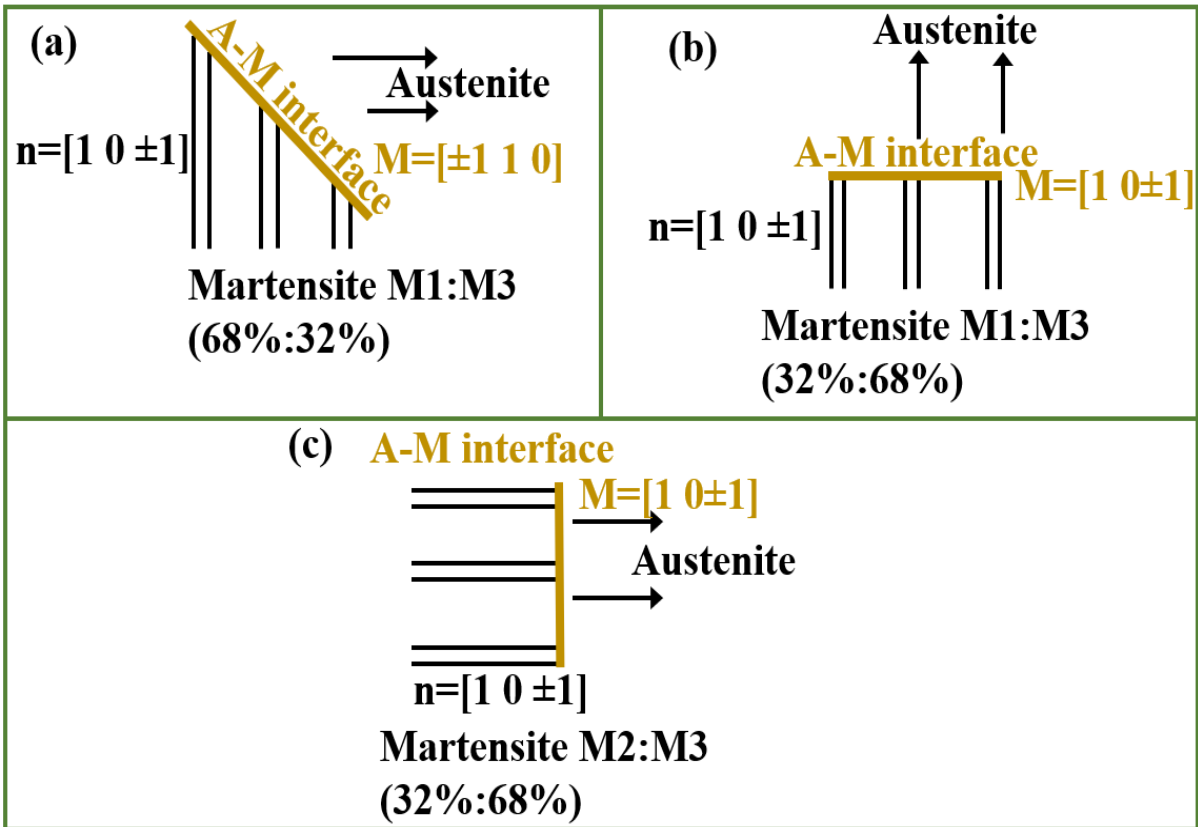


Figure 3-6. A-M interface and compatible martensite fine-twins on the  $x$ - $y$  plane from the compatibility analysis in Zhang et al. (2018b).



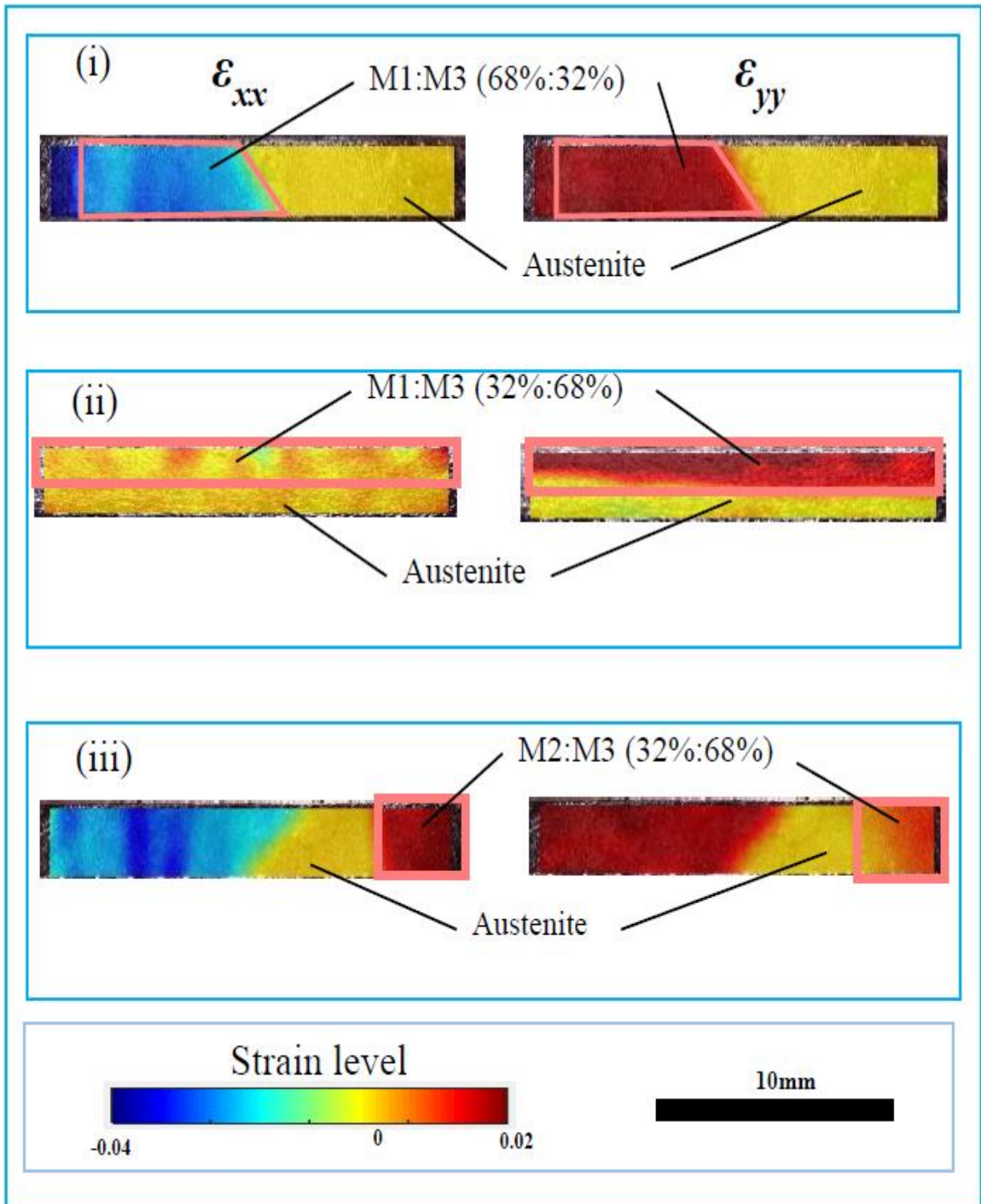


Figure 3-7. Typical strain maps from DIC.

### 3.2.3. Equipment properties and calibration

A heat gun (Seekone heat 2000W gun) is used to heat the MSMA's sample. A mini microscope (Bindpo USB digital microscope with 5 Megapixels and a recording rate of 30 fps)

is used to take photos of the sample surface. The microstructural evolutions are determined by treating the photos using Digital Image Correlation (DIC) technique presented in Subsection 3.2.1. A t-type thermocouple is attached to the sample holder to capture the temperature evolution. The resolution of this type of thermocouple is  $\pm 0.75\%$  error margin, i.e., the measured temperature may have  $\pm 1$  °C or 0.75% error. For example, for a measured value of 35 °C, the error is  $\pm 0.75\% \times 35 = \pm 0.3$  °C. During all tests, the temperature measurement from the thermocouple, the images taken from the mini microscope, and the control of the heat gun and data logger (squirrel SQ2040-2F16 data logger) are all synchronised using a laptop. The laptop puts the same time stamp on all equipment when the experiment is going on.

Calibrations of two different types of thermocouples (k-type and t-type) are conducted. The k-type thermocouple is made from chrome and aluminium conductors. The accuracy of the k-type is rated at  $\sim \pm 2.2$  °C or 0.75% (whichever is bigger). Its lead terminal is made of Ni-Cr+ || Ni-Al-. On the other hand, the t-type is made from 55% copper and 45% nickel, which is known as constantan alloy. Its lead terminal is made of Cu+ || Cu-Ni-. The accuracy of the t-type is rated at  $\sim \pm 1.0$  °C or 0.75% (whichever is bigger). Table 3-1 shows the measurements from the two types of thermocouples and compares them with the measurements from the digital thermometer, which is already calibrated and used as the reference here. By comparison, the t-type with higher accuracy is employed for the experimental studies in this thesis.

Table 3-1. Temperature measurements from thermocouples and digital thermometer.

<b>Digital thermometer</b> (°C)	<b>Thermocouple</b> <b>Type-t_1 (°C)</b>	<b>Thermocouple</b> <b>Type-t_2 (°C)</b>	<b>Thermocouple</b> <b>Type-k_1 (°C)</b>	<b>Thermocouple</b> <b>Type-k_2 (°C)</b>
<b>14.5</b>	14.6	14.7	14.3	14.6
<b>16.7</b>	16.7	16.6	16.8	16.9
<b>18.7</b>	18.5	18.5	18.4	18.3
<b>29.7</b>	29.4	29.5	29.4	29.2
<b>36.3</b>	36	36.1	35.8	35.7
<b>49.6</b>	49.7	49.7	49.2	49.3
<b>56.3</b>	56.5	56.5	56.2	56
<b>65.5</b>	65.7	65.7	65.1	65.7
<b>71.3</b>	71.1	71.2	71.1	71.6

#### **3.2.4. Experimental setup design**

The design and model parameters of the experimental setup for the homogeneous thermal loading is shown in Figure 3-8 and Table 3-2. The geometry of the setup (e.g., sample holder height) has a significant effect on the heating efficiency. Therefore, before fabricating the whole setup and conducting tests, finite element simulations by the commercial software ABAQUS are performed (Figure 3-9(a)) to find the optimised setup geometry for the most effective and suitable heating. Figure 3-9(b) shows the time evolutions of the sample temperature at different levels of sample holder height, from which a height of 4 mm is selected for the suitable heating rate of 2.94 °C/s. A 4-mm sample holder height is selected to achieve a heating rate of 2.94 °C/s. This heating rate, in combination with the chosen holder height, facilitates precise temperature control from the heater, ensuring that the phase transformations associated with the shape memory effect occur as consistently as possible throughout the material. Additionally, the 2.94 °C/s heating rate with a 4-mm holder height strikes a balance between the requirements for both rapid and slow heating rate analyses for phase transformations (Otsuka and Ren, 2005, Grigorieva et al., 2015, Malard et al., 2011).

Table 3-2. Abaqus model parameters

Description	Units	Value
<b>Heater Mat</b>		
Conductivity	W/m·K	0.12
Mass Density	Kg/m <sup>3</sup>	1420
Electrical Conductivity	S/m	1386.27
Joule Heat Fraction	J	1
Specific Heat	J/kg·K	1090
<b>Single crystal Ni-Mn-Ga</b>		
Conductivity	W/m·K	16
Mass Density	Kg/m <sup>3</sup>	8000
Electrical Conductivity	S/m	0.0001
Joule Heat Fraction	J	0
Specific Heat	J/kg·K	440

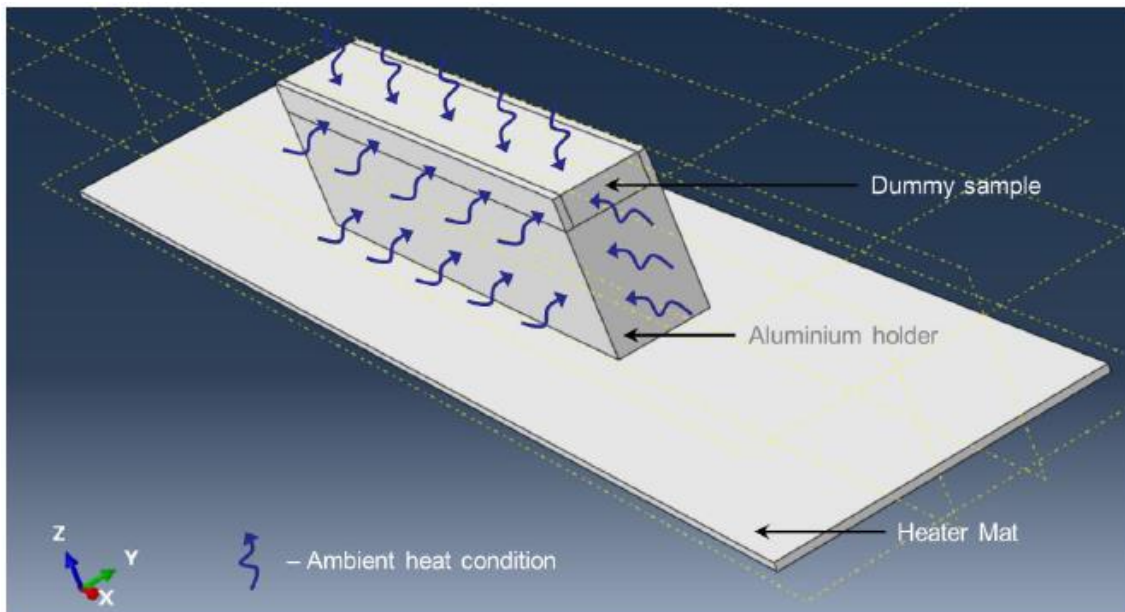
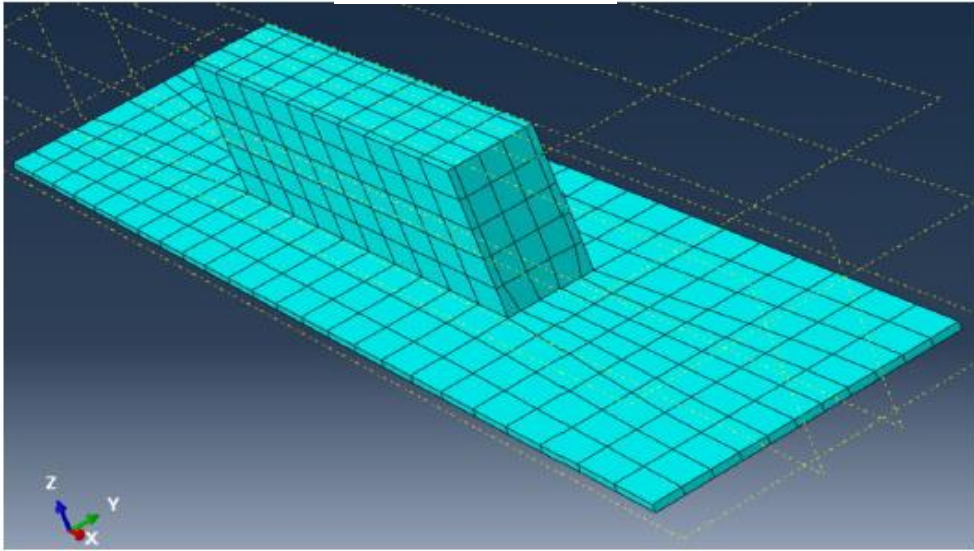


Figure 3-8. Design of experimental setup.

(a)



(b)

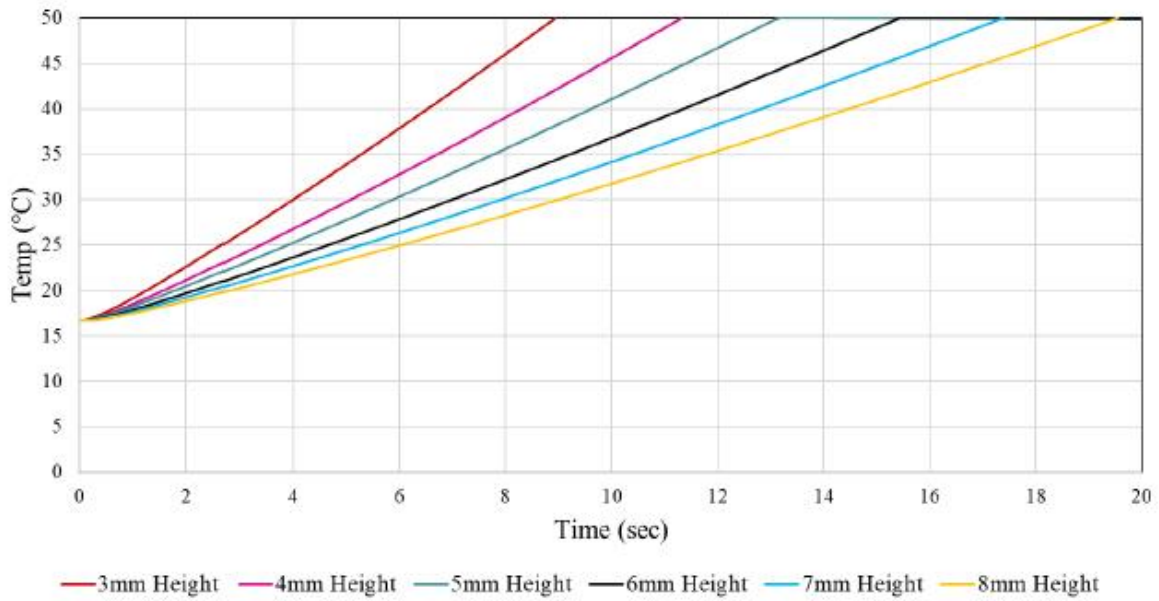


Figure 3-9. (a): ABAQUS simulation model. (b): Sample temperatures at different levels of sample holder height (simulation): Temperature increase rates of 3, 4, 5, 6, 7 and 8mm are 3.73, 2.94, 2.53, 2.16, 1.91 and 1.70 °C, respectively.

Two experimental setups are fabricated and tested. Setup 1 is shown in Figure 3-10. The MSMA sample is placed on an aluminium holder in a horizontal position where both ends of the sample are free to move. A heating mat under the sample holder is used to heat the sample and trigger the temperature-induced phase transformation. The experimental setup 2 is shown in Figure 3-11. The MSMA sample is placed on a PLA (Polylactic acid thermoplastic) holder

where both ends of the sample are free to move. Sample heating is attained via a heat gun and triggers the temperature-induced phase transformation (Figure 3-11).

In order to successfully carry out the experiments, Setup 2 is the optimal choice. Setup 1 is not used in the experiments in Chapter 5 because the aluminium sample holder has high heat conductivity and would absorb some amount of heat during the heating process, which is released during the cooling process. This influences the behaviour of the sample throughout the martensite-austenite phase transformation cycles. The second reason is that the heat that is stored in the aluminium holder during the heating process does interfere with the thermocouple readings, which gives an inaccurate reading of the temperature. Therefore, the readings from the experimental results are not reliable. The second configuration (setup 2) uses a PLA, which is a poor heat conductor. Because of this, the material has very little impact on the temperature readings.

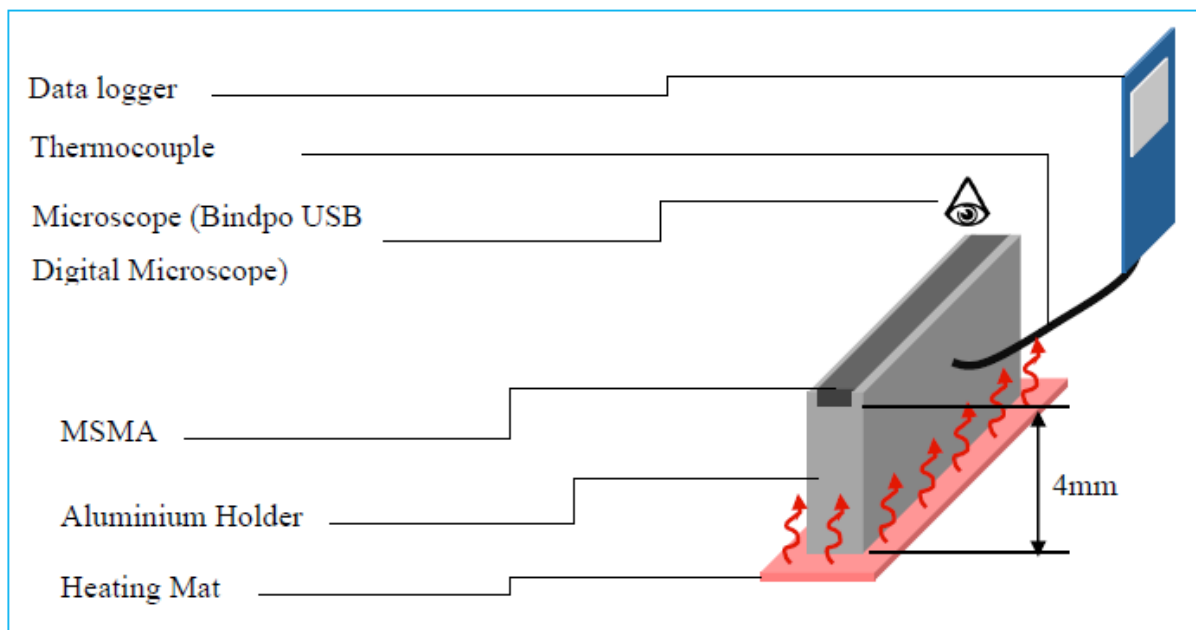


Figure 3-10. Schematic diagram of experimental setup 1.

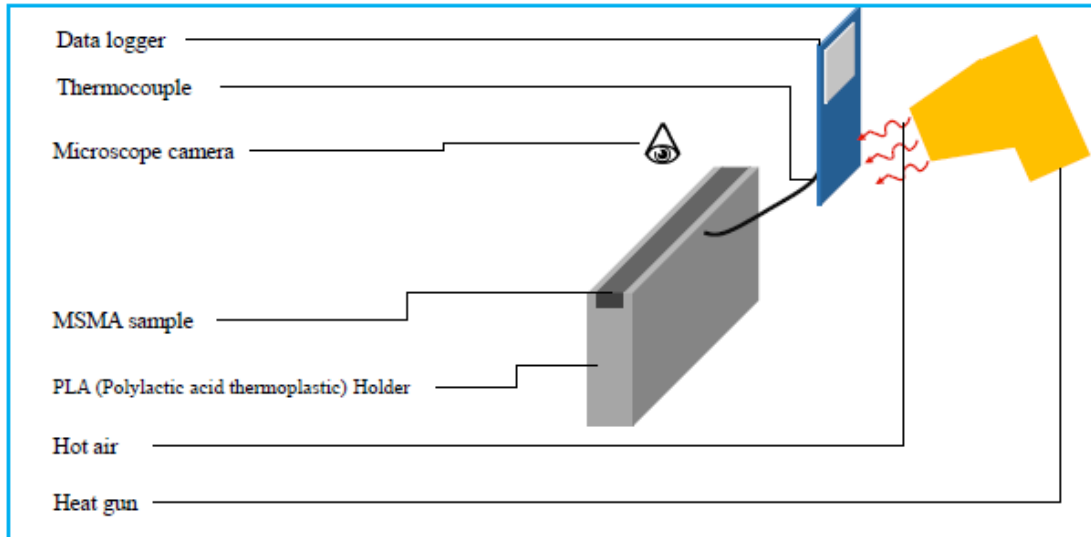


Figure 3-11. Schematic diagram of experimental setup 2

### 3.2.5. Preliminary test

Experimental setups 1 and 2 are used for the preliminary tests. Before each test in this subsection, the sample of Ni-Mn-Ga single crystals is compressed to ensure that it is in the initial state of a single martensite variant. Then the sample is heated to 50 °C above the austenite finish temperature  $A_f$  (~38 °C), where the martensite-to-austenite transformation completes. Different heating rates are applied by controlling the input voltage of the heating mat. Finally, the heating mat is switched off, and the sample is cooled down to room temperature by natural cooling.

Figure 3-12 and 3-13 give examples of microstructural evolution for setups 1 and 2, and Figure 3-14 showcases the strain evolution of the sample, along with their corresponding digital image correlation (DIC) images. For setup 1, the austenite start ( $A_s$ ) and finish ( $A_f$ ) temperatures are 39.0 °C and 39.5 °C respectively, and the martensite start ( $M_s$ ) and finish ( $M_f$ ) temperatures are 32.2 °C and 32.3 °C respectively. For setup 2, the  $A_s$  and  $A_f$  temperatures are 40.3 °C and 41.0 °C respectively, while the  $M_s$  and  $M_f$  temperature are 33.5 °C and 33.2 °C respectively. After conducting multiple tests, when the results were compared to the DSC temperatures (Figure 3-15), the average percentage error for setup 1 was found to be ~2%, while for setup

2, the average percentage error was ~1.5%. This demonstrates that setup 2 in general, produces more accurate temperature data than setup 1. The reduced accuracy observed in setup 1 is due to the heat absorption by the aluminium sample holder, as discussed earlier. In contrast, setup 2 employs a polylactic acid (PLA) material as the sample holder, which does not absorb heat during the experiment. This variation in heat absorption leads to enhanced accuracy of setup 2.

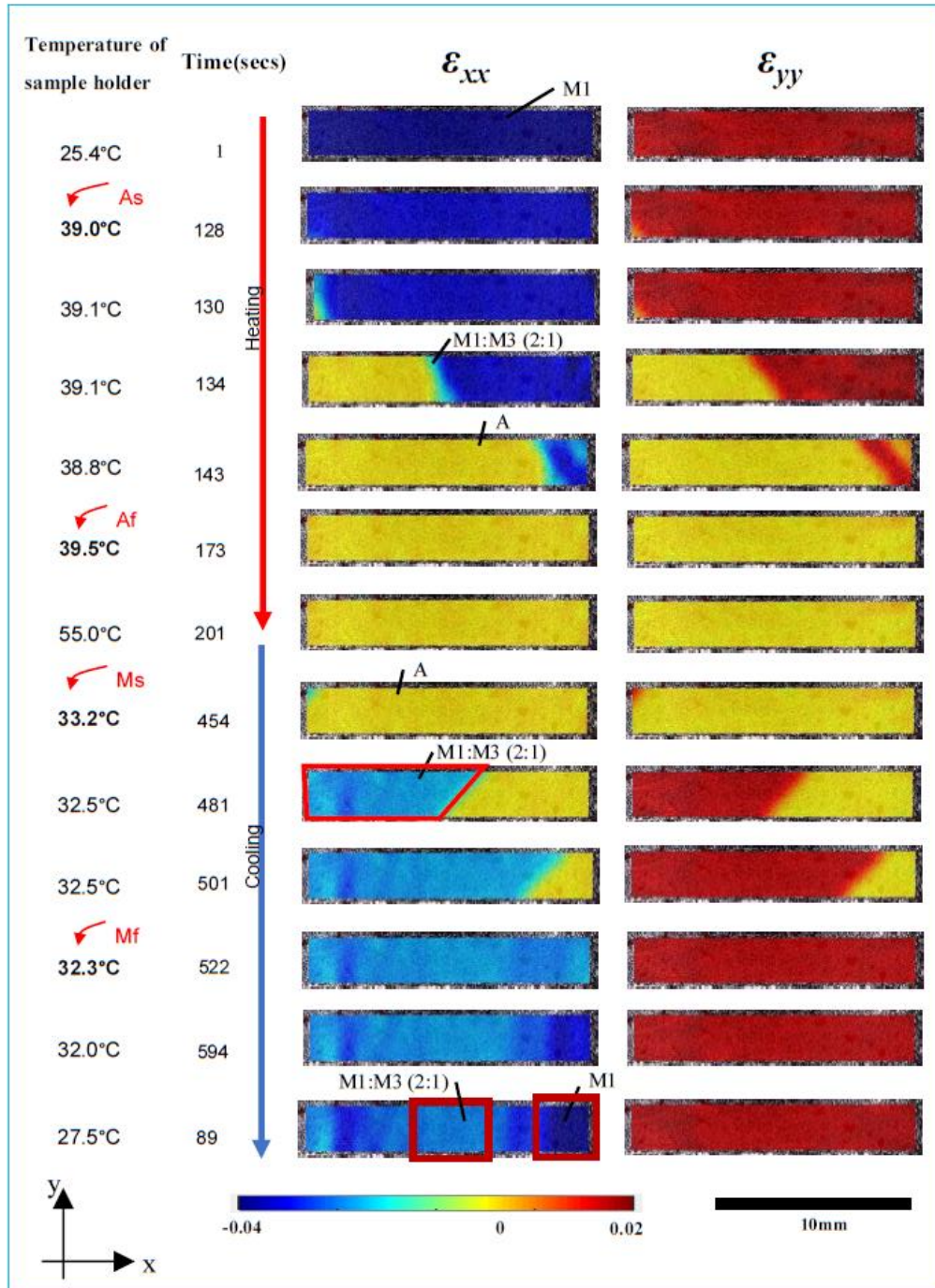


Figure 3-12. A typical heating by the input voltage of 4 V using experiment setup 1.



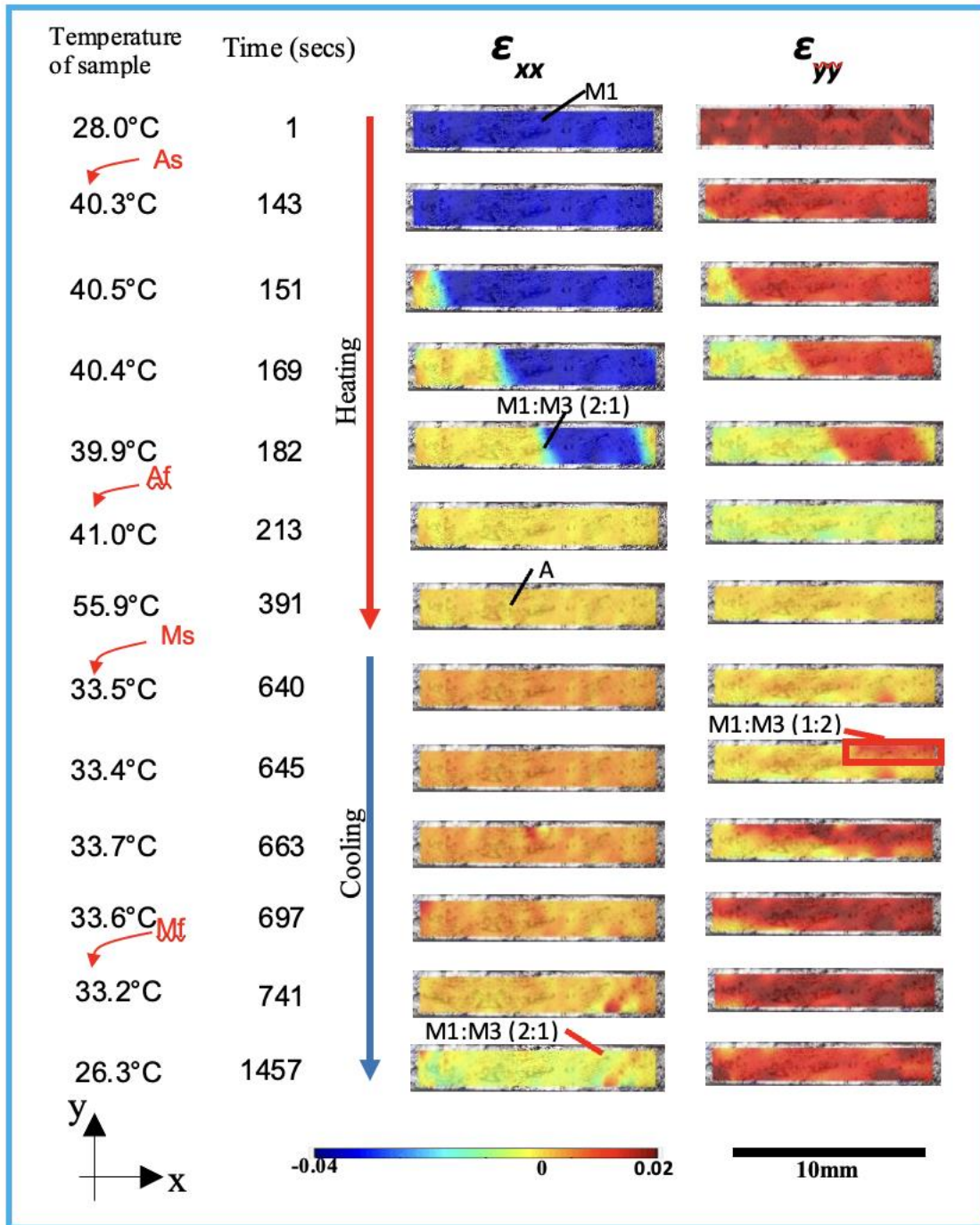


Figure 3-13. A typical heating process by the input voltage of 4 V using experiment setup 2

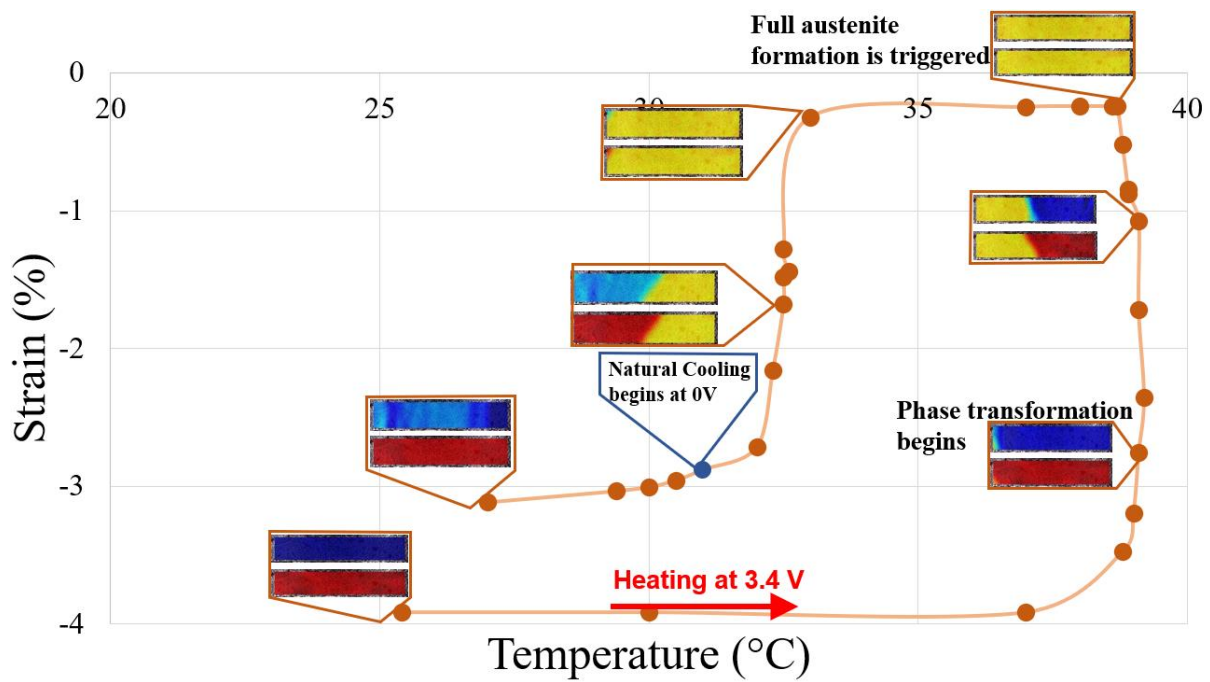


Figure 3-14. A typical strain evolution of experiment 1 with their DIC images.

The observed phase transformation temperatures and durations at different heating rates are summarised in Table 3-3. It is found that the phase transformation time decreases with increasing heating rate. Furthermore,  $M_s$  (martensite start temperature) is found to be close to  $M_f$  (martensite finish temperature) at all input voltages, while the difference between  $A_s$  (austenite start temperature) and  $A_f$  (austenite finish temperature) tends to increase with the increasing input voltage, possibly due to the non-uniform temperature distribution under high heating rate.

Table 3-3. Typical phase transformation temperatures at different applied voltages

Applied voltage	$A_s$ (°C)	$A_f$ (°C)	Average Transformation time (secs)	$M_s$ (°C)	$M_f$ (°C)	Average Transformation time (secs)
<b>4V</b>	39.0	39.5	15s	33.2	32.3	28s
<b>5V</b>	38.3	39.4	10s	31.1	31.9	25s
<b>6V</b>	38.6	40.8	7s	31.8	31.6	21s
<b>8V</b>	37.7	39.5	9s	31.8	32.2	61s
<b>10V</b>	36.1	41.2	5s	32.9	32.4	54s
<b>12V</b>	37.6	40.5	4s	30.0	30.2	73s

### 3.2.6. Differential scanning calorimetry (DSC) analysis

Another method to measure the phase transformation temperatures is to use differential scanning calorimetry (DSC) analysis. Single crystal Ni-Mn-Ga alloy provided by Goodfellow Cambridge Ltd. is tested. The sample of 10.12 mg is put into a chamber of the DSC testing machine (DSC 131 evo by Setaram), and the heating/cooling rate is maintained at 2 °C/min. The chamber temperature and the heat flow in/out of the chamber are measured by DSC, and a temperature–heat flow curve is finally obtained, as shown in Figure 3-15. From this figure, the transformation temperatures of martensite start ( $M_s$ ), martensite finish ( $M_f$ ), austenite start ( $A_s$ ) and austenite finish ( $A_f$ ) temperatures are found to be: 33.2 °C, 32.5 °C, 39.2 °C and 41.0 °C respectively.

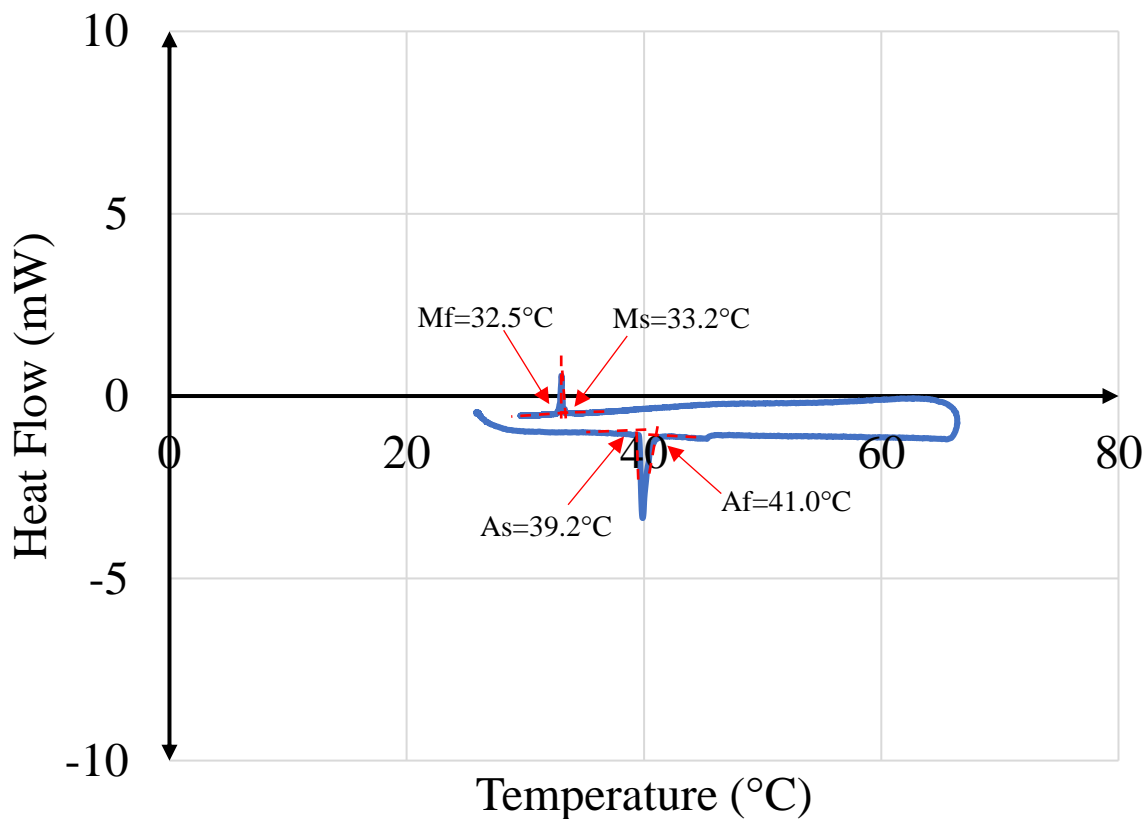


Figure 3-15. DSC curve for the Ni-Mn-Ga sample at the heating/cooling rate of 2 °C/min.

### **3.3. Chapter conclusion**

The theoretical modelling section outlines the modifications made to the existing model by Chen and He (2020) to account for the behaviour of the NiMnGa alloy under different levels of ambient heat transfer, temperature, and magnetic field frequency and amplitude. Moreover, this section provides a brief description of the theoretical modelling of the dynamic behaviour of magnetic shape memory alloys actuated by a high-frequency magnetic field detailed in Chapter 4.

In the experimental setup section, various factors are discussed that are taken into consideration when selecting an appropriate experimental setup for the analysis. Experimental results using setups 1 and 2 are compared to investigate the various heat patterns for these two types of heating setups on the sample and to select the most appropriate setup. This section also explains how the digital image correlation (DIC) images are validated with the experimental results presented in the literature (Zhang et al., 2018b) and further describes the calibration of the thermocouple. The section also presents the DSC curve for the sample.

## 4. Thermo-magnetic loading effects on the high-frequency dynamic behaviour of single crystal NiMnGa alloys

### 4.1. Introduction

Magnetic Shape Memory Alloys (MSMAs) are materials that can change shape when exposed to temperature, stress, and magnetic fields. Ni-Mn-Ga, a Ni-based MSMA, is the most studied and has a cubic structure at high temperatures and three tetragonal variants at low temperatures (see Figure 4-1).

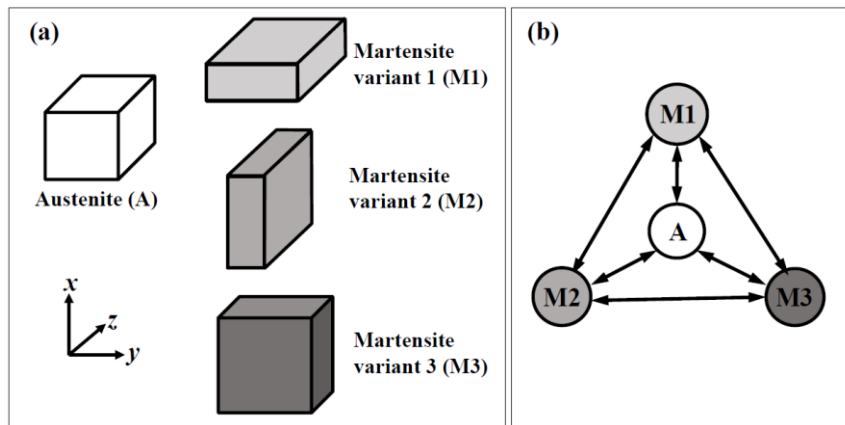


Figure 4-1. (a) Schematic diagram of the austenite and the martensite variants of Ni-Mn-Ga magnetic shape memory alloy: cubic austenite lattice and pseudo-tetragonal martensite lattice. (b) Martensite reorientation among three martensite variants (M1, M2, M3) and phase transformation between austenite (A) and martensite (M).

This chapter extends the model proposed in Chen and He (2020) to study the ambient thermal effects of ambient temperature and ambient heat-transfer condition, as well as the magnetic loading effects of magnetic field frequency and amplitude, on the long-term (> 100 s) high-frequency (> 100 Hz) dynamic behaviour of MSMAs actuated by cyclic magnetic fields. By further simplifying the dynamic model, theoretical analysis is also conducted to derive analytical expressions of the material's steady-state behaviours (i.e., stable output strain amplitude and temperature) as a function of ambient thermal conditions and magnetic loading conditions. The model simulations and analytical calculations demonstrate the roles that thermo-magnetic loading factors play in the material's dynamic behaviours.

## 4.2. Dynamic model

Figure 3-2 displays a schematic of the MSMA-based magnetic actuator. A spring is used to apply compressive force along the x-axis, and a pair of electromagnets apply the magnetic field along the y-axis. To regulate the ambient thermal state, airflow at various temperatures and velocities passes through the sample surface. The MSMA sample is set to an initial martensite state. In the sample, cyclic martensite reorientation between the stress-preferred variant (M1) and the magnetic-field-preferred variant (M2) is induced during the magnetic actuation (i.e., cyclic magnetic field) and results in the cyclic strain output (see inset of Figure 3-2 (b)). As seen in the inset of Figure 3-2, the martensite-to-austenite phase change may also be triggered depending on the thermo-magnetic loading circumstances.

The dynamic behaviour of the MSMA sample in Figure 3-2 (a) is described using the mass-spring-damper model in Figure 3-2 (b). The mass-spring-damper model incorporates the material model for the martensite reorientation and martensitic phase change of MSMA that was established (Chen et al., 2014, Chen and He, 2020). Below is a summary of the governing equations for thermo-magneto-mechanical analyses. These equations' thorough derivations are provided in Chen and He (2020).

### 4.2.1. Magnetic analysis

$H_2$  which is known as the internal magnetic field (only considering y-component) in the MSMA sample, is estimated as:

$$H = H^{app} - N(z_0M_0 + z_1M_1 + z_2M_2) \quad (4.1)$$

where  $H^{app}$  is the magnetic field applied by the electromagnets,  $N$  is the demagnetisation factor,  $z_0$ ,  $z_1$  and  $z_2$  are the volume fraction of austenite, martensite variant 1 and martensite variant 2 respectively, (denoted by A, M1 and M2 in Figure 3-2 (b)), and  $M_0$ ,  $M_1$ ,  $M_2$  are their respective magnetisations.

$$M_0 = \begin{cases} -M_s^A & \left(H < -\frac{M_s^A}{a_0}\right) \\ a_0 H & \left(-\frac{M_s^A}{a_0} \leq H \leq \frac{M_s^A}{a_0}\right) \\ M_s^A & \left(H > \frac{M_s^A}{a_0}\right) \end{cases} \quad (4.2)$$

$$M_i = \begin{cases} -M_s^M & \left(H < -\frac{M_s^M}{a_i}\right) \\ a_i H & \left(-\frac{M_s^M}{a_i} \leq H \leq \frac{M_s^M}{a_i}\right) \\ M_s^M & \left(H > \frac{M_s^M}{a_i}\right) \end{cases} \quad (i = 1, 2)$$

$M_s^A$  and  $M_s^M$  are denoted to be the saturation magnetisation of austenite and martensite, respectively, and  $a_0$  and  $a_i$  ( $i = 1, 2$ ) are the magnetic susceptibility of austenite and martensite variant  $i$ , respectively.

#### 4.2.2. Mechanical analysis

During the magnetic actuation, the cyclic martensite reorientation between M1 and M2 is induced. The thermodynamic force  $A_{1\leftrightarrow 2}$  for martensite reorientation between M1 and M2 can be calculated by Chen and He (2020):

$$A_{1\leftrightarrow 2} = \frac{E \varepsilon_0}{l_0} x + k \left( z_1^{(0)} - z_2^{(0)} + z_{01} - z_{02} \right) - \sigma_0 \varepsilon_0 + E_{1\leftrightarrow 2}^H \quad (4.3)$$

$$+ E \varepsilon_0 (z_{01} \varepsilon_c - z_{02} \varepsilon_a) - z_{12} (2k + E \varepsilon_0^2)$$

The displacement of the mass  $x$  in Figure 3-2 (b) is with respect to its initial displacement. The list of nomenclature and abbreviations provides parameters that have been adopted in this chapter. The calculation of the magnetic energy difference  $E_{1\leftrightarrow 2}^H$  between M1 and M2 can be found in Chen et al. (2014) and Chen and He (2020):

$$\begin{aligned}
E_{1\leftrightarrow 2}^{(H)} &= \frac{1}{2}\mu_0 a_2 |H|^2 \\
&+ \langle |H| - \frac{M_s^M}{a_2} \rangle \left( \mu_0 M_s^M |H| - \frac{1}{2}\mu_0 a_2 |H|^2 - \frac{1}{2a_2}\mu_0 (M_s^M)^2 \right) \\
&- \frac{1}{2}\mu_0 a_1 |H|^2 \\
&- \langle |H| - \frac{M_s^M}{a_1} \rangle \left( \mu_0 M_s^M |H| - \frac{1}{2}\mu_0 a_1 |H|^2 - \frac{1}{2a_1}\mu_0 (M_s^M)^2 \right)
\end{aligned} \tag{4.4}$$

where the function  $\langle x \rangle$  is being defined as:  $\{0, \text{ if } x < 0; 1, \text{ if } x \geq 0\}$ .

The following three scenarios for the mechanical analysis are in accordance with the material model of martensite reorientation in MSMA (Chen and He, 2020). The list of nomenclature and abbreviations provides definitions for each parameter used in the following equations.

When  $|A_{1\leftrightarrow 2}| < \sigma_{tw}^{eff} \varepsilon_0$ , with  $\sigma_{tw}^{eff}$  being the effective twinning stress of martensite reorientation estimated (Chen and He, 2020):

$$\sigma_{tw}^{eff} = \left( 0.2 - 0.02 \times (T - A_s^0) \times \left( 1 - \tanh \frac{2f_H - 199}{85} \right) \right) \times 10^6 \tag{4.5}$$

the martensite reorientation is non-existent. Then we have:

$$m\ddot{x} + c\dot{x} + \left( k_s + E \frac{S}{l_0} \right) x = ES(z_{12}\varepsilon_0 - z_{01}\varepsilon_c + z_{02}\varepsilon_a) \tag{4.6}$$

When  $A_{1\leftrightarrow 2} = \sigma_{tw}^{eff} \varepsilon_0$ , M1 switches to M2. Then the volume-fraction transformation  $z_{12}$  between M1 and M2 is calculated as:

$$\begin{aligned}
z_{12} &= \frac{1}{2k + E\varepsilon_0^2} \left( \frac{E\varepsilon_0}{l_0} x + k(z_1^{(0)} - z_2^{(0)} + z_{01} - z_{02}) - \sigma_0 \varepsilon_0 + E_{1\leftrightarrow 2}^H \right. \\
&\quad \left. + E\varepsilon_0(z_{01}\varepsilon_c - z_{02}\varepsilon_a) - \sigma_{tw}^{eff} \varepsilon_0 \right)
\end{aligned} \tag{4.7a}$$



The corresponding mechanical equilibrium equation can be calculated with the equation:

$$\begin{aligned}
m\ddot{x} + c\dot{x} + \left( k_s + \frac{2k}{\varepsilon_0^2} \frac{E}{\left( E + \frac{2k}{\varepsilon_0^2} \right) l_0} S \right) x \\
= \frac{ES\varepsilon_0}{2k + E\varepsilon_0^2} \left( k(z_1^{(0)} - z_2^{(0)} + z_{01} - z_{02}) - \sigma_0\varepsilon_0 + E_{1\leftrightarrow 2}^H \right. \\
\left. - \sigma_{tw}^{eff} \varepsilon_0 \right) - \frac{2kES}{2k + E\varepsilon_0^2} (z_{01}\varepsilon_c - z_{02}\varepsilon_a)
\end{aligned} \tag{4.7b}$$

When  $A_{1\leftrightarrow 2} = -\sigma_{tw}^{eff} \varepsilon_0$ , M2 switches to M1:

$$\begin{aligned}
z_{12} = \frac{1}{2k + E\varepsilon_0^2} \left( \frac{E\varepsilon_0}{l_0} x + k(z_1^{(0)} - z_2^{(0)} + z_{01} - z_{02}) - \sigma_0\varepsilon_0 + E_{1\leftrightarrow 2}^H \right. \\
\left. + E\varepsilon_0(z_{01}\varepsilon_c - z_{02}\varepsilon_a) + \sigma_{tw}^{eff} \varepsilon_0 \right)
\end{aligned} \tag{4.8a}$$

$$\begin{aligned}
m\ddot{x} + c\dot{x} + \left( k_s + \frac{2k}{\varepsilon_0^2} \frac{E}{\left( E + \frac{2k}{\varepsilon_0^2} \right) l_0} S \right) x \\
= \frac{ES\varepsilon_0}{2k + E\varepsilon_0^2} \left( k(z_1^{(0)} - z_2^{(0)} + z_{01} - z_{02}) - \sigma_0\varepsilon_0 + E_{1\leftrightarrow 2}^H \right. \\
\left. + \sigma_{tw}^{eff} \varepsilon_0 \right) - \frac{2kES}{2k + E\varepsilon_0^2} (z_{01}\varepsilon_c - z_{02}\varepsilon_a)
\end{aligned} \tag{4.8b}$$

### 4.2.3. Thermal analysis

The following 1D heat equation can be used to determine how temperature evolution is caused by heat generation and heat convection. (Chen and He, 2020):

$$\begin{aligned}
\dot{T} = (4641.4f_H - 1.35 \times 10^5) + \sigma_{tw}^{eff} \varepsilon_0 |\dot{z}_{12}| \\
+ (A_{01}\dot{z}_{01} + A_{02}\dot{z}_{02} + c_1T(\dot{z}_{01} + \dot{z}_{02})) - \frac{\lambda}{t_h} (T - T_0)
\end{aligned} \tag{4.9}$$

where  $t_h$  is the characteristic heat relaxation time, which is related to the ambient heat convection coefficient  $h$  and is denoted by  $t_h = \frac{\lambda R}{2h}$ . The definitions for additional parameters used are presented in the [list of nomenclature and abbreviations](#). The heat generation rate owing to the eddy current (caused by the cyclic magnetic field), the intrinsic dissipation of martensite reorientation, and the phase transformation are the first three terms on the right-hand side of Eq. (4.9), in that order. The rate of heat loss as a result of ambient heat transfer is the last term on the right-hand side of Eq. (4.9). In Eq. (4.9), for the phase transformation, the thermodynamic forces  $A_{01}$  and  $A_{02}$  are calculated as (Chen and He, 2020):

$$A_{01} = -\frac{E\varepsilon_c}{l_0}x - (k_0 + k + E\varepsilon_c^2)z_{01} - (k_0 - E\varepsilon_a\varepsilon_c)z_{02} + k_0z_0^{(0)} - k(z_1^{(0)} - z_{12}) + E\varepsilon_0\varepsilon_c z_{12} + \sigma_0\varepsilon_c + (c_0 - c_1T) + E_{01}^H \quad (4.10a)$$

$$A_{02} = \frac{E\varepsilon_a}{l_0}x - (k_0 - E\varepsilon_a\varepsilon_c)z_{01} - (k_0 + k + E\varepsilon_a^2)z_{02} + k_0z_0^{(0)} - k(z_2^{(0)} + z_{12}) - E\varepsilon_0\varepsilon_a z_{12} - \sigma_0\varepsilon_a + (c_0 - c_1T) + E_{02}^H \quad (4.10b)$$

with the magnetic energy difference  $E_{0i}^H$  ( $i = 1, 2$ ) between austenite and martensite variant  $i$  being calculated as:

$$E_{0i}^H = \frac{1}{2}\mu_0 a_i |H|^2 + \langle |H| - \frac{M_s^M}{a_i} \rangle \left( \mu_0 M_s^M |H| - \frac{1}{2}\mu_0 a_i |H|^2 - \frac{1}{2a_i} \mu_0 (M_s^M)^2 \right) - \frac{1}{2}\mu_0 a_0 |H|^2 - \langle |H| - \frac{M_s^A}{a_0} \rangle \left( \mu_0 M_s^A |H| - \frac{1}{2}\mu_0 a_0 |H|^2 - \frac{1}{2a_0} \mu_0 (M_s^A)^2 \right) \quad (4.11)$$

With  $A_{0i}$  ( $i = 1, 2$ ) calculated by Eq. (4.10), we can further calculate the rate  $\dot{z}_{0i}$  of the volume-fraction transformation between austenite and martensite variant  $i$  as:  $\dot{z}_{0i} = LA_{0i}$ , where  $L$  is a coefficient in the phase transformation of linear kinetics law (Chen and He, 2020).

It is possible to determine the temperature evolution by adding the value of  $\dot{z}_{0i}$  to Eq. (4.9). Appendix D contains the algorithmic chart for Equations (4.1) through to (4.11).

### **4.3. Thermo-magnetic loading effects**

To simulate the behaviour of magnetic shape memory alloys actuated by cyclic magnetic fields under various thermo-magnetic loading conditions, the dynamic model from Section 4.2 is integrated into the MATLAB software. The entire loading circumstances are investigated in more depth below and include the ambient heat-transfer condition, the ambient temperature, the applied magnetic field amplitude, and frequency.

#### **4.3.1. Ambient heat-transfer condition**

In order to quantify the ambient heat-transfer condition, the characteristic heat relaxation time  $t_h$  is used: as the value of  $t_h$  decreases, the ambient heat-transfer condition increases, and vice versa. The detailed characteristics of  $t_h$  can be found in (Zhang et al., 2018a, Zhang et al., 2020).

A typical illustration of material's reactions to a gradual response in the heat relaxation time  $t_h$  is shown in Figure 4-2. The magnified views in Figure 4-2(b) demonstrate the application of a cyclic magnetic field. The triangle wave of the input magnetic field oscillates between +0.78 T and 0.78 T. (i.e., with an amplitude of 0.78 T). The material's output strain stabilises at the time  $t_1$  (about 200 s), and it can be observed from Figure 4-2(b) that the output strain is also a triangle wave with an amplitude of 1.81%. The physical mechanism for the growth of the strain is revealed by the enlarged views of the volume fractions ( $z_1$ ,  $z_2$ ) of martensite variations at  $t_1$  in Figure 4-2 (b). The stress-preferred variant M1 switches to the magnetic-field-preferred M2 as the strength of the magnetic field increases (i.e., magnetic loading), as shown by the increase in  $z_2$  and decrease in  $z_1$  in Figure 4-2(b), and this variant switching (i.e., martensite reorientation) causes the strain to increase. The switch from M2 to

M1 causes the strain to decrease as the magnetic field strength decreases (i.e., magnetic unloading). This results in cyclic martensite reorientation between M1 and M2, changing the output strain between a maximum value and a minimum value. The amount of martensite participating in the cyclic martensite reorientation is represented by the amplitude of the cyclic change in the volume fractions of martensite variants, such as 0.31 at  $t_1$  in Figure 4-2(b), and this in turn, influences the strain amplitude (i.e., the difference between the maximum and minimum).

The material's reaction frequency is discovered to be two times the applied magnetic field frequency from the magnified picture at  $t_1$  in Figure 4-2(b). This is due to the fact that there are two cycles of martensite reorientation in a cycle of magnetic field: one in the range of positive magnetic field (0 ~ 0.78 T) and the other in the range of negative magnetic field (0.78 T ~ 0). Additionally, there is a delay in the material's response as a result of the dynamic system's damping effect; the strain reaches its highest point at a magnetic field magnitude below 0.78 T and its minimum at a magnetic field magnitude above 0 (see  $t_1$  in Figure 4-2(b)).

The material's stable output strain amplitude increases from 1.81% to 5.85% when the heat relaxation time  $t_h$  is increased from 1 s to 10 s (see the magnified views of output strain progression at times  $t_1$ ,  $t_2$ , and  $t_3$  in Figure 4-2(b)), together with a rise in its stable temperature from 21.20 °C to 36.91 °C (see Figure 4-2(a)). The ambient heat transfer weakens as  $t_h$  rises, transferring less heat to the environment and raising the material's temperature. The twinning stress, which is regarded as the frictional stress for martensite reorientation, decreases with rising material temperature (see Eq. (4.5)). The rise in the amplitude of the cyclic change of volume fractions for both variants from 0.31 to 0.99 (see the magnified views at times  $t_1$ ,  $t_2$ , and  $t_3$  in Figure 4-2(b)) indicates that more martensite can participate in this case's cycle of martensite reorientation. The strain amplitude consequently rises.

The material's stable output strain amplitude reduces from 5.85% to 0.41% as the relaxation time  $t_h$  increases from 10 s to 80 s (see the magnified views at times  $t_4$ ,  $t_5$ , and  $t_6$  in Figure 4-2(b)), but its temperature remains nearly constant at 39 °C. We can infer from the evolution of the volume fraction of austenite in Figure 4-2 (a) that the martensite-to-austenite phase transformation is initiated in this range of  $t_h$  ( $> 10$  s), causing the material's temperature to remain at the typical phase transformation temperature (39 °C) and the volume fraction of austenite to rise from 0 to 0.93 (see Figure 4-2(a)). Reduced output strain amplitude results from less martensite remaining in the material to participate in martensite reorientation. The material is completely changed into austenite when  $t_h$  is large enough, such as 300 seconds in Figure 4-2(a), meaning that the volume proportion of austenite is 1. The temperature of the material in this instance (42.63 °C in Figure 4-2 (a)) is higher than the typical phase change temperature, and the output strain amplitude of the material is zero.

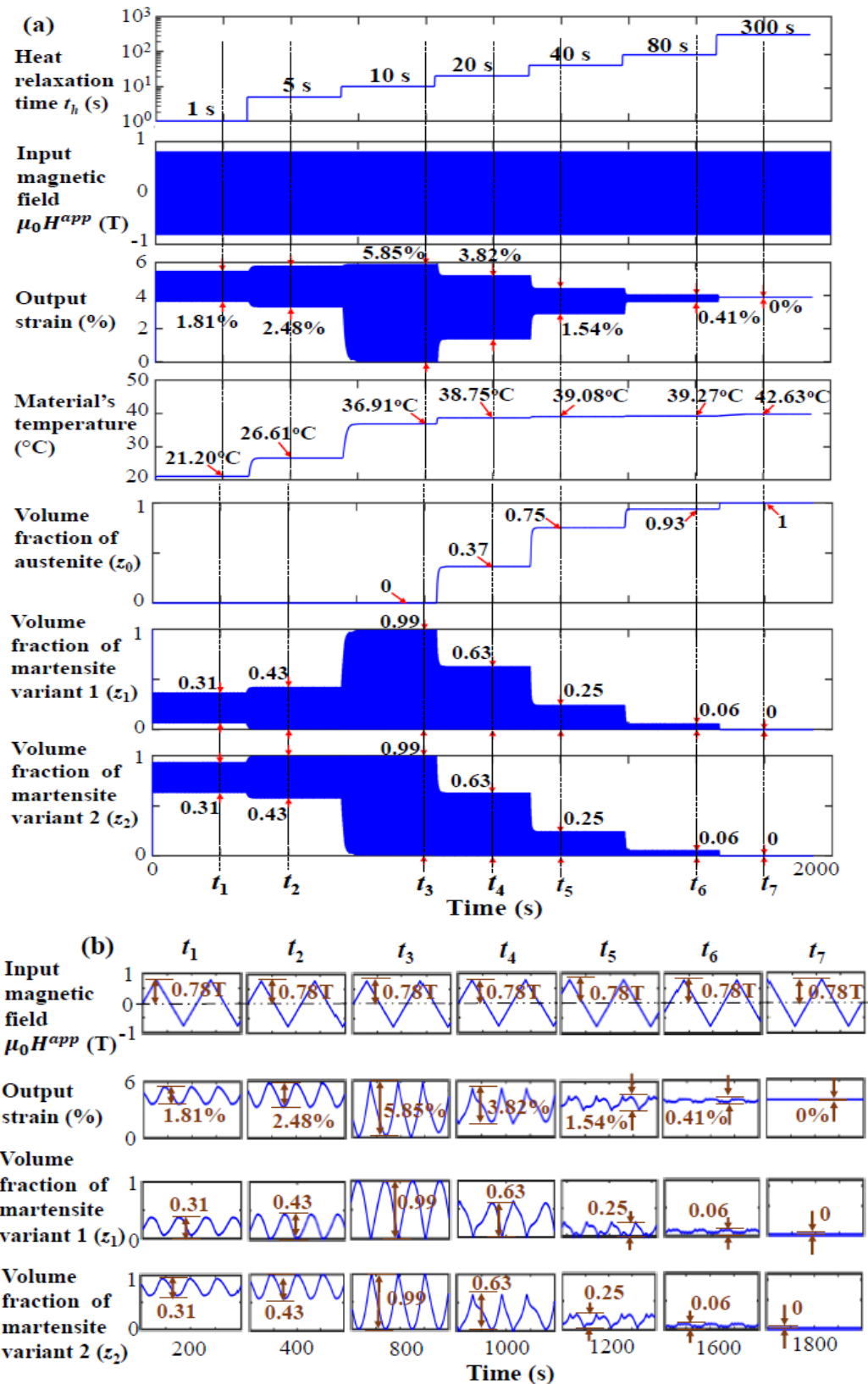


Figure 4-2. (a) Material's responses to the gradual change of heat relaxation time  $t_h$ . (b) Magnified views of stable states. The span of each view is 0.02 s. In order to achieve this, the model in MATLAB is performed at a magnetic field amplitude of 0.78 T, magnetic field frequency of 90 Hz (90Hz frequency denotes that the material's response frequency is twice, i.e.,  $2 \times 90 = 180$  Hz), and ambient temperature of 20  $^{\circ}\text{C}$ .

Figure 4-3 presents the interaction of temperature-induced phase transformation and magnetic-field-induced martensite reorientation during high-frequency magnetic actuation on MSMA and the summary of the material's stable (i.e., long-term steady state) behaviour at different levels of heat relaxation time  $t_h$ . The specimen presents three zones as the relaxation time increases: non-active austenite zone (constant zero deformation), active martensite zone (cyclic martensite deformations), and buffering zone (mixture of austenite and martensite). The heat generated within the specimen due to the temperature-driven phase boundary motion and the magnetic-field-driven twin boundary motion can coexist under magnetic actuation with changing ambient airflow. Hence, by controlling the value of  $t_h$ , the material can exhibit one of the following three states:

- $t_h < 12$  s: martensite state (M) with volume fraction of austenite = 0
- $12 \text{ s} \leq t_h < 270$  s: mixture state (M&A) where martensite and austenite coexist, with volume fraction of austenite between 0 and 1
- $t_h \geq 270$  s: austenite state (A) with volume fraction of austenite = 1

The boundary between the martensite zone M and the mixing zone M&A is where the output strain amplitude peaks. This is because the temperature of the martensite state is at its highest on this boundary, which results in the least amount of twinning stress. As a result, the maximum strain amplitude can be produced by the cyclic martensite reorientation, which can involve the highest fraction of martensite. Figure 4-3 also displays experimental findings from the literature, and it demonstrates a good level of agreement with model simulations.

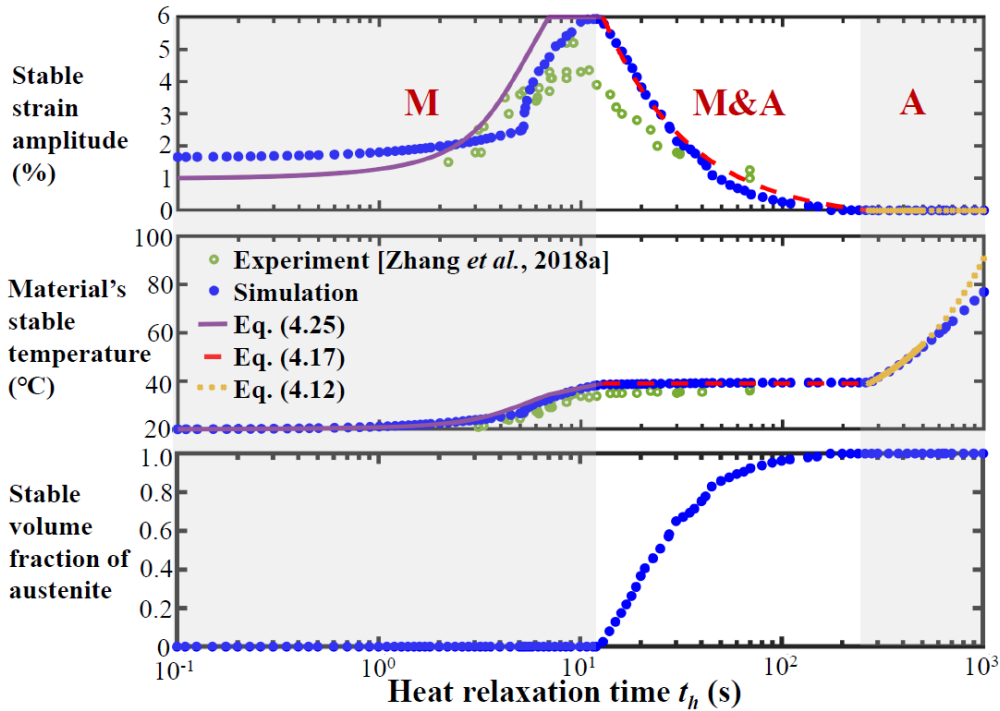


Figure 4-3. At various levels of heat relaxation time  $t_h$ , the material's stable behaviours (such as stable output strain amplitude and stable temperature) are shown. Martensite state (M), mixture state (M&A), when martensite and austenite coexist, and austenite state (A) are the three zones that correspond to the three material states. The ambient temperature is 20 °C, the magnetic field amplitude is 0.78 T, the magnetic field frequency is 90 Hz (making the material's response frequency  $2 \times 90 = 180$  Hz), and all simulations are run under these conditions.

#### 4.3.2. Ambient temperature

Figure 4-4(a) presents a typical behaviour of material's responses during a gradual change of the ambient temperature  $T_0$ . The twinning stress is high at low ambient temperatures (like  $-10$  °C in the figure). Cyclic martensite reorientation cannot be induced in this situation. As a result, the material's output strain amplitude is 0, and its stable temperature (in the figure,  $-8.58$  °C) is slightly higher than the outside temperature as a result of eddy current heat. The cyclic martensite reorientation is triggered when the ambient temperature rises to 5 °C, because the twinning stress is reduced. The output strain amplitude increases from 0 to 5.92% in the figure, while the temperature of the material rises from  $-8.58$  to 37.37 °C as a result of heat generation during cyclic martensite reorientation.

The martensite-to-austenite phase transition is triggered when the ambient temperature rises from 5 °C to 30 °C in Figure 4-4(a). At this point, the material approaches the typical



phase transformation temperature of 39 °C. Figure 4-4(a) shows a rise in the volume fraction of austenite from 0 to 0.79. The material's output strain amplitude drops from 5.92% to 1.31% as less martensite is left to participate in the martensite reorientation. The phase transformation is complete, and the material is in the austenite state when the ambient temperature is raised to 40 °C, as shown in Figure 4-4(a), where the volume fraction of austenite is 1. Since there is no martensite reorientation in this situation, the output strain amplitude is 0.

The steady behaviour of the material at various levels of ambient temperature  $T_0$  is summarised in Figure 4-4(b). The material's state can be controlled similarly to Figure 4-3(b) by adjusting  $T_0$ :

- $T_0 < 10$  °C: martensite state (M)
- $10$  °C  $\leq T_0 < 38$  °C: mixture state (M&A) where martensite and austenite coexist
- $T_0 \geq 38$  °C: austenite state (A)

Additionally, the boundary between the martensite zone M and the mixing zone M&A, where the martensite state's temperature reaches its maximum and the twinning stress reaches its minimum, is where the largest output strain amplitude is found.

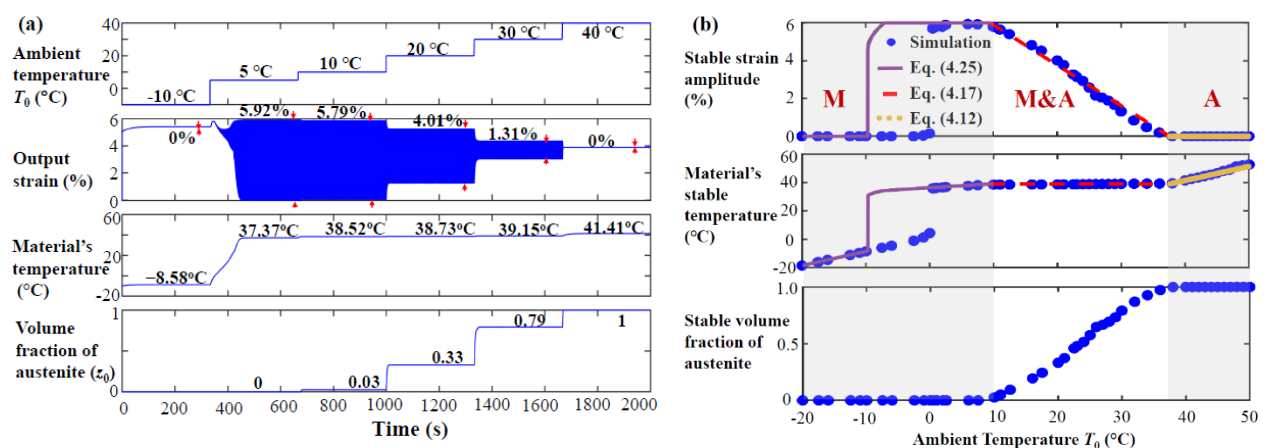


Figure 4-4. (a) Responses of the material to a change in ambient temperature  $T_0$  over time. (b) Stable behaviours of the material (stable output strain amplitude, stable temperature) at various ambient temperature levels: martensite state (M), mixture state (M&A) (when martensite and austenite coexist), and austenite state (A) are the three zones that correspond to the three material states. All simulations are run using a magnetic field amplitude of 0.8 T, magnetic field frequency of 90 Hz, and a heat relaxation time of 20 s. So the material response frequency is:  $2 \times 90 = 180$  Hz.

### 4.3.3. Magnetic field amplitude

Figure 4-5(a) provides an illustration of how a material reacts to a gradual change in the applied magnetic field amplitude,  $\mu_0 H_{amp}^{app}$ . Low magnetic field amplitudes, such as 0.1 T in Figure 4-5(a), cannot induce the conversion from the initial stress-preferred martensite variant M1 to the magnetic-field-preferred variant M2. The material's output strain, therefore, stays at 0. The M1-to-M2 switching is triggered by raising the magnetic field amplitude from 0.1 T to 0.7 T, as evidenced by the increase in the material's output strain amplitude from 0 to 1.82% (Figure 4-5(a)). The material's temperature rises from 23.16 °C to 38.46 °C concurrently as a result of the increased heat dissipation caused by the cyclic martensite reorientation. The material's stable output strain amplitude increases slightly from 1.82% to 2.19% and meets the typical phase transformation temperature (about 39 °C) when the magnetic field amplitude is increased further to 1.0 T in Figure 4-5(a). As a result, Figure 4-5(a) shows that the martensite-to-austenite transition is initiated, increasing the volume fraction of austenite from 0 to 0.64.

Figure 4-5(b) provides a summary of the material's stable behaviour at various levels of applied magnetic field amplitude. There are two different material states depending on the level of  $\mu_0 H_{amp}^{app}$ :

- $\mu_0 H_{amp}^{app} \leq 0.7$  T: martensite state (M)
- $\mu_0 H_{amp}^{app} > 0.7$  T: mixture state (M&A) where martensite and austenite coexist

The figure also shows that the output strain amplitude in the mixture state (M&A) is not significantly affected by the applied magnetic field amplitude. This will be explained in Section 4.4.2, along with the cause.

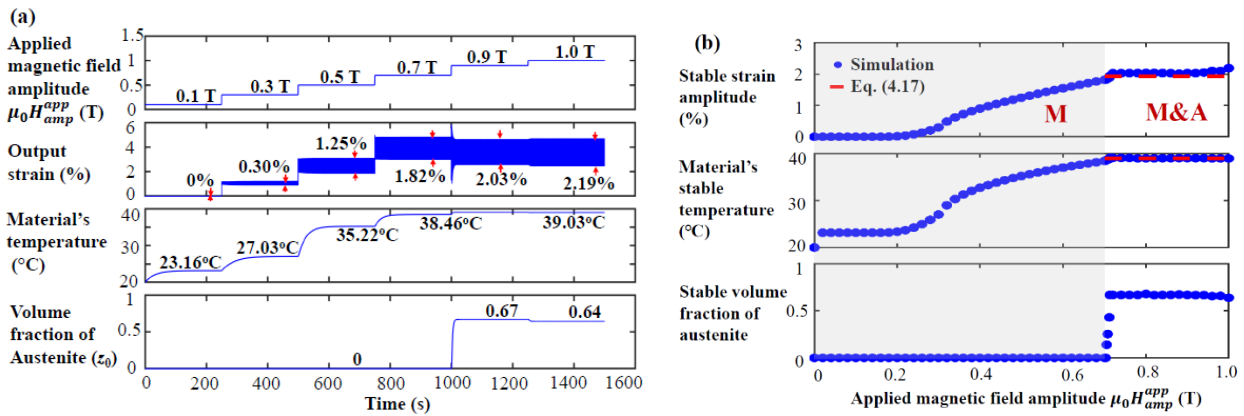


Figure 4-5. (a) Responses of the material to gradual changes in the applied magnetic field amplitude  $\mu_0 H_{amp}^{app}$ . (b) Stable behaviours of the material, such as stable output strain amplitude and stable temperature, at various magnetic field amplitude levels. There are two zones that correspond to the martensite state (M) and the mixture state (M&A), where austenite and martensite coexist. The MATLAB simulations are run with the following parameters: a heat relaxation time of 30 s, an ambient temperature of 20 °C, and a magnetic field frequency of 120 Hz. So the material response frequency is:  $2 \times 120 = 240$  Hz.

#### 4.3.4. Magnetic field frequency

Different frequency responses can be seen in the material depending on the surrounding ambient conditions. The material maintains its martensite state and displays the typical resonance-like frequency response in conditions of strong ambient heat transfer and/or low ambient temperature (see an example in Figure 4-6(b)). In Figure 4-6(a), the output strain amplitude of the material increases from 3.88% to the highest value of 5.64% at 90 Hz and subsequently drops to 0.77% as the magnetic field frequency is increased from 50 Hz to 150 Hz. The temperature trend of the material is identical; it initially rises to the peak value of 37.68 °C at 90 Hz and then falls to 28.92 °C. This is due to the fact that the output strain amplitude, which is a representation of the dissipation of heat from the cyclic martensite reorientation, primarily regulates the material's temperature. Throughout the entire simulated frequency range, the material's stable temperature is below the typical phase transformation temperature ( $\sim 39$  °C), maintaining the material's martensite state and keeping the volume proportion of austenite at 0 in Figure 4-6 (a).

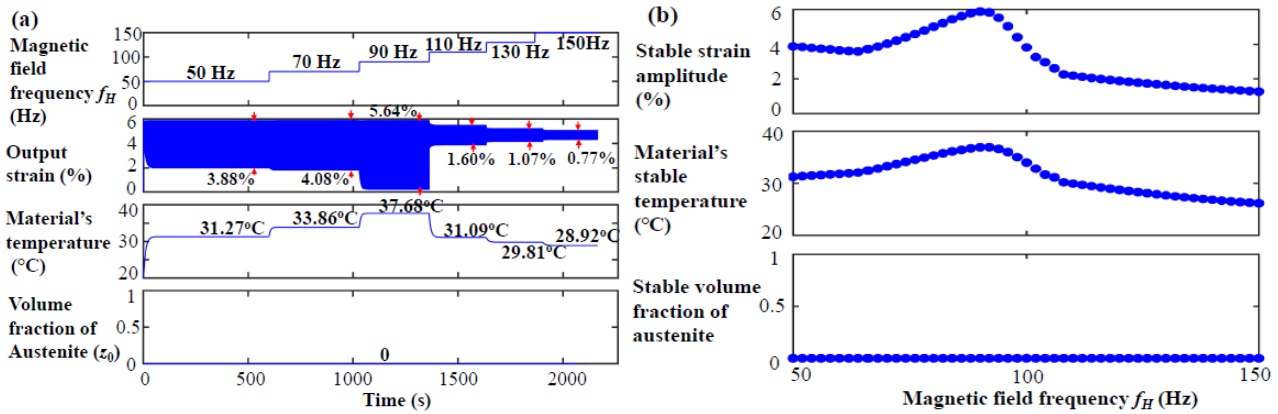


Figure 4-6. (a) Martensite state's responses to the magnetic field frequency's gradual change,  $f_H$  - I: martensite state. (b) The stable behaviours of the material (such as stable output strain amplitude and stable temperature) at various magnetic field frequencies. All simulations are run at an ambient temperature of 20 °C, a magnetic field amplitude of 0.8 T, and a heat relaxation time of 10 s. It should be noted that the material's response frequency is two times the frequency of the applied magnetic field, making the response frequency of the simulated material from 100 Hz to 300 Hz.

The material's temperature can reach the typical phase change temperature when the ambient heat-transfer condition is poor and/or the ambient temperature is high. Since the material is in a mixed condition where martensite and austenite coexist, the martensite to austenite transition has been triggered in this instance. Figure 4-7(b) displays a typical illustration of the frequency response in this situation. As opposed to the resonance-like frequency response in Figure 4-6(b), Figure 4-7(b) shows a monotonic drop in strain amplitude with increasing magnetic field frequency. Figure 4-7(a) displays in detail how the material reacts to a steady shift in the magnetic field frequency. The figure shows that the material's stable output strain amplitude reduces from 2.06% to 0.76% when the magnetic field frequency is raised from 50 Hz to 150 Hz, but its temperature stays close to the typical phase transformation temperature ( $\sim 39$  °C). The martensite-to-austenite transition is accelerated by an increase in actuation frequency because the heat from cyclic martensite reorientation accumulates more quickly. As a result, Figure 4-7(a) shows a rise in the volume fraction of austenite from 0.66 to 0.84. The output strain amplitude reduces as less martensite is left in the material to participate in the martensite reorientation.

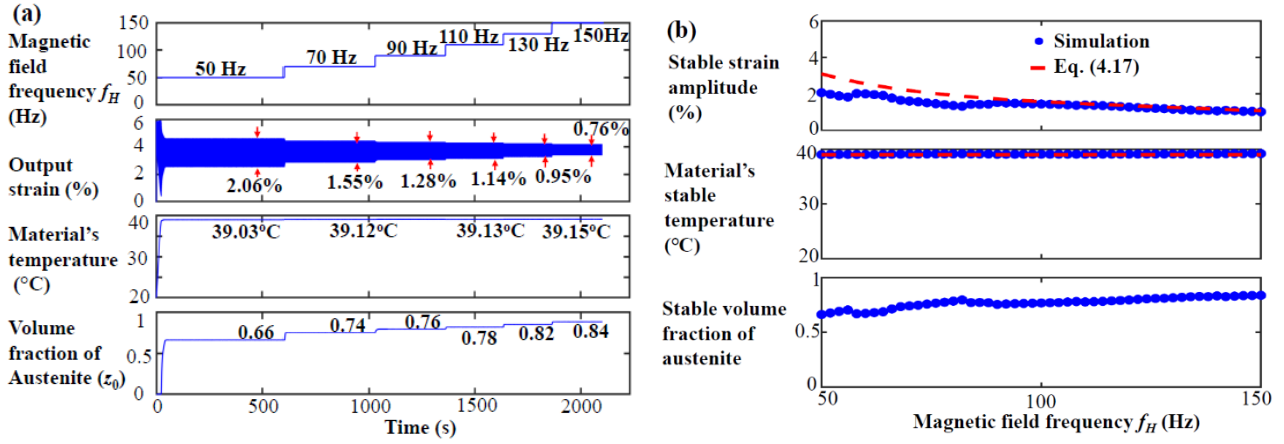


Figure 4-7. (a) Materials' reactions to the magnetic field frequency's steady shift,  $f_H$  - II: mixing state. (b) The stable behaviours of the material (such as stable output strain amplitude and stable temperature) at various magnetic field frequencies. All simulations are run using a 0.8 T magnetic field amplitude, a 40 s heat relaxation time, and a 20 °C ambient temperature. It should be noted that the material's response frequency is two times the frequency of the applied magnetic field, making the response frequency of the simulated material from 100 Hz to 300 Hz.

The contribution of this section to the existing model of Chen and He (2020) is the study of the behaviour of single crystal NiMnGa alloys actuated by cyclic magnetic fields under various thermo-magnetic loading conditions, taking into account the effects of ambient heat-transfer condition, ambient temperature, applied magnetic field amplitude, and frequency. This study has revealed different material states under dynamic loadings that have not been identified in the literature. Based on these material states under dynamic loadings, the next section will simplify the existing model of Chen and He (2020) presented in Section 4.2 to derive the explicit expressions of material's long-term steady-state behaviours. These explicit expressions will provide a clearer understanding of how the material responds under different thermo-magnetic loading conditions and can be used to quantify the material's response when a stimulus is applied.

#### 4.4. Discussions

This section aims to present new analytic expressions of single crystal NiMnGa alloys' dynamic behaviours as a function of ambient thermal conditions and magnetic loading conditions by taking into account the different material states under dynamic loadings revealed

in Section 4.3 and simplifying the model of Chen and He (2020) presented in Section 4.2. These analytical expressions have never been reported in the literature at the time of study and are vital to the understanding of the single crystal NiMnGa's behaviour and its implementation for the design of engineering systems.

From Section 4.3, it is discovered that the material's state and its stable strain amplitude and temperature are influenced by the thermo-magnetic loading circumstances. These material states are useful for predicting the dynamic behaviour of single crystal NiMnGa under different conditions and the material's response to stimuli. Understanding and optimising these material states are key research challenges in the field of magnetic shape memory alloys. Therefore, the results in this section provide valuable insights into how these material states affect the behaviour of single crystal NiMnGa and will be useful to inform future research and design efforts in single crystal NiMnGa.

The three distinct material states discovered in Section 4.3 are as follows:

- Austenite state

The output strain amplitude is 0 since there is no martensite in this condition, and the material's stable temperature is higher than the typical phase transformation temperature  $T_{PT}$ .

- Mixture state where martensite and austenite coexist

The material's stable temperature is approximately  $T_{PT}$ , and the thermo-magnetic loadings can change the material's stable output strain amplitude.

- Martensite state

The material's stable temperature is below  $T_{PT}$  under this condition. The thermo-magnetic loadings can change both the material's stable temperature and its stable output strain amplitude.

A thorough study of the behaviour of the material in each of these three stable (long-term steady-state) states will be discussed. The understanding of these three states is essential to fully comprehend the thermo-magneto-mechanical properties of single-crystalline NiMnGa alloys under dynamic loadings. The definitions for each parameter used in the subsequent equations are provided in the [List of nomenclature and abbreviations table](#).

#### 4.4.1. Austenite state

In this state, there is no phase change or martensite reorientation. We determine the material's stable temperature: by ignoring the heat generation components resulting from martensite reorientation and phase transition in the heat equation (Eq. (4.9)) and further assuming  $\dot{T} = 0$  (i.e., steady state), the material's stable temperature can be calculated as:

$$T_{stable}^{(A)} = T_0 + \frac{t_h}{\lambda} (4641.4f_H - 1.35 \times 10^5) \quad (4.12a)$$

Since there is no martensite reorientation that is occurring in the austenite state, the material's output strain amplitude is 0:

$$\Delta\varepsilon_{stable}^{(A)} = 0 \quad (4.12b)$$

Equation (4.12a) demonstrates that the material's stable temperature  $T_{stable}^{(A)}$  is always higher than the surrounding temperature  $T_0$ . The heat from the eddy current (caused by the cyclic magnetic field), which is the only heat source in the austenite state, is responsible for the additional temperature (2nd term on the right-hand side of Eq. (4.12a)). Additionally, a weaker ambient heat-transfer condition causes the material's stable temperature to rise with rising heat relaxation time. Eq. (4.12) is presented in Figure 4-3 and Figure 4-4(b) using the parameter values in the [list of nomenclature and abbreviations](#), and there is good agreement with simulation results.

#### 4.4.2. Mixture state where martensite and austenite phases coexist

The constant levels of austenite volume fraction at periods  $t_4$ ,  $t_5$  and  $t_6$  in Figure 4-2(a) demonstrate that the phase change has been completed in the stable state. When the heat equation (Eq. (4.9)) does not take into account the heat generation due to phase transformation and  $\dot{T}$  is equal to 0 (steady state), the following equation is obtained:

$$(4641.4f_H - 1.35 \times 10^5) + \sigma_{tw}^{eff} \varepsilon_0 |\dot{z}_{12}| = \frac{\lambda}{t_h} (T_{stable} - T_0) \quad (4.13)$$

In Eq. (4.13), the components on the left-hand side denote the heat generated by eddy current and martensite reorientation, while the terms on the right-hand side denote the heat transported to the surrounding environment. Eq. (4.13) demonstrates that in a steady state, the produced heat and the emitted heat must be equal. Since the material's response frequency is two times the applied magnetic field frequency, as seen by the magnetised views in Figure 4-2(b), we may integrate Eq. (4.13) for one cycle of the material's response ( $= 1/2f_H$ ), giving us:

$$(4641.4f_H - 1.35 \times 10^5) \frac{1}{2f_H} + 2\sigma_{tw}^{eff} \varepsilon_0 |\Delta z_{12}| = \frac{\lambda}{t_h} (T_{stable} - T_0) \frac{1}{2f_H} \quad (4.14)$$

where  $|\Delta z_{12}|$  is the volume fraction change caused by the cyclic reorientation of martensite between M1 and M2. Since M1 switches to M2 during loading ( $+\Delta z_{12}$ ) and M2 switches back to M1 during unloading ( $-\Delta z_{12}$ ) in the course of one cycle, the second term on the left-hand side of Equation (4.14) is multiplied by "2". The martensite reorientation is mostly responsible for the material's output strain, therefore we have:

$$\Delta \varepsilon_{stable} \approx \varepsilon_0 |\Delta z_{12}| \quad (4.15)$$

Introducing Eqs. (4.5) and (4.15) into Eq. (4.14), we obtain:



$$\begin{aligned} & \Delta \varepsilon_{stable} \\ &= \frac{\frac{\lambda}{t_h} (T_{stable} - T_0) - (4641.4f_H - 1.35 \times 10^5)}{4f_H \left( 0.2 - 0.02 \times (T_{stable} - A_s^0) \times \left( 1 - \tanh \frac{2f_H - 199}{85} \right) \right)} \times 10^6 \end{aligned} \quad (4.16)$$

The material's stable temperature  $T_{stable}$  is close to the characteristic phase transformation temperature in the mixture state (martensite and austenite). Then we have:

$$T_{stable}^{(A\&M)} = T_{PT} \quad (4.17a)$$

$$\begin{aligned} & \Delta \varepsilon_{stable}^{(A\&M)} \\ &= \frac{\frac{\lambda}{t_h} (T_{PT} - T_0) - (4641.4f_H - 1.35 \times 10^5)}{4f_H \left( 0.2 - 0.02 \times (T_{PT} - A_s^0) \times \left( 1 - \tanh \frac{2f_H - 199}{85} \right) \right)} \times 10^6 \end{aligned} \quad (4.17b)$$

The stable strain amplitude is observed to decrease with increasing heat relaxation time  $t_h$ , ambient temperature  $T_0$ , and magnetic field frequency  $f_H$  in Eq. (4.17b). The martensite-to-austenite transition is accelerated when  $t_h$  rises because the ambient heat transmission is less, allowing for more heat to be stored in the material. Consequently, less martensite is left to participate in the cyclic martensite reorientation, which results in a smaller output strain.  $T_0$  and  $f_H$  have comparable outcomes. The martensite-to-austenite transition is pushed forward as  $f_H$  increases because more heat is produced per unit of time owing to faster cyclic martensite reorientation (denominator of Eq. (4.17b)), which results in less martensite and a lower output strain magnitude. The martensite-to-austenite transition speeds up as the ambient temperature  $T_0$  rises, converting more martensite into austenite and reducing the output strain amplitude.

Additionally, it is discovered that Eq. (4.17b) does not include the applied magnetic field amplitude  $\mu_0 H_{amp}^{app}$ , indicating that  $\mu_0 H_{amp}^{app}$  has no impact on the stable strain amplitude. In the mixed state, simulations in Figure 4-5(b) also show a minimal impact of  $\mu_0 H_{amp}^{app}$ . The amount

of martensite still remains in the material, which is governed by the martensite-to-austenite transition, determining the strain amplitude in this condition. The output strain amplitude is not greatly impacted by the applied magnetic field ( $\leq 1 T$ ), which is too small to induce phase transformation in MSMA or appreciably alter the typical phase transition temperature. Equation (4.17) is depicted in Figure 4-3, 4-4(b), 4-5, and 4-7(b), and both simulations and experiments (Figure 4-3) show strong agreement with it.

The boundary between the mixture state and the austenite state is at:  $T_{stable}^{(A)} = T_{stable}^{(A\&M)} = T_{PT}$  and  $\Delta\varepsilon_{stable}^{(A)} = \Delta\varepsilon_{stable}^{(A\&M)} = 0$ . Both equations lead to the following:

$$T_0 + \frac{t_h}{\lambda} (4641.4f_H - 1.35 \times 10^5) = T_{PT} \quad (4.18)$$

Equation (4.18) demonstrates that high ambient temperature  $T_0$  combined with significant eddy current heat production (the second component on the left-hand side) can cause the material to reach the austenite state and provide an output strain of zero. By lowering the magnetic field frequency and/or enhancing the ambient heat transfer conditions, we can minimise the material's temperature and/or the formation of eddy current heat (i.e., reducing  $t_h$ ).

#### 4.4.3. Martensite state

In contrast to the states in the previous subsections, where either the material's stable temperature or its stable output strain amplitude is constant, in this state, both temperature and strain amplitude are subjected to changes depending on the thermo-magnetic loading circumstances. In addition to the equation derived from the heat equation (Eq. (4.16)), a further equation is required to calculate a stable temperature and stable output strain amplitude.

Magnetic actuation causes cyclic martensite reorientation between M1 and M2. The thermodynamic force  $A_{1\leftrightarrow 2}$  for the martensite reorientation is obtained by setting  $z_{01} = z_{02} =$

0 (no phase change in the martensite state) and inserting  $z_1 = z_1^{(0)} - z_{12}$  and  $z_2 = z_2^{(0)} + z_{12}$  in Eq. (4.3) as below:

$$A_{1\leftrightarrow 2} = E\varepsilon_0(\varepsilon - z_{12}\varepsilon_0) - \sigma_0\varepsilon_0 + k(z_1 - z_2) + E_{1\leftrightarrow 2}^H \quad (4.19)$$

M1 transforms into M2 under magnetic loading, increasing output strain. When M1 changes to M2,  $A_{1\leftrightarrow 2} = \sigma_{tw}^{eff} \varepsilon_0$ , in accordance with the material model of martensite reorientation in MSMA (Chen et al., 2014). When the material's output strain is at its greatest, the velocity is zero (local maximum), which means that the damping force (proportional to velocity) is also zero. The enlarged images at  $t_1$ ,  $t_2$  and  $t_3$  in Figure 4-2(b) demonstrate that because the actuation signal (i.e., the input magnetic field) is a triangle wave, the resultant material's reaction (i.e., the output strain) is likewise roughly a triangular wave. In this instance, the material's acceleration is about 0 (continuous slope in the triangle wave) at the point of maximum strain, which results in zero inertial force. The restoring force  $f_{MSMA}$  given by the material is solely balanced by the spring force in this exceptional situation of zero damping force and zero inertial force (see Figure 3-2(b)), therefore we have:

$$\begin{aligned} f_{MSMA} + f_{spring} &= 0 \\ \rightarrow ES(\varepsilon_{max} - z_{12}\varepsilon_0) + k_s l_0 \varepsilon_{max} &= 0 \rightarrow E(\varepsilon_{max} - z_{12}\varepsilon_0) = \\ -\frac{k_s l_0}{S} \varepsilon_{max} \end{aligned} \quad (4.20)$$

Introducing Eq. (4.20) into Eq. (4.19) and setting  $z_1 = 1$  and  $z_2 = 0$  (supposing the material is in pure M1 for M1-to-M2 switching), we obtain:

$$A_{1\leftrightarrow 2} = \sigma_{tw}^{eff} \varepsilon_0 \rightarrow \sigma_{int} - \left( \sigma_0 + \frac{k_s l_0}{S} \varepsilon_{max} \right) + \sigma_H^{(1)} = \sigma_{tw}^{eff} \quad (4.21)$$

where  $\sigma_{int} = \frac{k}{\varepsilon_0}$  and  $\sigma_H^{(1)} (= \frac{E_{1\leftrightarrow 2}^H}{\varepsilon_0})$  is the magneto-stress.

In the case when M2 switches back to M1 during magnetic unloading, the output strain decreases and  $A_{1\leftrightarrow 2} = -\sigma_{tw}^{eff} \varepsilon_0$ . Following similar procedures, the following is obtained:

$$-\sigma_{int} - \left( \sigma_0 + \frac{k_s l_0}{S} \varepsilon_{min} \right) + \sigma_H^{(2)} = -\sigma_{tw}^{eff} \quad (4.22)$$

From Eqs. (4.21), (4.22), and (4.5), the output strain amplitude ( $= \varepsilon_{max} - \varepsilon_{min}$ ) can be estimated as:

$$\begin{aligned} \Delta \varepsilon_{stable} = & \frac{S}{k_s l_0} \left( \Delta \sigma_H + 2 \sigma_{int} \right. \\ & - 2 \\ & \times \left( 0.2 - 0.02 \times (T_{stable} - A_s^0) \times \left( 1 - \tanh \frac{2f_H - 199}{85} \right) \right) \\ & \left. \times 10^6 \right) \end{aligned} \quad (4.23)$$

where  $\Delta \sigma_H = \sigma_H^{(1)} - \sigma_H^{(2)}$ . The size of the applied magnetic field affects the magneto-stresses  $\sigma_H^{(1)}$  and  $\sigma_H^{(2)}$ . The strain in the quasi-static scenario is maximised at the highest applied magnetic field strength of  $\mu_0 H_{amp}^{app}$  and minimised at the minimum magnetic field strength of 0. The strain, however, is maximum at a magnetic field magnitude less than  $\mu_0 H_{amp}^{app}$  and minimum at a magnetic field magnitude greater than 0 in the dynamic situation due to the damping effect of the dynamic system (as demonstrated in Figure 4-2(b)). The magnetic field frequency  $f_H$  affects the phase lag (delay). As a result, the magneto-stress difference  $\Delta \sigma_H (= \sigma_H^{(1)} - \sigma_H^{(2)})$  is a function of both  $f_H$  and  $\mu_0 H_{amp}^{app}$ .

A pair of equations for the material's stable temperature and stable strain amplitude is made up of Equations (4.16) and (4.23). For ease of use, the dimensionless quantities listed in Table 4-1 are used to describe the equation solutions in the dimensionless form (i.e., normalised temperature and strain amplitude):

- If  $\frac{1}{4}A^2 - B < 0$ , with  $A$  and  $B$  being:

$$A = \frac{2N_3N_4/N_6 - N_4N_5 - 1}{N_4^2/N_6} \quad (4.24a)$$

$$B = \frac{N_3^2/N_6 - N_3N_5 - N_1 - N_2}{N_4^2/N_6} \quad (4.24b)$$

The set of equations has no actual solution in this case, since martensite reorientation is not initiated. As a result, the material's output strain amplitude is 0, and Eq. (4.16) can be used to determine the material's temperature as follows:

$$\bar{T}_{stable}^{(M)} = N_1 + N_2 \quad (4.25a)$$

$$\Delta\bar{\epsilon}_{stable}^{(M)} = 0 \quad (4.25b)$$

- If  $\frac{1}{4}A^2 - B \geq 0$ , there is a real solution. By accounting for the boundaries of the normalised strain amplitude ( $\Delta\bar{\epsilon}_{stable} \in [0,1]$ ), we have:

$$\text{When } \frac{\sqrt{\frac{1}{4}A^2 - B + \frac{1}{2}A - N_1 - N_2}}{N_3 - N_4 \left( \sqrt{\frac{1}{4}A^2 - B + \frac{1}{2}A} \right)} < 0:$$

$$\bar{T}_{stable}^{(M)} = N_1 + N_2 \quad (4.25c)$$

$$\Delta\bar{\epsilon}_{stable}^{(M)} = 0 \quad (4.25d)$$

$$\text{When } 0 \leq \frac{\sqrt{\frac{1}{4}A^2 - B + \frac{1}{2}A - N_1 - N_2}}{N_3 - N_4 \left( \sqrt{\frac{1}{4}A^2 - B + \frac{1}{2}A} \right)} \leq 1:$$

$$\bar{T}_{stable}^{(M)} = \sqrt{\frac{1}{4}A^2 - B + \frac{1}{2}A} \quad (4.25e)$$

$$\Delta \bar{\epsilon}_{stable}^{(M)} = \frac{\sqrt{\frac{1}{4}A^2 - B + \frac{1}{2}A} - N_1 - N_2}{N_3 - N_4 \left( \sqrt{\frac{1}{4}A^2 - B + \frac{1}{2}A} \right)} \quad (4.25f)$$

$$\text{When } \frac{\sqrt{\frac{1}{4}A^2 - B + \frac{1}{2}A} - N_1 - N_2}{N_3 - N_4 \left( \sqrt{\frac{1}{4}A^2 - B + \frac{1}{2}A} \right)} > 1:$$

$$\bar{T}_{stable}^{(M)} = \frac{N_1 + N_2 + N_3}{1 + N_4} \quad (4.25g)$$

$$\Delta \bar{\epsilon}_{stable}^{(M)} = 1 \quad (4.25h)$$

It is still unclear what the exact form of  $\Delta \sigma_H(\mu_0 H_{amp}^{app}, f_H)$  is. However, if  $\mu_0 H_{amp}^{app}$  and  $f_H$  are constants, we may accept  $\Delta \sigma_H$  as a constant. For the variable ambient thermal conditions and constant magnetic loading circumstances, i.e., constant  $\mu_0 H_{amp}^{app}$  and  $f_H$ , Eq. (4.25) is plotted in Figure 4-3 and 4.4(b) by using  $\Delta \sigma_H(\mu_0 H_{amp}^{app}, f_H) = 1.53$  MPa (best match with the experiments in Figure 4-3) and using the parameter values from the [list of nomenclature and abbreviations](#). Agreement with simulations was found.

The boundary between the martensite state and the mixture state (martensite and austenite) is defined as follows:  $\bar{T}_{stable}^{(M)} = \bar{T}_{stable}^{(A\&M)} = 1$  and  $\Delta \bar{\epsilon}_{stable}^{(M)} = \Delta \bar{\epsilon}_{stable}^{(A\&M)}$ . By normalising Eq. (4.17) and utilising the dimensionless values in Table 4-1, it is possible to determine the dimensionless stable temperature  $\bar{T}_{stable}^{(A\&M)}$  and stable strain amplitude  $\Delta \bar{\epsilon}_{stable}^{(A\&M)}$  in the mixed state as:

$$\bar{T}_{stable}^{(A\&M)} = 1 \quad (4.26a)$$

$$\Delta \bar{\epsilon}_{stable}^{(A\&M)} = \frac{1 - N_1 - N_2}{N_3 - N_4} \quad (4.26b)$$

Then the boundary between the martensite and the mixture state can be further calculated with the aid of Eqs. (4.25) and (4.26) as below:

- If  $\frac{1}{4}A^2 - B < 0$ , with  $A$  and  $B$  being given in Eq. (4.24):

$$N_1 + N_2 = 1 \quad (4.27a)$$

- If  $\frac{1}{4}A^2 - B \geq 0$ :

$$\text{When } \frac{\sqrt{\frac{1}{4}A^2 - B + \frac{1}{2}A - N_1 - N_2}}{N_3 - N_4 \left( \sqrt{\frac{1}{4}A^2 - B + \frac{1}{2}A} \right)} < 0: \quad N_1 + N_2 = 1 \quad (4.27b)$$

$$\text{When } 0 \leq \frac{\sqrt{\frac{1}{4}A^2 - B + \frac{1}{2}A - N_1 - N_2}}{N_3 - N_4 \left( \sqrt{\frac{1}{4}A^2 - B + \frac{1}{2}A} \right)} \leq 1: \quad \sqrt{\frac{1}{4}A^2 - B + \frac{1}{2}A} = 1 \quad (4.27c)$$

$$\text{When } \frac{\sqrt{\frac{1}{4}A^2 - B + \frac{1}{2}A - N_1 - N_2}}{N_3 - N_4 \left( \sqrt{\frac{1}{4}A^2 - B + \frac{1}{2}A} \right)} > 1: \quad N_1 + N_2 + N_3 - N_4 = 1 \quad (4.27d)$$

Table 4-1. Dimensionless parameters adopted in Chapter 4.

$N_1$	<b>Normalised ambient temperature</b>	$\frac{T_0}{T_{PT}}$
$N_2$	Normalised heat from eddy current	$\frac{4641.4f_H - 1.35 \times 10^5}{T_{PT}\lambda/t_h}$
$N_3$	Normalised dissipation due to martensite reorientation at 0 °C	$\frac{4t_h f_H \epsilon_0}{T_{PT}\lambda} \left( 2 \times 10^5 + 2 \times 10^4 \times A_S^0 \times \left( 1 - \tanh \frac{2f_H - 199}{85} \right) \right)$

$N_4$	Dimensionless temperature coefficient for dissipation of martensite reorientation	$8 \times 10^4 \times \frac{t_h f_H \varepsilon_0}{\lambda} \left(1 - \tanh \frac{2f_H - 199}{85}\right)$
$N_5$	Normalised total stress, including the effect of magnetic field and interaction	$\frac{\Delta \sigma_H (\mu_0 H_{amp}^{app} f_H) + \frac{2k}{\varepsilon_0}}{k_s l_0 \varepsilon_0 / S}$
$N_6$	Normalised spring energy	$\frac{2f_H k_s l_0 \varepsilon_0^2 / S}{T_{PT} \lambda / t_h}$
$\bar{T}_{stable}$	Normalised material's stable temperature	$\frac{T_{stable}}{T_{PT}}$
$\Delta \bar{\varepsilon}_{stable}$	Normalised material's stable output strain amplitude	$\frac{\Delta \varepsilon_{stable}}{\varepsilon_0}$

## 4.5. Chapter conclusion

This chapter examines the impact of thermo-magnetic loading conditions on the high frequency (> 100 Hz) long-term (> 100 s) dynamic behaviour of magnetic shape memory alloys driven by cyclic magnetic fields. The studied thermo-magnetic loading conditions include the ambient thermal conditions of ambient temperature and ambient heat transfer and the magnetic loading conditions of magnetic field frequency and amplitude. The key findings are as follows:

1. The material's stable temperature is always higher than the surrounding temperature due to heat generated from eddy currents and intrinsic dissipation during magnetic-field-induced cyclic martensite reorientation. This can lead to phase transformations and mixed material states where both martensite and austenite are present.



2. Thermo-magnetic loading conditions can influence the material's stable temperature and state. Factors such as weak ambient heat transfer, high ambient temperature, and high magnetic field amplitude can cause the material to transform from martensite to a mixed state or even to an austenite state.
3. The material's stable strain depends on its stable state. Output strain amplitude varies based on the presence of martensite and the temperature-driven martensite-to-austenite transition.
4. Thermo-magnetic loading conditions can alter the material's stable strain amplitude in martensite and mixed states. Greater net heat production and promotion of martensite-to-austenite transformation can lead to less martensite remaining and lower strain amplitude in the mixed state.
5. Analytical expressions of the material's stable temperature and stable output strain amplitude are developed based on ambient thermal parameters and magnetic loading conditions. This model can guide the control of output strain and operating temperature for magnetic shape memory alloy-based actuators, improving their reliability.

## 5. Kinetics of temperature-induced phase transformations in Ni-Mn-Ga single crystal

### 5.1. Introduction

Shape memory alloys undergo temperature-induced phase transformations between martensite and austenite during heating and cooling. Four key temperatures are identified in this process:  $A_s$  (austenite start temperature),  $A_f$  (austenite finish temperature),  $M_s$  (martensite start temperature), and  $M_f$  (martensite finish temperature) (Figure 5-1). The martensite-to-austenite transition starts at  $A_s$  (Point B) when the alloy's temperature rises and the new austenite phase nucleates. This transformation continues until the pure austenite state is reached at  $A_f$  (Point C in Figure 5-1). When cooled, the austenite-to-martensite transition begins at  $M_s$  (Point E in Figure 5-1), with fresh martensite nucleating. The process concludes at  $M_f$  (Point F in Figure 5-1) when the sample is in the pure martensite state.

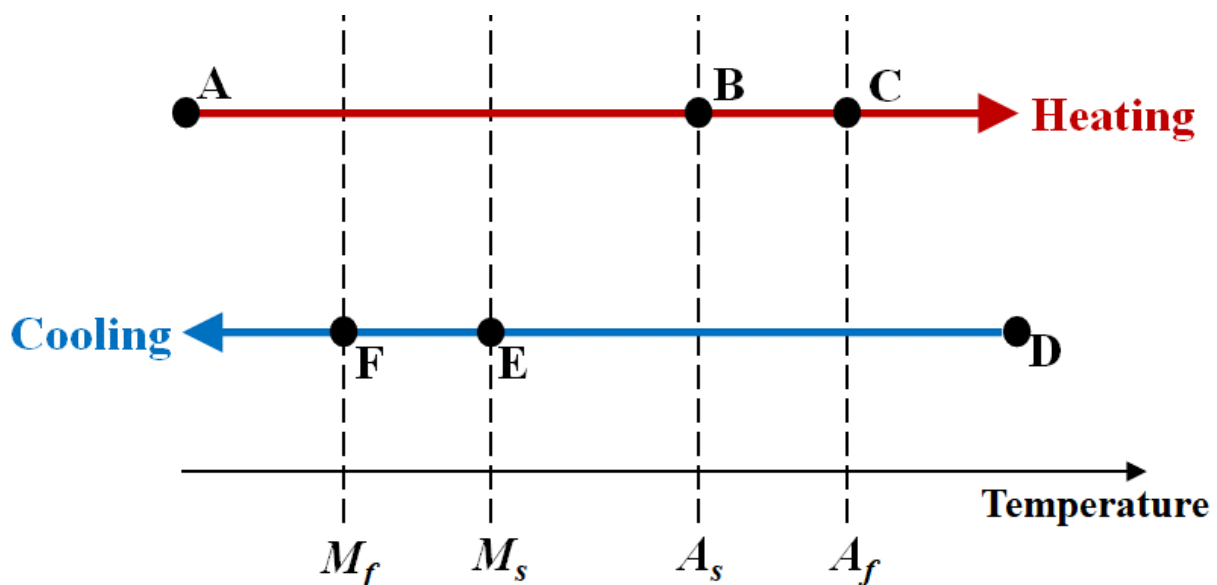


Figure 5-1. Temperature-induced phase transformations in shape memory alloys. Four characteristic temperatures are identified:  $A_s$  (austenite start temperature),  $A_f$  (austenite finish temperature),  $M_s$  (martensite start temperature), and  $M_f$  (martensite finish temperature).

Although generally believed that without mechanical stress, the martensite-to-austenite transition requires temperatures at or above  $A_s$ , recent studies on dynamic behaviours of

magnetic shape memory alloys found that high-frequency magnetic fields can trigger this transformation below  $A_s$ , and sometimes near  $M_s$  (Zhang et al., 2018a, Zhang et al., 2018b). The magnetic field-induced martensite reorientation generates dissipated heat, causing the phase transformation. A systematic investigation of this phenomenon has yet to be conducted in the literature.

In this chapter, we conduct systematic experiments to investigate the temperature-induced austenite-to-martensite transition above  $M_s$  and the martensite-to-austenite transformation below  $A_s$ . The remainder of the chapter is divided into the following sections: information about the experiments and tested materials is presented in Section 5.2. The experimental findings and discussions on phase transformation kinetics are provided in Section 5.3. Section 5.4 gives a summary and conclusions.

## 5.2. Material properties and experimental setup

Samples of single crystal  $\text{Ni}_{50}\text{Mn}_{28}\text{Ga}_{22}$  (at. %) shape memory alloys purchased from Goodfellow Cambridge Ltd. are used in the experiments. All samples are rectangular bars with the nominal dimension of  $1 \text{ mm} \times 2.5 \text{ mm} \times 20 \text{ mm}$ , and all faces of the bars are approximately parallel to the  $\{100\}$  planes of the parent cubic austenite. Two sets of samples are tested. The first set (Set I) has the characteristic phase transformation temperatures  $M_s = 39 \pm 1.0 \text{ }^\circ\text{C}$ ,  $M_f = 36 \pm 1.0 \text{ }^\circ\text{C}$ ,  $A_s = 52 \pm 2.0 \text{ }^\circ\text{C}$ ,  $A_f = 54 \pm 2.0 \text{ }^\circ\text{C}$ , and this set has a relatively large hysteresis:  $A_s - M_s = 13 \pm 3.0 \text{ }^\circ\text{C}$ . The second set (Set II) has the characteristic phase transformation temperatures  $M_s = 33.5 \pm 1.0 \text{ }^\circ\text{C}$ ,  $M_f = 32.8 \pm 1.0 \text{ }^\circ\text{C}$ ,  $A_s = 40 \pm 1.5 \text{ }^\circ\text{C}$ ,  $A_f = 41 \pm 1.5 \text{ }^\circ\text{C}$ , and this set has a relatively small hysteresis:  $A_s - M_s = 6.5 \pm 2.5 \text{ }^\circ\text{C}$ . The phase transformation temperatures are measured by the DIC (digital image correlation) technique detailed in Appendix A.

At room temperature, all samples are in the state of 5M modulated martensite phase. The martensite variants are slightly monoclinic with  $\gamma = 90.37^\circ$  (Chulist et al., 2013). For simplicity, the martensite variants are approximated as a tetragonal lattice with two long axes  $a$  and one short axis  $c$ . Therefore, there are totally three martensite variants, i.e.,  $M_1$ ,  $M_2$  and  $M_3$ , with their short  $c$ -axis, respectively along  $x$ ,  $y$  and  $z$  coordinates, as shown in Figure 5-2. This simplification has been widely used in the studies on  $\text{Ni}_{50}\text{Mn}_{28}\text{Ga}_{22}$  single crystals (Bronstein et al., 2019; Haldar et al., 2014; Karaca et al., 2006; Pinneker et al., 2014).

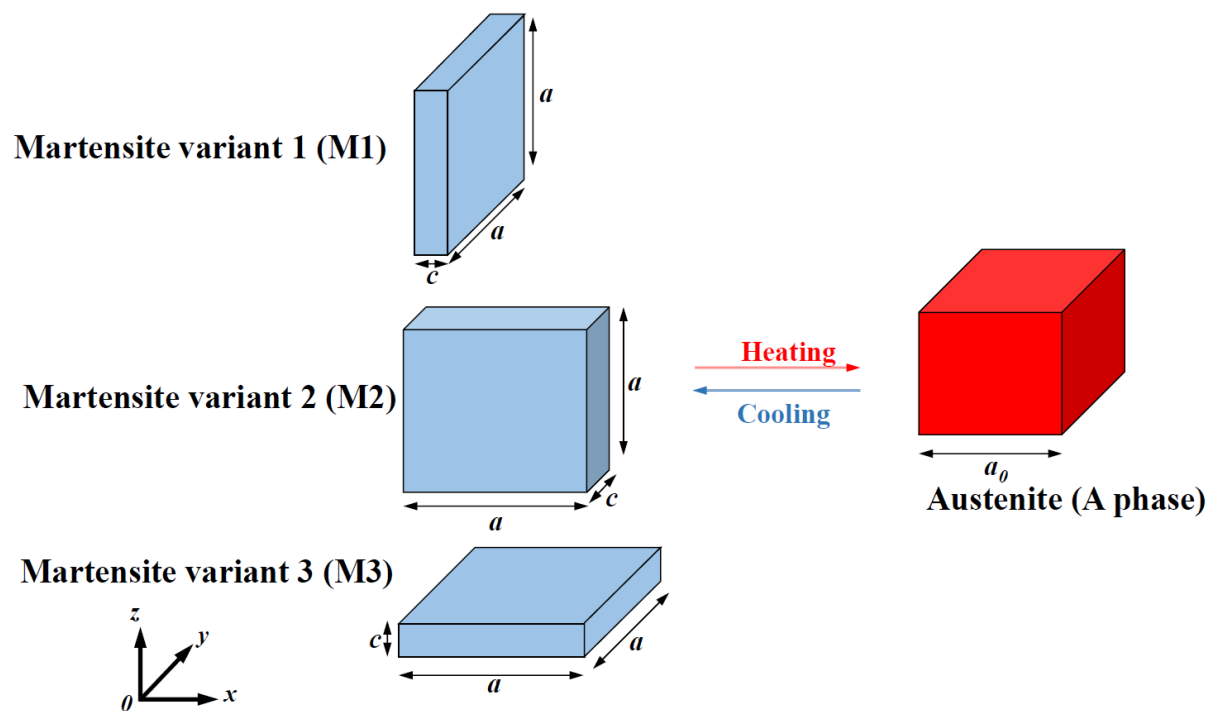


Figure 5-2. Schematic diagram of the austenite and the martensite variants of Ni–Mn–Ga shape memory alloys: pseudo-tetragonal martensite lattice with the long axis of length  $a$  and short axis of length  $c$ , and cubic austenite lattice with length  $a_0$ .

In Figure 3-11 and Figure 5-3, the experimental setup is shown. The sample is put on a PLA 3D-printed sample holder (Polylactic acid thermoplastic). The sample is in the free state during the tests, meaning no mechanical force or magnetic field is applied. A heat gun (Seekone heat 2000W gun) is employed to produce hot air. The sample is heated by thermal convection as the air passes through it. The temperature of the sample is measured using a thermocouple (T-type thermocouple with probes made of copper wire) affixed to the side surface of the

sample. The thermocouple has a resolution/precision of 0.75% or 1.0 °C (Thermocoupleinfo (2011)). Using two distinct T-type thermocouples, preliminary tests are carried out at various places (the top surface and side surface) (details in Appendix B), and it is discovered that the variation in recorded temperatures at various sites is less than 1.5 °C (Appendix B). Therefore, one thermocouple can be used to measure the sample temperature since the sample temperature will remain roughly uniform throughout the experiment. A tiny bit of thermal paste is applied to the tip of the thermocouple to aid the transfer of heat from the Ni-Mn-Ga sample. This has proven to improve the accuracy of temperature measurement while using a temperature probe.

Phase transformation in single crystal Ni-Mn-Ga shape memory alloys takes place by the nucleation and propagation of the austenite-martensite (A-M) interface. The austenite and martensite are separated by this A-M interface. As a result, there is an abrupt strain change across this interface. When using the austenite phase as the reference (i.e., zero strains), with the observed lattice parameters:  $a_0 \approx 0.584$  nm for austenite,  $a \approx 0.595$  nm, and  $c \approx 0.561$  nm for martensite (Heczko et al., 2002, Straka et al., 2008), the normal strains of the three martensite variations are as follows:  $\varepsilon_{xx} \approx -4\%$  and  $\varepsilon_{yy} \approx 2\%$  for  $M_1$ ,  $\varepsilon_{xx} \approx 2\%$  and  $\varepsilon_{yy} \approx -4\%$  for  $M_2$ ,  $\varepsilon_{xx} \approx 2\%$  and  $\varepsilon_{yy} \approx 2\%$  for  $M_3$ . Therefore, the A-M interface (represented by a change in strain) may be located, and the progress of the phase transformation can be observed by measuring the local strain distribution. The top surface of the sample, or the x-y plane, is seen using a tiny microscope (Bindpo USB digital microscope with 5 Megapixels and a recording rate of 30 fps). To determine the local strain distribution, images from the microscope are processed using the open-source 2-D DIC analyser published by Blaber et al. (2015), utilising the digital image correlation (DIC) approach (further information on the DIC may be found in Chapter 3). Figure 5-4 illustrates an example of the austenite-martensite interface that is captured by the DIC. A PC synchronises the thermocouple temperature measurement, pictures from the small microscope, and heat gun control throughout each test.

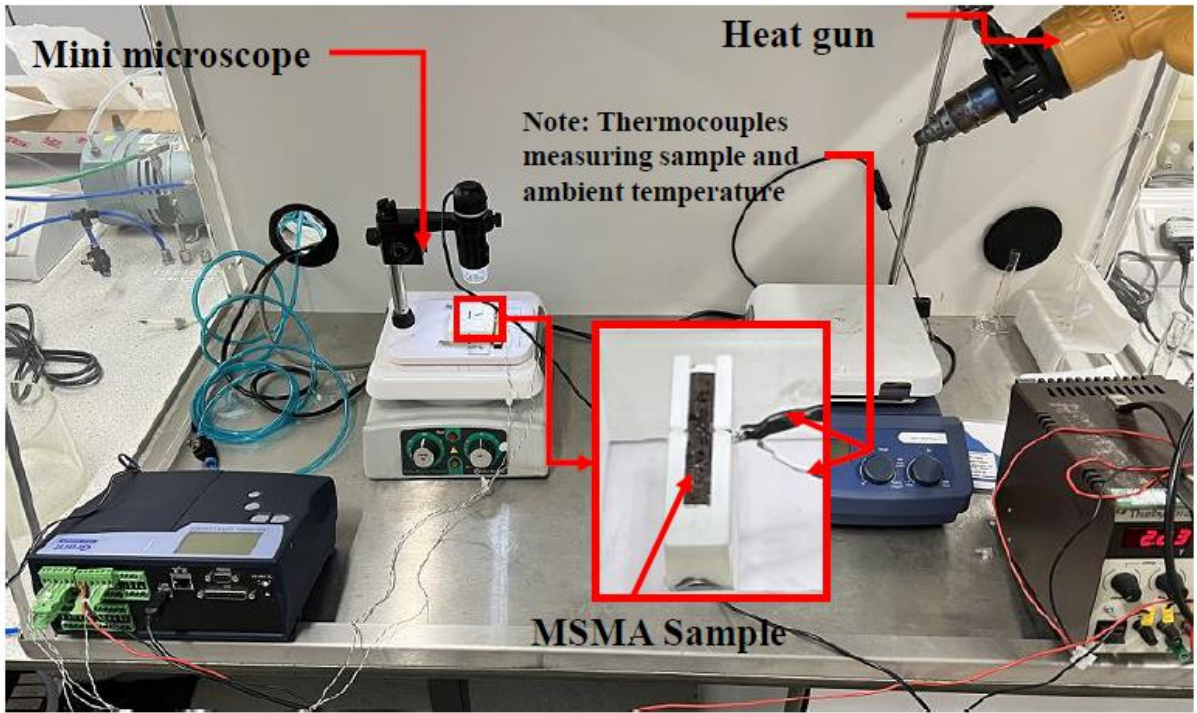


Figure 5-3. Photo of experimental setup.

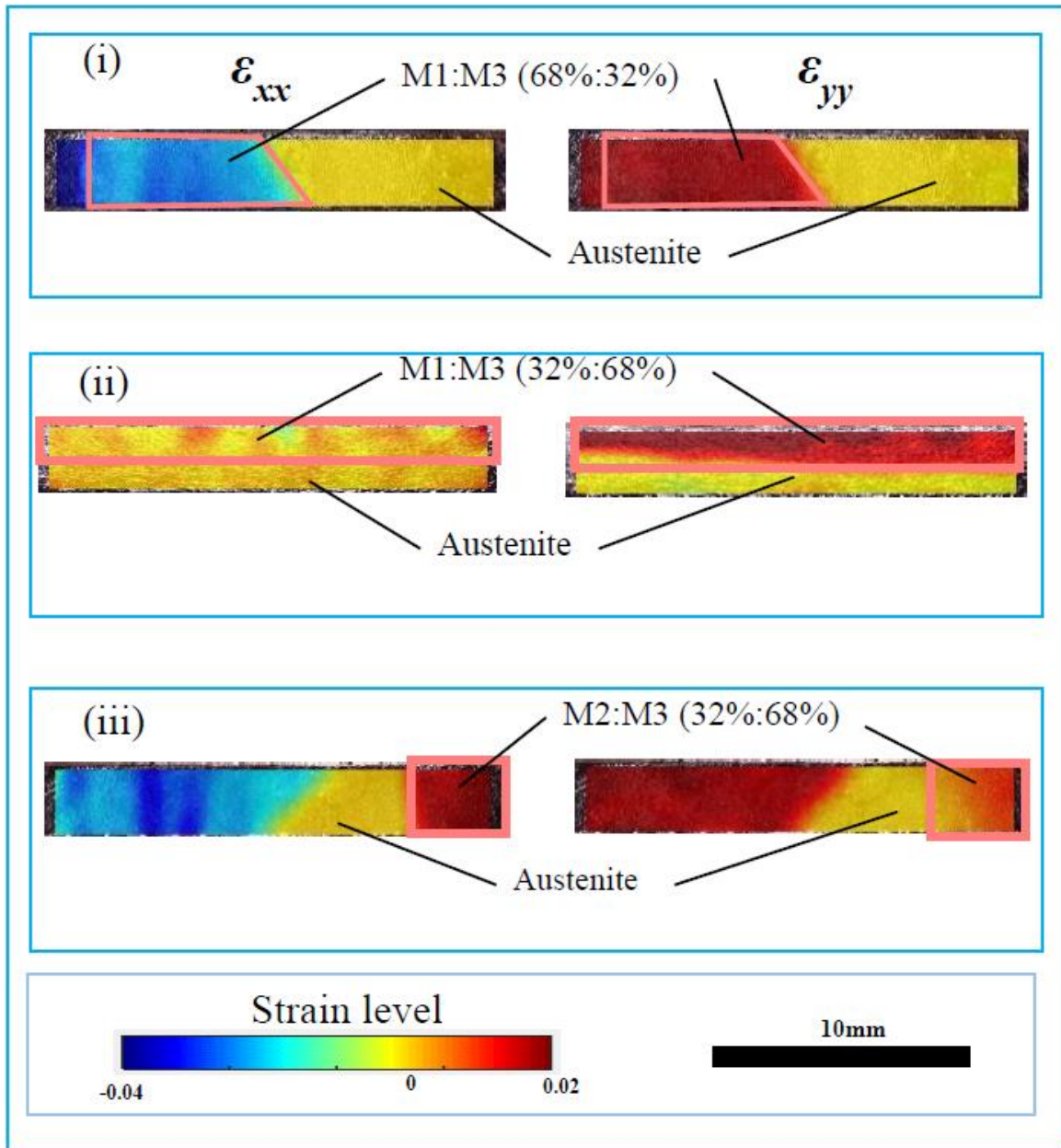


Figure 5-4. Example of austenite-martensite (A-M) interface identified in DIC images

There are two different types of tests that are conducted. These two tests are conducted to identify the two new critical temperatures that can be observed during the temperature-induced phase transformations of shape memory alloys. For the first type (Test I), the sample is cooled to room temperature and compressed along the x-axis at the start of each test to place it in the starting condition of a single martensite variation  $M_1$ . The sample is then heated using a heat gun to blow hot air flow on the sample. The sample temperature rises steadily at a heating rate of about  $0.024 \text{ }^\circ\text{C/s}$  (Appendix B). The heat gun is turned off after the typical austenite

start temperature ( $A_s$ ) is achieved (or just slightly exceeded,  $< 1$  °C), and the sample is cooled down naturally at an average rate of around 0.029 °C/s.

For the second kind of test (Test II), the sample is heated by the heat gun at the start of each test to a temperature that is around 10 °C higher than the typical austenite finish temperature ( $A_f$ ), in order to put the sample in the initial condition of pure austenite. The heat gun is then turned off, and the sample is cooled down naturally at an average rate of around 0.029 °C/s. When the sample temperature drops to the typical martensite start temperature ( $M_s$ ) or drops just below  $M_s$  ( $< 1$  °C), the heat gun is turned on again, and the sample is heated at an average heating rate of around 0.024 °C/s

### 5.3. Results and discussions







#### 5.3.1. Test I: martensite-to-austenite transformation triggered by heating









Table 5-1 displays a typical example of Test I. The sample is in the starting condition of martensite variation M1, which contains the strains  $\epsilon_{xx} \approx -4\%$  and  $\epsilon_{yy} \approx 2\%$ , at the start of the test or at 0 seconds (see DIC images at 0 s in Table 5-1). When the sample is then heated, just before the sample temperature reaches the characteristic austenite start temperature  $A_s$ , the DIC image is still unchanged, as seen at 50 s in Table 5-1, indicating the phase transformation has not begun. The new austenite phase begins to form at 55 seconds after  $A_s$  (51.4 °C) is achieved. Then the martensite-to-austenite transformation takes place by the propagation of an austenite-martensite interface (A-M interface), which is visible and identified by the interface separating the domain with nearly 0 strains (austenite) and the one with  $\epsilon_{xx} \approx -4\%$  and  $\epsilon_{yy} \approx 2\%$  ( $M_1$ ) at 57.0 s in Table 5-1. At 59.0 seconds, the heat gun is turned off, and the sample temperature begins to drop from 52.1 °C. It is surprising to see that the martensite-to-austenite transformation continues as the sample temperature decreases below  $A_s$ , rather than stopping as is typically acknowledged or assumed (see the DIC images at 61–68 s), and the transformation



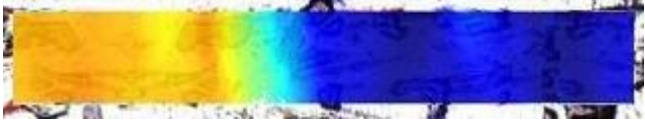







finally comes to an end at a temperature much lower than  $A_s$  (51.4 °C), i.e., 46.1 °C at 75 s in Table 5-1. In this chapter, this temperature is referred to as the austenite stop temperature ( $A_{stop}$ ). The unchanging DIC pictures at 100 seconds in Table 5-1 demonstrate that the martensite-to-austenite transition does not occur when the sample temperature is further lowered below  $A_{stop}$ .

Table 5-1. A typical example of Test I results: sample is heated to the characteristic austenite start temperature ( $A_s$ ) and then cooled down naturally.

Time	Sample temperature	DIC images on the x-y plane
0 s	22.6 °C	Colour bar  Scale bar  $\epsilon_{xx}$  $\epsilon_{yy}$ 
51 s	50.0 °C	$\epsilon_{xx}$  $\epsilon_{yy}$ 
55 s	51.4 °C ( $A_s$ )	$\epsilon_{xx}$

Time	Sample temperature	DIC images on the $x$ - $y$ plane
		 <p data-bbox="671 439 708 465"><math>\epsilon_{yy}</math></p> 
57 s	51.9 °C	<p data-bbox="671 667 708 694"><math>\epsilon_{xx}</math></p>  <p data-bbox="671 898 708 925"><math>\epsilon_{yy}</math></p> 
59 s	52.1 °C (switched off heat gun)	<p data-bbox="671 1131 708 1158"><math>\epsilon_{xx}</math></p>  <p data-bbox="671 1361 708 1388"><math>\epsilon_{yy}</math></p> 
61 s	52.0 °C	<p data-bbox="671 1594 708 1621"><math>\epsilon_{xx}</math></p>  <p data-bbox="671 1825 708 1852"><math>\epsilon_{yy}</math></p> 


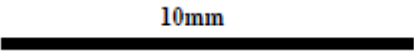





Time	Sample temperature	DIC images on the $x$ - $y$ plane
64 s	51.1 °C	$\epsilon_{xx}$  $\epsilon_{yy}$ 
68 s	50.3 °C	$\epsilon_{xx}$  $\epsilon_{yy}$ 
75 s	46.1 °C ( $A_{stop}$ )	$\epsilon_{xx}$  $\epsilon_{yy}$ 
100 s	41.8 °C	$\epsilon_{xx}$  $\epsilon_{yy}$




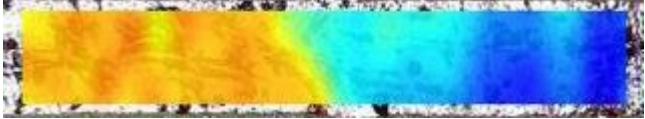




Time	Sample temperature	DIC images on the $x$ - $y$ plane
		








### 5.3.2. Test II: Austenite-to-martensite transformation triggered by cooling

A typical example of Test II is shown in Table 5-2. The material is initially in an austenite condition with almost no stresses at the start of the test (0 s) (see DIC images at 0 s in Table 5-2). The sample is then allowed to cool down naturally. The austenite-to-martensite transition is not activated until the sample temperature drops to the typical martensite start temperature  $M_s$ , resulting in almost unaltered DIC pictures at 83 s in Table 5-2. The new martensite phase begins to form at 229 s, when  $M_s$  (39.2°C) is attained. The austenite-to-martensite transformation is then caused by the propagation of an austenite-martensite interface (A-M interface), which is distinguished by the interface separating the domain with almost zero strains (austenite) and the one with  $\epsilon_{xx} \approx -2\%$  and  $\epsilon_{yy} \approx 0\%$  (martensite twin composed of M1 and M3) at 262 s in Table 5-2. At 282 seconds, the heat gun is turned on, and the sample temperature begins to rise from 38.5 °C. Surprisingly, the austenite-to-martensite transformation continues as the sample temperature rises above  $M_s$  rather than stopping as is typically acknowledged or assumed (see the DIC images at 285–296 s), and it finally comes to an end at a temperature much higher than  $M_s$  (39.2 °C), i.e. 43.0 °C at 298 s in Table 5-2. The term " $M_{stop}$ " temperature is used to describe this temperature. The unmodified DIC pictures at 324 s in Table 5-2 demonstrate that the austenite-to-martensite transition does not occur when the sample temperature is raised further above  $M_{stop}$ .

Table 5-2. A typical example of Test II results: sample is cooled down naturally from a temperature around 10 °C higher than the characteristic austenite finish temperature ( $A_f$ ) to the characteristic martensite start temperature ( $M_s$ ), and then the sample is heated.

Time	Sample temperature	DIC images on the $x$ - $y$ plane
0 s	65.8 °C	<p data-bbox="671 409 815 443">Colour bar</p>  <p data-bbox="671 577 794 611">Scale bar</p>  <p data-bbox="671 752 708 786"><math>\epsilon_{xx}</math></p>  <p data-bbox="671 981 708 1014"><math>\epsilon_{yy}</math></p> 
83 s	45.0 °C	<p data-bbox="671 1211 708 1245"><math>\epsilon_{xx}</math></p>  <p data-bbox="671 1440 708 1473"><math>\epsilon_{yy}</math></p> 
229 s	39.2 °C ( $M_s$ )	<p data-bbox="671 1671 708 1704"><math>\epsilon_{xx}</math></p>  <p data-bbox="671 1899 708 1933"><math>\epsilon_{yy}</math></p>

Time	Sample temperature	DIC images on the $x$ - $y$ plane
		
262 s	39.0 °C	$\epsilon_{xx}$  $\epsilon_{yy}$ 
282 s	38.5 °C (switched on heat gun)	$\epsilon_{xx}$  $\epsilon_{yy}$ 
285 s	38.2 °C	$\epsilon_{xx}$  $\epsilon_{yy}$ 
292 s	39.0 °C	$\epsilon_{xx}$ 

Time	Sample temperature	DIC images on the $x$ - $y$ plane
		$\epsilon_{yy}$ 
296 s	41.1 °C	$\epsilon_{xx}$  $\epsilon_{yy}$ 
298 s	43.0 °C ( $M_{stop}$ )	$\epsilon_{xx}$  $\epsilon_{yy}$ 
324 s	50.1 °C	$\epsilon_{xx}$  $\epsilon_{yy}$ 

### 5.3.3. Kinetics of phase transformation

Two groups of samples each have a distinct thermal hysteresis. Two samples make up each group. Both Test I and Test II are performed on each sample, and each kind of test is repeated for three cycles. All of the raw experimental data is provided in Appendix C, along with a summary of the measured  $A_s$  (characteristic austenite start temperature),  $A_{stop}$  (austenite stop temperature, only defined in the chapter),  $M_s$  (characteristic martensite start temperature), and  $M_{stop}$  (martensite stop temperature, only defined in this chapter) from all tests.  $A_s$  can be observed from Figure 5-5, (for the samples with high thermal hysteresis, i.e., Set I with  $A_s - M_s = 12.7 \pm 0.3$  °C: the difference between  $A_s$  and  $A_{stop}$  and the difference between  $M_s$  and  $M_{stop}$  are significant)  $A_{stop}$  is nearly 5.5 °C lower than  $A_s$ , and  $M_{stop}$  is nearly 4.0 °C higher than  $M_s$ . While for the samples with relatively small thermal hysteresis, i.e., Set II with  $A_s - M_s = 9.6 \pm 0.2$  °C,  $A_{stop}$  is slightly lower than  $A_s$  (difference < 5.3 °C) and  $M_{stop}$  is slightly higher than  $M_s$  (difference < 2.2 °C).

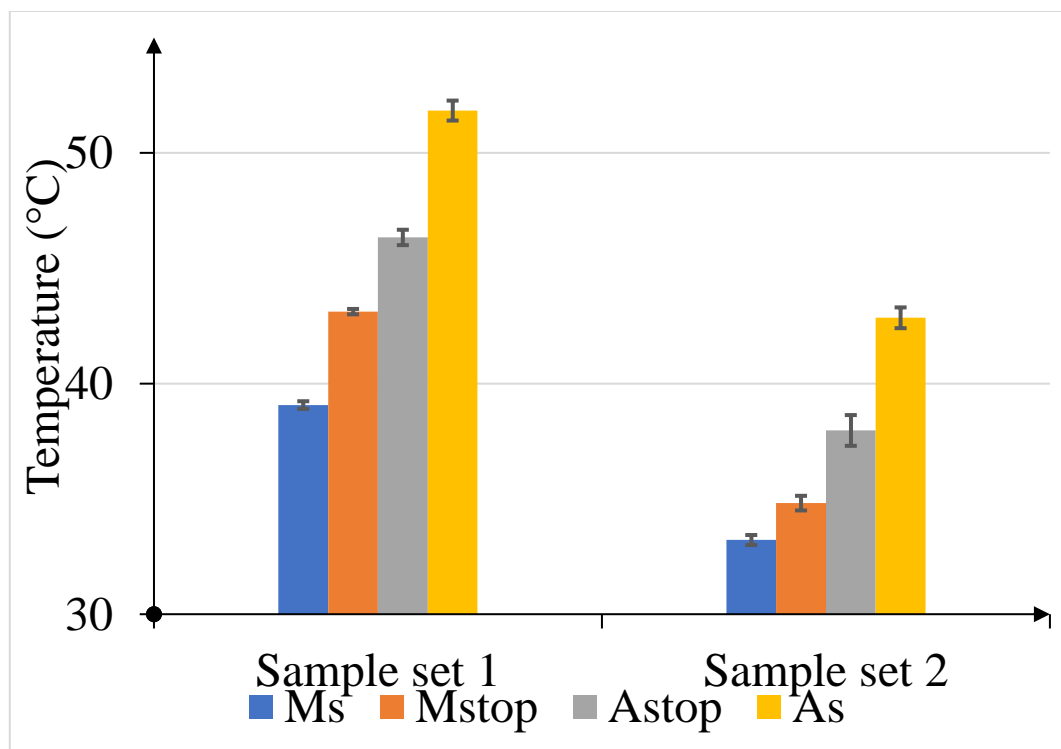


Figure 5-5. Summary of the measured  $A_s$  (characteristic austenite start temperature),  $A_{stop}$  (austenite stop temperature, only defined in the chapter),  $M_s$  (characteristic martensite start temperature), and  $M_{stop}$  (martensite stop temperature, only defined in the chapter) from all tests.



According to the test summary in Figure 5-5,  $A_{stop}$  is always lower than  $A_s$ , and  $M_{stop}$  is always higher than  $M_s$ , which means the austenite-to-martensite transformation continues at an increasing temperature above  $M_s$  (with external heat intake) while the martensite-to-austenite transformation continues at a decreasing temperature below  $A_s$  (without any external heat intake). This observation goes against common sense/assumed knowledge that in order to promote or advance the austenite-to-martensite transformation, heat must be removed from the sample in order to maintain a temperature around or below  $M_s$ , while in order to keep the temperature above  $A_s$ , heat must be added to the sample in order to promote or advance the martensite-to-austenite transformation.

The new phases (i.e., austenite and martensite) emerge as the critical temperatures of  $A_s$  and  $M_s$  are reached. They may be regarded as the temperatures at which nucleation and appearance of new phases occur. The temperatures for the austenite-martensite interface motion may be different. Traditional shape memory alloys that are subject to stress-induced phase transformation often experience a quick stress drop and an avalanche-like process when a new phase first forms. An illustration of the typical stress-strain curve for the stress-induced phase transformation of shape memory alloys (super-elasticity) is shown schematically in Figure 5-6. The nucleation stress of the new martensite phase is visible as a peak stress during the forward martensitic transformation (see Figure 5-6). A lower stress plateau follows, which represents the stress for the forward A-M interface motion (i.e., martensite propagation). During the reverse martensitic transformation, a nadir stress is seen (see Figure 5-6), which represents the nucleation stress of the austenite phase. A higher stress plateau for the reverse A-M interface motion (i.e., austenite propagation) follows the nadir stress. With the analogy to the temperature-induced phase transformation, the peak stress is comparable to the  $A_s$  temperature in terms of the temperature-induced phase transformation, and the lower plateau stress that follows is comparable to the  $A_{stop}$  temperature, indicating that the nucleation

temperature of austenite is greater than its propagation temperature. The nadir stress for the reverse transition is an analogy to the  $M_s$  temperature, and the greater plateau stress that follows is in analogy to the  $M_{stop}$  temperature, indicating that the martensite phase's nucleation temperature is higher than its propagation temperature.

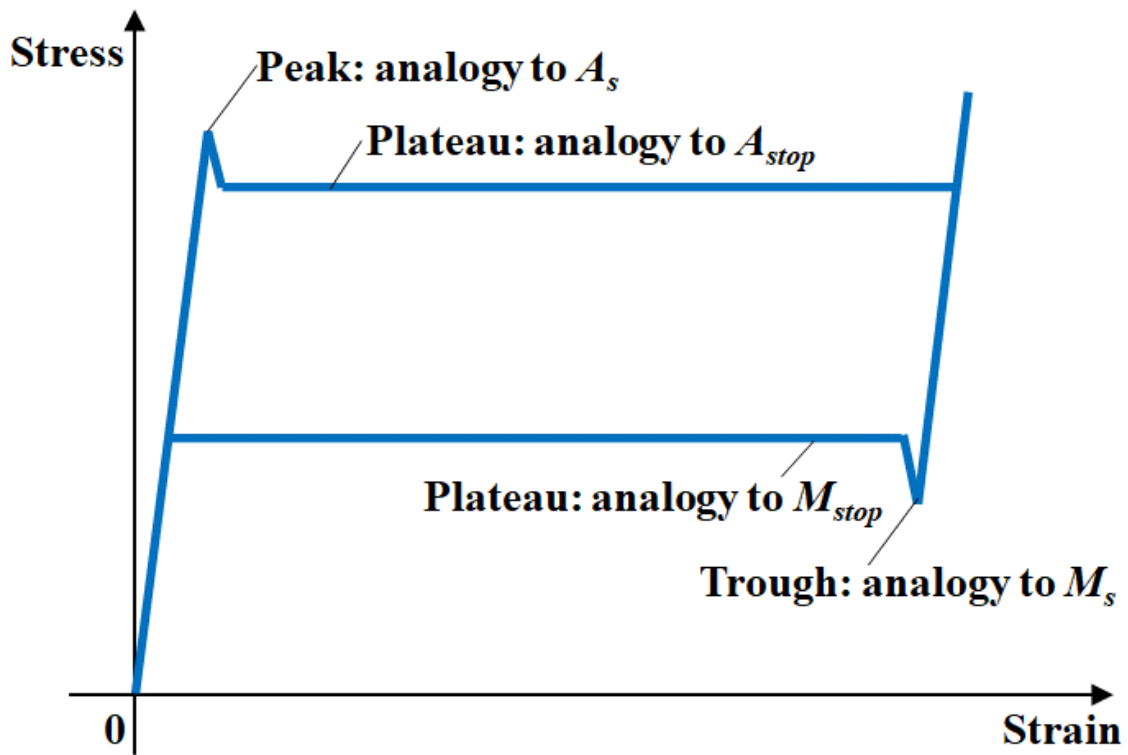


Figure 5-6. Schematic diagram of typical stress–strain curve for stress-induced phase transformation in shape memory alloys (super-elasticity).

For the temperature-induced phase transformation, its thermodynamic force  $A_0$  is just the internal energy difference between austenite and martensite. Its expression can be obtained by neglecting the effect of mechanical stress and magnetic field (Chen and He, 2020):

$$A_0 = U_A - U_M = c_0 - c_1 T = -c_1 \left( T - \frac{c_0}{c_1} \right) = -c_1 (T - T_0) = -c_1 \Delta T \quad (5.1)$$

where  $c_0$  is the internal energy difference between austenite and martensite at 0 K and  $c_1$  is the entropy difference between austenite and martensite at 0 K.  $T_0 (= \frac{c_0}{c_1})$  is the temperature at which the two phases have equal internal energy.  $T_0$  can be approximately estimated as:

$$T_0 \approx \frac{1}{2}(M_s + A_s) \quad (5.2)$$

From equation 5.1,  $A_0$  is proportional to the temperature difference  $\Delta T$  ( $= (T - T_0)$ ).  $\Delta T$  can therefore be used to quantify the thermodynamic force for the temperature-induced phase transformation.

During the experiment, after the heat gun is switched off (in Test I), or switched on (during Test II), the sample temperature decreases (for Test I), or increases (for Test II), and the A-M interface motion continues until the temperature  $A_{stop}$  (Test I) or  $M_{stop}$  (Test II) is reached. Therefore, the average value of  $\Delta T$  and the average speed  $\bar{v}$  of the austenite-martensite interface motion can be calculated with the below equations:

$$\text{Test I: } \Delta\bar{T} = \frac{1}{2}(T_{switch-off} + A_{stop}) - T_0, \bar{v} = \frac{1}{1-\varepsilon_{xx}} \frac{d}{t} \quad (5.3a)$$

$$\text{Test II: } \Delta\bar{T} = \frac{1}{2}(T_{switch-on} + M_{stop}) - T_0, \bar{v} = -\frac{1}{1+\varepsilon_{xx}} \frac{d}{t} \quad (5.3b)$$

where  $T_{switch-off}$  is the temperature at which the heat gun is switched off,  $A_{stop}$  is the measured austenite stop temperature,  $T_{switch-on}$  is the temperature at which the heat gun is switched on, and  $M_{stop}$  is the measured martensite stop temperature;  $\varepsilon_{xx}$  is the strain of martensite near the A-M interface from the DIC image,  $d$  is the nominal distance of the A-M interface motion after the heat gun is switched off or on (see 75 s in Table 5-1 for an example), and  $t$  is the duration of the A-M interface motion after the heat gun is switched off or on (e.g.,  $t = 75 \text{ s} - 59 \text{ s} = 16 \text{ s}$  from Table 5-1).

For all the experimental data, Figure 5-7 summarises the values obtained using Equation (5.3). The average speed of the A-M interface motion, which is an absolute value less than 0.3 mm/s, may be observed in Figure 5-7 (nearly quasi-static). This is due to the fact that in Test I, the martensite-to-austenite transformation occurs at a temperature below  $A_s$  without the use of an external heat source to advance/speed up the transformation process. During Test II, the

austenite-to-martensite transformation occurs at temperatures above  $M_s$  without releasing the heat from the sample to advance/speed up the transformation process. It is also found from Figure 5-7 that the average driving force (quantified by the average temperature difference:  $\sim 4$  °C from the data in the 1st quadrant of Figure 5-7) for the martensite-to-austenite transformation is close to that ( $\sim -4.5$  °C from the 3rd quadrant of Figure 5-7) for the austenite-to-martensite transformation, which leads to the close average velocity of the A-M interface motion ( $0.1 \sim 0.3$  mm/s) for both transformations.

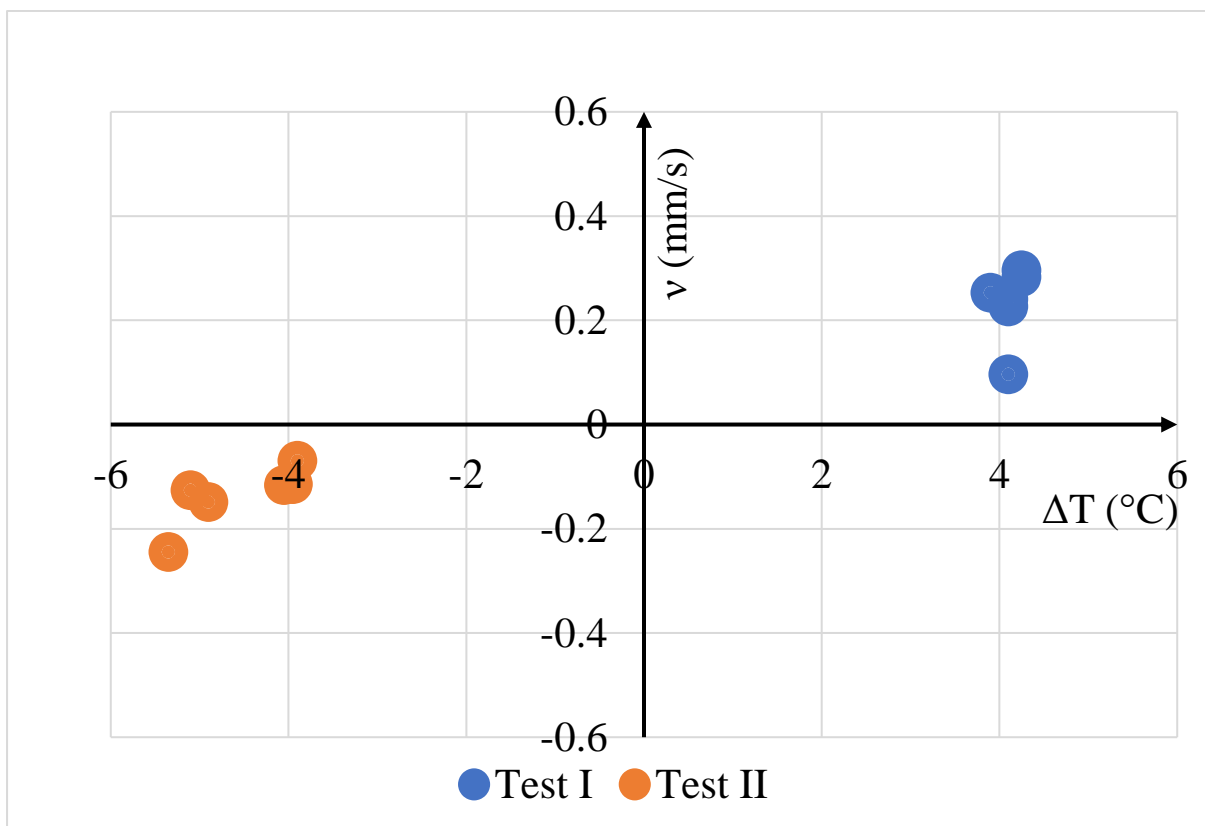


Figure 5-7. Average A-M interface motion speed at different levels of the average thermodynamic driving force, which is quantified by the average temperature difference here.

## 5.4. Chapter conclusion

This chapter experimentally studies the temperature-induced phase transformations of magnetic shape memory alloys. It is found from the experimental results that once the martensite-to-austenite (M-to-A) transformation is triggered when the Ni-Mn-Ga sample reaches the characteristic austenite start temperature  $A_s$ , martensite-to-austenite (M-to-A) transformation may continue at temperatures below  $A_s$ . This indicates that the nucleation temperature of austenite is greater than its propagation temperature. For the reverse austenite-to-martensite (M-to-A) transformation, once it is triggered by decreasing the sample temperature to the characteristic martensite start temperature  $M_s$ , the transformation can continue at temperatures above  $M_s$ . This also indicates that the nucleation temperature of the martensite phase is higher than its propagation temperature. Moreover, both transformations (i.e., M-to-A below  $A_s$  and A-to-M above  $M_s$ ) take place nearly quasi-statically with low velocity  $< 0.3$  mm/s.

## 6. Overall conclusion

This thesis has presented a study on single crystal Ni-Mn-Ga alloy through a combination of theoretical and experimental approaches. The goal of this study was to gain a deeper understanding of the behaviour of MSMA's under thermo-magnetic loading conditions and temperature-induced phase transformations.

The material model presented in this thesis has successfully revealed the complex relationship between thermo-magnetic loading conditions and single crystal Ni-Mn-Ga performance. The model provides valuable insights into the factors influencing the shape memory effect, which will allow engineers and researchers to optimise the design and functionality for various practical applications. Furthermore, analytical expressions of the material's stable temperature and stable output strain amplitude were presented that can offer a solid foundation for future advancements in the field, which could potentially lead to the development of novel single crystal NiMnGa-based devices and technologies. The experimental study on the other hand expands on the current knowledge of the kinetics of temperature-induced phase transformations in Ni-Mn-Ga MSMA's. The findings reveal crucial information about the underlying mechanisms governing the phase transformations, enabling researchers to better predict and control the material properties of MSMA's during phase transformation. This new understanding of temperature-induced phase transformations will enhance the current behaviour understanding of single crystal NiMnGa for numerous applications, including actuators, sensors, and energy harvesting devices.

In summary, this thesis has advanced the understanding of single crystal NiMnGa alloys by providing a comprehensive understanding of the behaviour and characteristics and will open research interest for further study and real-world applications.

## 7. Future work

The future work stemming from this thesis can be expanded and advanced in several key areas, which will further enhance the understanding of magnetic shape memory alloys and their applications:

- Investigate the effect of ambient heat transfer conditions on critical temperatures ( $A_{stop}$  and  $M_{stop}$ ): By exploring how varying heat transfer conditions impact the critical temperatures where phase transformations cease, researchers can gain a more comprehensive understanding of the factors influencing these transitions. This could lead to improved control over phase transformations, enabling more precise tuning of material properties and behaviour.
- In-depth analysis of temperature-induced phase transformation mechanisms: Further research into the underlying mechanisms responsible for temperature-induced phase transformations will help elucidate the relationships between the observed behaviour and the underlying material properties. This could lead to the development of more accurate models and predictive tools for FSMAs, ultimately improving their performance in various applications.
- Investigate the similarities between  $A_{stop}/M_{stop}$  behaviour and stress-strain curves for stress-induced phase transformations: By examining the parallels between temperature-induced phase transformations and stress-induced transformations, researchers can develop a more unified understanding of the various factors influencing the behaviour of shape memory alloys. This knowledge can be used to optimise material performance and tailor alloys for specific applications.
- Develop a finite element analysis (FEA) model based on the theoretical model: By creating an FEA model that incorporates the findings from the theoretical model, researchers can

simulate the behaviour of FSMA's under a broader range of conditions and geometries.

This would allow for more accurate predictions of material performance in complex, real-world scenarios, ultimately leading to more efficient and reliable FSMA-based devices.

By pursuing these avenues of research, the scientific community can deepen its understanding of magnetic shape memory alloys and their potential applications. This will pave the way for the development of more advanced, efficient, and reliable FSMA-based technologies in various industries.



## References

- Akintunde, A. R., Miller, K. S. & Schiavazzi, D. E. (2019). Bayesian inference of constitutive model parameters from uncertain uniaxial experiments on murine tendons. *Journal of the Mechanical Behavior of Biomedical Materials*, 96, 285–300.
- Aswathy, S., Narendrakumar, U. & Manjubala, I. (2020). Commercial hydrogels for biomedical applications. *Heliyon*, 6, e03719.
- Bhattacharya, K. (1992). Self-accommodation in martensite. *Archive for Rational Mechanics and Analysis*, 120, 201-244.
- Bin, F., Yi, L., Jing-Fang, D., Chao-Lun, W., Yong-Qin, C., Rong-Chang, Y. & Guang-Heng, W. (2010). Magnetic hysteresis and refrigeration capacity of Ni–Mn–Ga alloys near Martensitic transformation. *Chinese Physics B*, 19, 097501.
- Blaber, J., Adair, B. & Antoniou, A. (2015). Ncorr: Open-Source 2D Digital Image Correlation Matlab Software. *Experimental Mechanics*, 55.
- Bril, M., Fredrich, S. & Kurniawan, N. A. (2022). Stimuli-responsive materials: A smart way to study dynamic cell responses. *Smart Materials in Medicine*, 3, 257-273.
- Bronstein, E., Faran, E. & Shilo, D. (2019). Analysis of austenite-martensite phase boundary and twinned microstructure in shape memory alloys: The role of twinning disconnections. *Acta Materialia*, 164, 520-529.
- Bruno, N. M., Wang, S., Karaman, I. & Chumlyakov, Y. I. (2017). Reversible Martensitic Transformation under Low Magnetic Fields in Magnetic Shape Memory Alloys. *Scientific Reports*, 7, 40434.
- Buschow, K. H. J. (2013). *Handbook of Magnetic Materials*, Amsterdam, North Holland.
- Cao, W., Cudney, H. H. & Waser, R. (Year) Published. Smart materials and structures. Proceedings of the National Academy of Sciences, 1999. 8330–8331.
- Chen, X. & He, Y. (2020). Thermo-magneto-mechanical coupling dynamics of magnetic shape memory alloys. *International Journal of Plasticity*, 129, 102686.
- Chen, X., Moumni, Z., He, Y. & Zhang, W. (2014). A three-dimensional model of magneto-mechanical behaviors of martensite reorientation in ferromagnetic shape memory alloys. *Journal of the Mechanics and Physics of Solids*, 64, 249-286.
- Chmielus, M., Glavatsky, I., Hoffmann, J.-U., Chernenko, V. A., Schneider, R. & Müllner, P. (2011). Influence of constraints and twinning stress on magnetic field-induced strain of magnetic shape-memory alloys. *Scripta Materialia*, 64, 888-891.
- Chu, C. L., Hu, T., Wu, S. L., Dong, Y. S., Yin, L. H., Pu, Y. P., Lin, P. H., Chung, C. Y., Yeung, K. W. K. & Chu, P. K. (2007). Surface structure and properties of biomedical NiTi shape memory alloy after Fenton's oxidation. *Acta Biomaterialia*, 3, 795-806.
- Chulist, R., Straka, L., Lanska, N., Soroka, A., Sozinov, A. & Skrotzki, W. (2013). Characterization of mobile type I and type II twin boundaries in 10M modulated Ni–Mn–Ga martensite by electron backscatter diffraction. *Acta Materialia*, 61, 1913-1920.
- Duerig, T. W., Melton, K., Stockel, D. & Wayman, C. M. (1990). *Engineering aspects of shape memory alloys*, Butterworth-Heinemann Ltd.
- Faran, E. & Shilo, D. (2012). Implications of twinning kinetics on the frequency response in NiMnGa actuators. *Applied Physics Letters*, 100.
- Faran, E. & Shilo, D. (2016). Ferromagnetic Shape Memory Alloys – Challenges, Applications, and Experimental Characterization. *Experimental Techniques*, 40, 1005–1031.

- Fonteno, W. & Bilderback, T. (1993). Impact of hydrogel on physical properties of coarse-structured horticultural substrates. *Journal of the American Society for Horticultural Science*, 118, 217-222.
- Fuhg, J. N. & Bouklas, N. (2022). On physics-informed data-driven isotropic and anisotropic constitutive models through probabilistic machine learning and space-filling sampling. *Computer Methods in Applied Mechanics and Engineering*, 394, 114915.
- Ge, Y., Wang, H., Xue, J., Jiang, J., Liu, Z., Liu, Z., Li, G. & Zhao, Y. (2021). Programmable Humidity-Responsive Actuation of Polymer Films Enabled by Combining Shape Memory Property and Surface-Tunable Hygroscopicity. *ACS Applied Materials & Interfaces*, 13, 38773-38782.
- Grigorieva, V., Danilov, A. & Razov, A. (2015). Thermo-mechanical properties of an NiTi-shape memory alloy after dynamic loading. *Acta Physica Polonica A*, 128, 592-596.
- Guilemany, J. & Fernández, J. (1994). On the mechanism of two way shape memory effect obtained by stabilized stress induced martensite. *Scripta Metallurgica et Materialia;(United States)*, 30.
- Haldar, K. & Lagoudas, D. C. (2018). Dynamic magnetic shape memory alloys responses: Eddy current effect and Joule heating. *Journal of Magnetism and Magnetic Materials*, 465, 278-289.
- Haldar, K., Lagoudas, D. C. & Karaman, I. (2014). Magnetic field-induced martensitic phase transformation in magnetic shape memory alloys: modeling and experiments. *Journal of the Mechanics and Physics of Solids*, 69, 33-66.
- He, Y., Chen, X. & Moumni, Z. (2012). Reversible-strain criteria of ferromagnetic shape memory alloys under cyclic 3D magneto-mechanical loadings. *Journal of Applied Physics*.
- He, Y. J., Chen, X. & Moumni, Z. (2011). Two-dimensional analysis to improve the output stress in ferromagnetic shape memory alloys. *Journal of Applied Physics*.
- Heczko, O., Lanska, N., Soderberg, O. & Ullakko, K. (2002). Temperature variation of structure and magnetic properties of Ni–Mn–Ga magnetic shape memory alloys. *Journal of Magnetism and Magnetic Materials*, 242245, 1446-1449.
- Heczko, O. & Straka, L. (2004). Giant magneto-elastic strain-magnetic shape memory effect. *Czechoslovak Journal of Physics*, 54, 611-614.
- Heczko, O., Veřtát, P., Vronka, M., Kopecky, V. & Perevertov, O. (2016). Ni–Mn–Ga single crystal exhibiting multiple magnetic shape memory effects. *Shape Memory and Superelasticity*, 2, 272-280.
- Henry, C. P., Bono, D., Feuchtwanger, J., Allen, S. M. & O’Handley, R. C. (2002). ac field-induced actuation of single crystal Ni–Mn–Ga. *American Institute of Physics*, 91, 7810-7811.
- Herath, M., Epaarachchi, J., Islam, M., Fang, L. & Leng, J. (2020). Light activated shape memory polymers and composites: A review. *European Polymer Journal*, 136, 109912.
- Iqbal, D. & Samiullah, M. H. (2013). Photo-Responsive Shape-Memory and Shape-Changing Liquid-Crystal Polymer Networks. *Materials (Basel)*, 6, 116-142.
- Jain, M., Singh, S. & Cadeiras, M. (2013). A case of nitinol allergy causing pericardial tamponade. *Journal of Invasive Cardiology*, 25.
- Jetty, P., Jayaram, S. & Veinot, J. (2013). Superficial femoral artery nitinol stent in a patient with nickel allergy. *Journal of vascular surgery*, 58, 1388-1390.

- Jiang, C., Muhammad, Y., Deng, L., Wu, W. & Xu, H. (2004). Composition dependence on the martensitic structures of the Mn-rich NiMnGa alloys. *Acta Materialia*, 52, 2779-2785.
- Jugo, J., Feuchtwanger, J., Corres, J. & Etxebarria, V. (2018). Analysis of temperature effects in high accuracy ferromagnetic shape memory alloy actuators. *Sensors & Actuators: A. Physical*, 271, 174-181.
- Karaca, H., Basaran, B., Karaman, I. & Chumlyakov, Y. (2012). Stress-induced martensite to austenite phase transformation in Ni<sub>2</sub>MnGa magnetic shape memory alloys. *Smart materials and structures*, 21, 045011.
- Karaca, H., Karaman, I., Basaran, B., Lagoudas, D., Chumlyakov, Y. I. & Maier, H. (2007). On the stress-assisted magnetic-field-induced phase transformation in Ni<sub>2</sub>MnGa ferromagnetic shape memory alloys. *Acta materialia*, 55, 4253-4269.
- Karaca, H. E., Karaman, I., Basaran, B., Chumlyakov, Y. I. & Maier, H. J. (2006). Magnetic field and stress induced martensite reorientation in NiMnGa ferromagnetic shape memory alloy single crystals. *Acta Materialia*, 54, 233-245.
- Keplinger, C., Kaltenbrunner, M., Arnold, N. & Bauer, S. (2010). Röntgen's electrode-free elastomer actuators without electromechanical pull-in instability. *Proceedings of the National Academy of Sciences*, 107, 4505-4510.
- Kim, J.-h., Fukuda, T. & Kakeshita, T. (2006). A new phase induced in Ni<sub>2</sub>MnGa by uniaxial stress. *Scripta materialia*, 54, 585-588.
- Kim, T. A., Beiermann, B. A., White, S. R. & Sottos, N. R. (2016). Effect of mechanical stress on spiropyran-merocyanine reaction kinetics in a thermoplastic polymer. *ACS Macro letters*, 5, 1312-1316.
- Kim, Y.-J. & Matsunaga, Y. T. (2017). Thermo-responsive polymers and their application as smart biomaterials. *Journal of Materials Chemistry B*, 5, 4307-4321.
- Lahoz, R. & Puértolas, J. A. (2004). Training and two-way shape memory in NiTi alloys: influence on thermal parameters. *Journal of Alloys and Compounds*, 381, 130-136.
- Laitinen, V., Merabtene, M., Stevens, E., Chmielus, M., Van Humbeeck, J. & Ullakko, K. (2020). Additive Manufacturing from the Point of view of Materials Research. *Technical, Economic and Societal Effects of Manufacturing 4.0*, 43.
- Lexcellent, C., Leclercq, S., Gabry, B. & Bourbon, G. (2000). The two way shape memory effect of shape memory alloys: an experimental study and a phenomenological model. *International Journal of Plasticity*, 16, 1155-1168.
- Li, Y., Chen, H., Liu, D., Wang, W., Liu, Y. & Zhou, S. (2015). pH-Responsive Shape Memory Poly(ethylene glycol)-Poly( $\epsilon$ -caprolactone)-based Polyurethane/Cellulose Nanocrystals Nanocomposite. *ACS Applied Materials & Interfaces*, 7, 12988-12999.
- Li, Z., Zhang, Y., Esling, C., Zhao, X. & Zuo, L. (2011). Twin relationships of 5M modulated martensite in Ni-Mn-Ga alloy. *Acta Materialia*, 59, 3390-3397.
- Likhachev, A. A. & Ullakko, K. (2000). Magnetic-field-controlled twin boundaries motion and giant magneto-mechanical effects in Ni-Mn-Ga shape memory alloy. *Physical Letters A*, 275, 142-151.
- Liu, Y., Van Humbeeck, J., Stalmans, R. & Delaey, L. (1997). Some aspects of the properties of NiTi shape memory alloy. *Journal of alloys and compounds*, 247, 115-121.
- Liu, Z., Zhang, M., Cui, Y. T., Zhou, Y. Q., Wang, W., Wu, G., Zhang, X. & Xiao, G. (2003). Martensitic transformation and shape memory effect in ferromagnetic Heusler alloy Ni<sub>2</sub>FeGa. *Applied Physics Letters*, 82, 424-426.

- Lu, H., Leng, J. & Du, S. (2013). A phenomenological approach for the chemo-responsive shape memory effect in amorphous polymers. *Soft Matter*, 9, 3851-3858.
- Malard, B., Pilch, J., Sittner, P., Delville, R. & Curfs, C. (2011). In situ investigation of the fast microstructure evolution during electropulse treatment of cold drawn NiTi wires. *Acta Materialia*, 59, 1542-1556.
- Malik, A., Amberg, G., Borgenstam, A. & Ågren, J. (2013). Effect of external loading on the martensitic transformation – A phase field study. *Acta Materialia*, 61.
- Martynov, V. & Kokorin, V. (1992). The crystal structure of thermally- and stress-induced Martensites in Ni<sub>2</sub>MnGa single crystals. *Journal de Physique III*, 2, 739-749.
- Masdeu, F., Pons, J., Chumlyakov, Y. & Cesari, E. (2021). Two-way shape memory effect in Ni<sub>49</sub>Fe<sub>18</sub>Ga<sub>27</sub>Co<sub>6</sub> ferromagnetic shape memory single crystals. *Materials Science and Engineering: A*, 805, 140543.
- McFadden, M. E. & Robb, M. J. (2019). Force-dependent multicolor mechanochromism from a single mechanophore. *Journal of the American Chemical Society*, 141, 11388-11392.
- Melton, K. (1990). Ni-Ti based shape memory alloys. *Engineering aspects of shape memory alloys*, 344, 21-25.
- Miyazaki, S., Otsuka, K. & Wayman, C. (1989). The shape memory mechanism associated with the martensitic transformation in Ti • Ni alloys—I. Self-accommodation. *Acta Metallurgica*, 37, 1873-1884.
- Mogyl'nyy, G., Glavatskyy, I., Glavatska, N., Söderberg, O., Ge, Y. & Lindroos, V. (2003). Crystal structure and twinning in martensite of Ni<sub>1.96</sub>Mn<sub>1.18</sub>Ga<sub>0.86</sub> magnetic shape memory alloy. *Scripta materialia*, 48, 1427-1432.
- Mohd Jani, J., Leary, M., Subic, A. & Gibson, M. A. (2014). A review of shape memory alloy research, applications and opportunities. *Materials & Design (1980-2015)*, 56, 1078-1113.
- Müllner, P. (2019). Twinning stress of type I and type II deformation twins. *Acta Materialia*, 176, 211-219.
- Murray, S. J., Marioni, M., Allen, S. M., O'Handley, R. C. & Lograsso, T. A. (2000). 6% magnetic-field-induced strain by twin boundary motion in ferromagnetic Ni-Mn-Ga". *Applied Physics Letters*, 77, 886.
- Nath, H. & Phanikumar, G. (2015). Martensite transformation and magnetic properties of Ni-Fe-Ga Heusler alloys. *Metallurgical and Materials Transactions A*, 46, 4947-4955.
- Naumov, P., Chizhik, S., Panda, M. K., Nath, N. K. & Boldyreva, E. (2015). Mechanically Responsive Molecular Crystals. *Chemical Reviews*, 115, 12440-12490.
- Otsuka, K. & Ren, X. (2005). Physical metallurgy of Ti-Ni-based shape memory alloys. *Progress in Materials Science*, 50, 511-678.
- Pagounis, E., Chulist, R., Szczerba, M. J. & Laufenberg, M. (2014). High-temperature magnetic shape memory actuation in a Ni-Mn-Ga single crystal. *Scripta Materialia*, 83, 29-32.
- Pagounis, E., Szczerba, M., Chulist, R. & Laufenberg, M. (2015). Large magnetic field-induced work output in a NiMnGa seven-layered modulated martensite. *Applied Physics Letters*, 107, 152407.
- Panda, A. K., Ghosh, M., Kumar, A. & Mitra, A. (2008). Magnetic transitions and structure of a NiMnGa ferromagnetic shape memory alloy prepared by melt spinning technique. *Journal of Magnetism and Magnetic Materials*, 320, L116-L120.







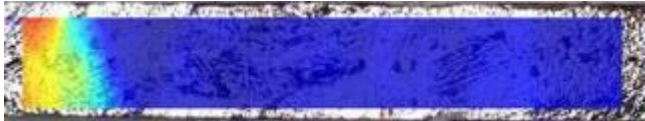
- Paranjape, H., Aycock, K., Bonsignore, C., Weaver, J., Craven, B. & Duerig, T. (2021). A probabilistic approach with built-in uncertainty quantification for the calibration of a superelastic constitutive model from full-field strain data. *Computational Materials Science*, 192, 110357.
- Pascan, O. Z., He, Y., Mounnia, Z. A. & Zhanga, W. H. (2015). Temperature rise of high-frequency martensite reorientation via Type II twin boundary motion in NiMnGa Ferromagnetic Shape Memory Alloy. *Scripta Materialia*, 104, 71-74.
- Pinneker, V., Gueltig, M., Sozinov, A. & Kohl, M. (2014). Single phase boundary actuation of a ferromagnetic shape memory foil. *Acta Materialia*, 64, 179-187.
- Pirge, G., Hyatt, C. & Altıntaş, S. (2004). Characterization of NiMnGa magnetic shape memory alloys. *Journal of materials processing technology*, 155, 1266-1272.
- Purwar, R. & Sachan, R. (2020). Thermoresponsive shape memory polymers for smart textiles. *Advances in Functional and Protective Textiles*. Elsevier.
- Qian, M., Zhang, X., Wei, L., Martin, P., Sun, J., Geng, L., Scott, T. B. & Peng, H.-X. (2018). Tunable Magnetocaloric Effect in Ni-Mn-Ga Microwires. *Scientific Reports*, 8, 16574.
- Righi, L., Albertini, F., Pareti, L., Paoluzi, A. & Calestani, G. (2007). Commensurate and incommensurate “5M” modulated crystal structures in Ni–Mn–Ga martensitic phases. *Acta Materialia*, 55, 5237-5245.
- Sabahi, N., Chen, W., Wang, C.-H., Kruzic, J. J. & Li, X. (2020). A Review on Additive Manufacturing of Shape-Memory Materials for Biomedical Applications. *JOM*, 72, 1229-1253.
- Sarvari, R., Keyhanvar, P., Agbolaghi, S., Gholami Farashah, M., Sadrhaghighi, A., Nouri, M. & Roshangar, L. (2020). Shape-memory materials and their clinical applications. *International Journal of Polymeric Materials and Polymeric Biomaterials*, 71, 315-335.
- Seiner, H., Straka, L. & Heczko, O. (2014). A microstructural model of motion of macro-twin interfaces in Ni–Mn–Ga 10M martensite. *Journal of the Mechanics and Physics of Solids*, 64, 198-211.
- Shahinpoor, M. (2015). *Ionic Polymer Metal Composites (Ipmcs) Set*, Cambridge, Royal Society of Chemistry.
- Snyder, E. A. & Tong, T. H. (2005). Towards Novel Light-Activated Shape Memory Polymer: Thermomechanical Properties of Photo-responsive Polymers. *MRS Proceedings*, 872, J18.6.
- Sozinov, A., Likhachev, A. A., Lanska, N. & Ullakko, K. (2002). Giant magnetic-field induced strain in NiMnGa seven-layered martensitic phase. *Applied Physics Letters*, 80, 1746-1748.
- Sratongon, P., Chernenko, V., Feuchtwanger, J. & Hosoda, H. (2019). Magnetic field-induced rubber-like behavior in Ni-Mn-Ga particles/polymer composite. *Scientific Reports*, 9.
- Straka, L., Heczko, O. & Hänninen, H. (2008). Activation of magnetic shape memory effect in Ni–Mn–Ga alloys by mechanical and magnetic treatment. *Acta Materialia*, 56, 5492-5499.
- Straka, L., Heczko, O. & Hannula, S.-P. (2006). Temperature dependence of reversible field-induced strain in Ni–Mn–Ga single crystal. *Scripta Materialia*, 54, 1497-1500.
- Straka, L., Soroka, A., Seiner, H., Hänninen, H. & Sozinov, A. (2012). Temperature dependence of twinning stress of Type I and Type II twins in 10M modulated Ni–Mn–Ga martensite. *Scripta Materialia*, 67, 25-28.

- Talbot, D. (2003). *Smart materials*, London, Institute of Materials, Minerals and Mining.
- Tan, H. & Elahinia, M. (2008). A nonlinear model for ferromagnetic shape memory alloy actuators. *Communications in Nonlinear Science and Numerical Simulation*, 13, 1917-1928.
- Tarng, W., Chen, C.-J., Lee, C.-Y., Lin, C.-M. & Lin, Y.-J. (2019). Application of virtual reality for learning the material properties of shape memory alloys. *Applied Sciences*, 9, 580.
- Techapiesancharoekij, R., Kostamo, J., Allen, S. M. & O'Handley, R. C. (2011). The effect of magnetic stress and stiffness modulus on resonant characteristics of Ni–Mn–Ga ferromagnetic shape memory alloy actuators. *Journal of Magnetism and Magnetic Materials*, 323, 3109-3116.
- Techapiesancharoekij, R., Kostamo, J., Allen, S. M. & O'Handley, R. C. (2009). Frequency response of acoustic-assisted Ni–Mn–Ga ferromagnetic-shapememory-alloy actuator. *American Institute of Physics*, 105, 093923.
- Thermocoupleinfo. (2011). *Thermocouple Accuracy Comparison Chart* [Online]. Thermocoupleinfo.com. Available: <https://www.thermocoupleinfo.com/thermocouple-accuracies.htm> [Accessed 26 September 2022].
- Thévenot, J., Oliveira, H., Sandre, O. & Lecommandoux, S. (2013). Magnetic responsive polymer composite materials. *Chemical Society Reviews*, 42, 7099.
- Tickle, R., James, R. D., Shield, T., Wuttig, M. & Kokorin, V. V. (1999). Ferromagnetic shape memory in the NiMnGa system. *IEEE Transactions on Magnetics*, 35, 4301–4310.
- Uchimali, M. & Vedantam, S. (2021). Modeling stress–strain response of shape memory alloys during reorientation of self-accommodated martensites with different morphologies. *Mechanics of Advanced Materials and Structures*, 1-9.
- Wang, F. E., Buehler, W. J. & Pickart, S. J. (1965). Crystal Structure and a Unique "Martensitic" Transition of TiNi. *Journal of Applied Physics*, 36, 3232-3239.
- Wang, J. & Du, P. (2019). Theoretical study and numerical simulations on the stress-induced twin interface nucleation in single-crystalline NiMnGa alloys. *Journal of Applied Physics*, 126, 115101.
- Wang, T., Farajollahi, M., Choi, Y., Lin, I., Marshall, J., Thompson, N., Kar-Narayan, S., Madden, J. & Smoukov, S. (2016). Electroactive polymers for sensing. *Interface Focus*, 6, 20160026.
- Wang, Y., Wang, Y., Wei, Q. & Zhang, J. (2022). Light-responsive shape memory polymer composites. *European Polymer Journal*, 173, 111314.
- Webster, P. J., Ziebeck, K. R. A., Town, S. L. & Peak, M. S. (1984). Magnetic order and phase transformation in Ni<sub>2</sub>MnGa. *Philosophical Magazine B* 49, 295–310.
- Wei, Z., Sandström, R. & Miyazaki, S. (1998). Shape-memory materials and hybrid composites for smart systems: Part I Shape-memory materials. *Journal of materials science*, 33, 3743-3762.
- Wen, C., Yu, X., Zeng, W., Zhao, S., Wang, L., Wan, G., Huang, S., Grover, H. & Chen, Z. (2018). Mechanical behaviors and biomedical applications of shape memory materials: A review. *AIMS Materials Science*, 5, 559-590.
- Wuttig, M., Li, J. & Craciunescu, C. (2001). A new ferromagnetic shape memory alloy system. *Scripta materialia*, 44, 2393-2397.
- Xie, X. (2022). Phase field-finite element analysis of magnetic-induced deformation in ferromagnetic shape memory alloy. *Computational Materials Science*, 210, 111454.


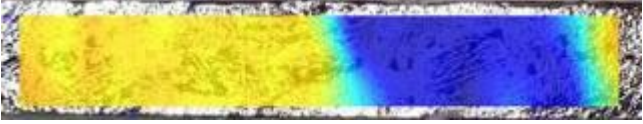
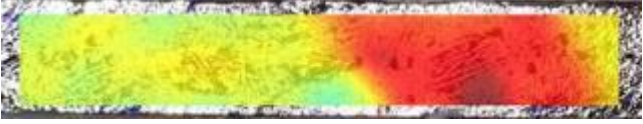

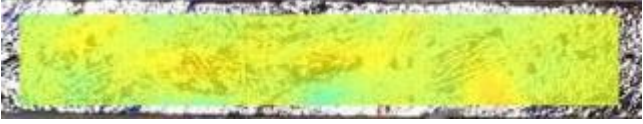



- Yahia, H. (2015). *Shape memory polymers for biomedical applications*, Cambridge, UK, Woodhead Publishing.
- Yang, Q., Zheng, W., Zhao, W., Peng, C., Ren, J., Yu, Q., Hu, Y. & Zhang, X. (2019). One-way and two-way shape memory effects of a high-strain cis-1,4-polybutadiene–polyethylene copolymer based dynamic network via self-complementary quadruple hydrogen bonding. *Polymer Chemistry*, 10, 718-726.
- Yu, C., Chen, T., Yin, H., Kang, G. & Fang, D. (2020). Modeling the anisotropic elastocaloric effect of textured NiMnGa ferromagnetic shape memory alloys. *International Journal of Solids and Structures*, 191-192, 509-528.
- Yu, C., Kang, G. & Fang, D. (2018). A Thermo-Magneto-Mechanically Coupled Constitutive Model of Magnetic Shape Memory Alloys. *Acta Mechanica Solida Sinica*, 31.
- Zasimchuk, I. K., Kokorin, V., Martynov, V., Tkachenko, A. & Chernenko, V. A. (1990). Crystal structure of martensite in heusler alloy Ni<sub>2</sub>MnGa. *Physics of Metals and Metallography*, 69, 104-108.
- Ze, Q., Kuang, X., Wu, S., Wong, J., Montgomery, S., Zhang, R., Kovitz, J., Yang, F., Qi, H. & Zhao, R. (2019). Magnetic Shape Memory Polymers with Integrated Multifunctional Shape Manipulation. *Advanced Materials*, 32, 1906657.
- Zhang, S. (2018). *High Frequency Magnetic Field-induced Strain of Ferromagnetic Shape Memory Alloys*. PhD, Paris-Saclay University.
- Zhang, S., Chen, X., Moumni, Z. & He, Y. (2018a). Thermal effects on high-frequency magnetic-field-induced martensite reorientation in ferromagnetic shape memory alloys: an experimental and theoretical investigation. *International Journal of Plasticity*, 108, 1–20.
- Zhang, S., Chen, X., Moumni, Z. & He, Y. (2018b). Coexistence and compatibility of martensite reorientation and phase transformation in high-frequency magnetic-field-induced deformation of Ni-Mn-Ga single crystal. *International Journal of Plasticity*, 110, 110–122.
- Zhang, S., Qin, G. & He, Y. (2020). Ambient effects on the output strain of Ni-Mn-Ga single crystal magnetic shape memory alloy. *Journal of Alloys and Compounds*, 835, 155159.
- Zhu, Y. & Dui, G. (2007). Micromechanical modeling of the stress-induced superelastic strain in magnetic shape memory alloy. *Mechanics of Materials*, 39, 1025-1034.




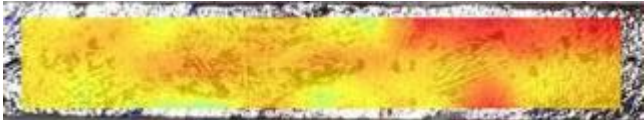
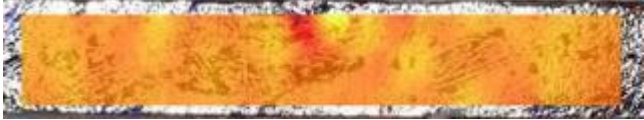
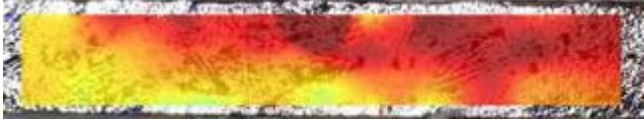


## Appendix






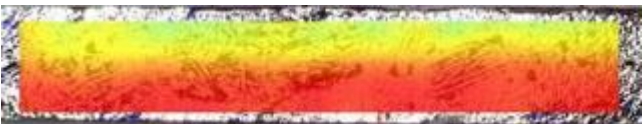

### Appendix A. Measurement of characteristic phase transformation temperatures of Ni-Mn-Ga single crystal

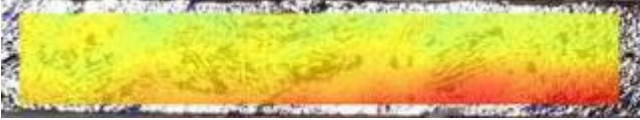







Time	Sample temperature	DIC images on the $x$ - $y$ plane
0 s	28.0 °C	<p>Colour bar</p>  <p>Scale bar</p> <p>10mm</p>  <p><math>\epsilon_{xx}</math></p>  <p><math>\epsilon_{yy}</math></p> 
143 s	40.3 °C ( $A_s$ )	<p><math>\epsilon_{xx}</math></p>  <p><math>\epsilon_{yy}</math></p> 
151 s	40.5 °C	<p><math>\epsilon_{xx}</math></p> 

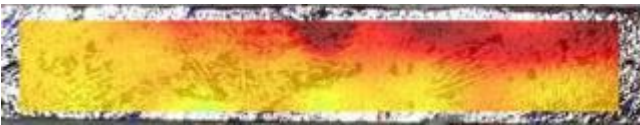





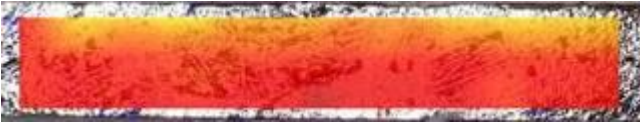



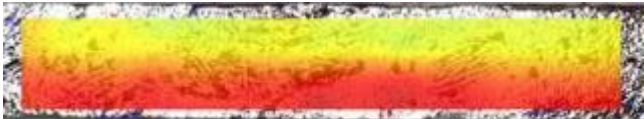

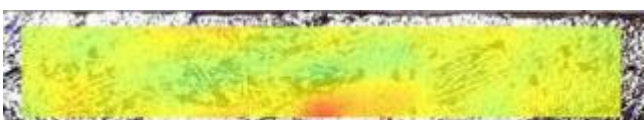




Time	Sample temperature	DIC images on the $x$ - $y$ plane
		$\epsilon_{yy}$ 
182 s	39.9 °C	$\epsilon_{xx}$  $\epsilon_{yy}$ 
213 s	41.0 °C ( $A_f$ )	$\epsilon_{xx}$  $\epsilon_{yy}$ 
391 s	55.9 °C	$\epsilon_{xx}$  $\epsilon_{yy}$ 
640 s	33.5 °C ( $M_s$ )	$\epsilon_{xx}$ 


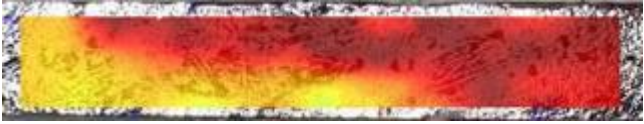

Time	Sample temperature	DIC images on the $x$ - $y$ plane
		 <p data-bbox="676 434 711 465"><math>\epsilon_{xx}</math></p> 
645 s	33.4 °C	<p data-bbox="676 667 711 698"><math>\epsilon_{xx}</math></p>  <p data-bbox="676 898 711 929"><math>\epsilon_{yy}</math></p> 
663 s	33.7 °C	<p data-bbox="676 1131 711 1162"><math>\epsilon_{xx}</math></p>  <p data-bbox="676 1361 711 1393"><math>\epsilon_{yy}</math></p> 
741 s	33.2 °C ( $M_f$ )	<p data-bbox="676 1594 711 1626"><math>\epsilon_{xx}</math></p>  <p data-bbox="676 1825 711 1856"><math>\epsilon_{yy}</math></p> 

Time	Sample temperature	DIC images on the $x$ - $y$ plane
<b>Experimental cycle 2</b>		
1457 s	26.3 °C	$\epsilon_{xx}$  $\epsilon_{yy}$ 
1587 s	39.3 °C ( $A_s$ )	$\epsilon_{xx}$  $\epsilon_{yy}$ 
1616 s	39.3 °C	$\epsilon_{xx}$  $\epsilon_{yy}$ 
1631 s	39.4 °C	$\epsilon_{xx}$  $\epsilon_{yy}$

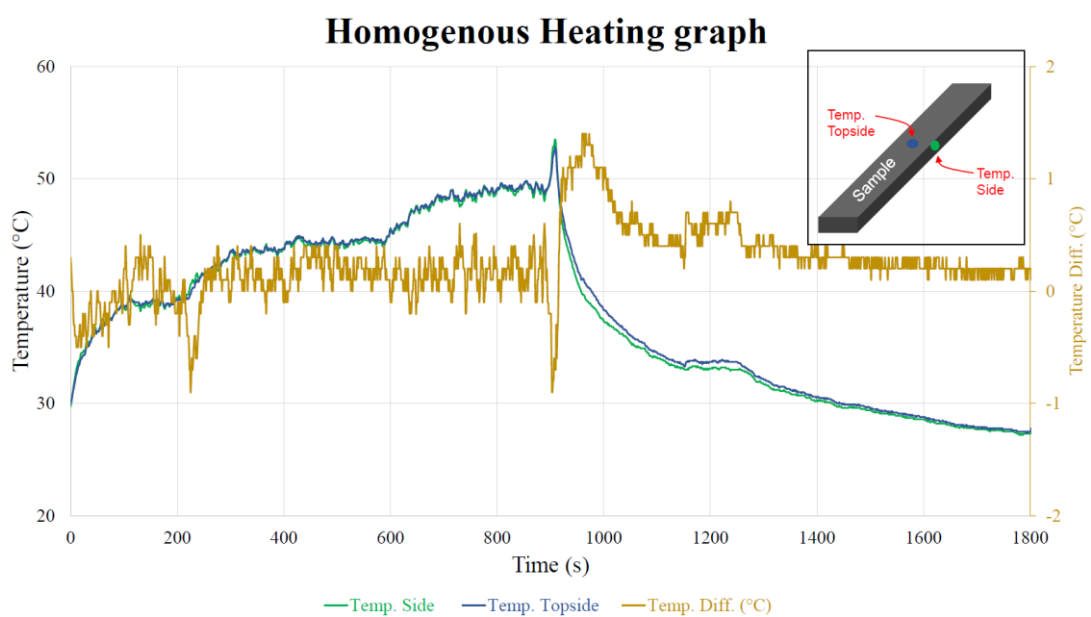
Time	Sample temperature	DIC images on the $x$ - $y$ plane
		
1662 s	42.3 °C ( $A_f$ )	<p data-bbox="678 434 715 461"><math>\epsilon_{xx}</math></p>  <p data-bbox="678 667 715 694"><math>\epsilon_{yy}</math></p> 
1864 s	56 °C	<p data-bbox="678 896 715 922"><math>\epsilon_{xx}</math></p>  <p data-bbox="678 1126 715 1153"><math>\epsilon_{yy}</math></p> 
2106 s	33.7 °C ( $M_s$ )	<p data-bbox="678 1357 715 1384"><math>\epsilon_{xx}</math></p>  <p data-bbox="678 1588 715 1615"><math>\epsilon_{yy}</math></p> 
2115 s	33.5 °C	<p data-bbox="678 1818 715 1845"><math>\epsilon_{xx}</math></p> 

Time	Sample temperature	DIC images on the $x$ - $y$ plane
		$\epsilon_{yy}$ 
2231 s	33.0 °C ( $M_f$ )	$\epsilon_{xx}$  $\epsilon_{yy}$ 
2719 s	27.6 °C	$\epsilon_{xx}$  $\epsilon_{yy}$ 
<i>Experiment cycle 3</i>		
2828 s	40.0 °C ( $A_s$ )	$\epsilon_{xx}$  $\epsilon_{yy}$ 
2835 s	39.8 °C	$\epsilon_{xx}$







Time	Sample temperature	DIC images on the $x$ - $y$ plane
		 $\epsilon_{yy}$ 
2870 s	41.5 °C ( $A_f$ )	$\epsilon_{xx}$  $\epsilon_{yy}$ 
3168 s	55.1 °C	$\epsilon_{xx}$  $\epsilon_{yy}$ 
3440 s	33.7 °C ( $M_s$ )	$\epsilon_{xx}$  $\epsilon_{yy}$ 

Time	Sample temperature	DIC images on the $x$ - $y$ plane
3475	33.9 °C	$\epsilon_{xx}$  $\epsilon_{yy}$ 
3546	33.4 °C ( $M_f$ )	$\epsilon_{xx}$  $\epsilon_{yy}$





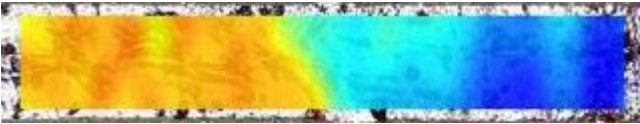

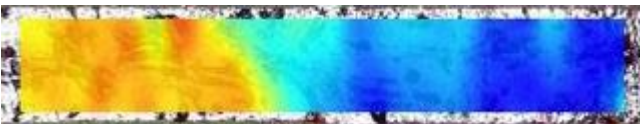

## Appendix B. Sample temperature measured by thermocouples at different locations

















**Appendix C. Experimental data for temperature-induced phase transformation in Ni-Mn-Ga single crystal**








Time	Sample temperature	DIC images on the $x$ - $y$ plane
0 s	65.8 °C	<p>Colour bar</p>  <p>Scale bar</p>  <p><math>\epsilon_{xx}</math></p>  <p><math>\epsilon_{yy}</math></p> 
83 s	45.0 °C	<p><math>\epsilon_{xx}</math></p>  <p><math>\epsilon_{yy}</math></p> 
229 s	39.2 °C ( $M_s$ )	<p><math>\epsilon_{xx}</math></p>






Time	Sample temperature	DIC images on the $x$ - $y$ plane
		 $\epsilon_{yy}$ 
262 s	39.0 °C	$\epsilon_{xx}$  $\epsilon_{yy}$ 
282 s	38.5 °C (switched on heat gun)	$\epsilon_{xx}$  $\epsilon_{yy}$ 
285 s	38.2 °C	$\epsilon_{xx}$  $\epsilon_{yy}$ 

Time	Sample temperature	DIC images on the $x$ - $y$ plane
292 s	39.0 °C	$\epsilon_{xx}$  $\epsilon_{yy}$ 
296 s	41.1 °C	$\epsilon_{xx}$  $\epsilon_{yy}$ 
298 s	43.0 °C ( $M_{stop}$ )	$\epsilon_{xx}$  $\epsilon_{yy}$ 
324 s	50.1 °C	$\epsilon_{xx}$  $\epsilon_{yy}$

Time	Sample temperature	DIC images on the $x$ - $y$ plane
		
<b>Experiment cycle 2</b>		
400 s	66.4°C (Power switch off)	$\epsilon_{xx}$  $\epsilon_{yy}$ 
664 s	39.1 °C ( $M_s$ )	$\epsilon_{xx}$  $\epsilon_{yy}$ 
703 s	39.1 °C (Power switched on)	$\epsilon_{xx}$  $\epsilon_{yy}$ 

Time	Sample temperature	DIC images on the $x$ - $y$ plane
726 s	43.2°C ( $M_{stop}$ )	$\epsilon_{xx}$  $\epsilon_{yy}$ 
<b>Experiment cycle 3</b>		
828 s	65.8 °C (Power switched off)	$\epsilon_{xx}$  $\epsilon_{yy}$ 
1107 s	38.9 °C ( $M_s$ )	$\epsilon_{xx}$  $\epsilon_{yy}$ 
1153 s	38.5 °C (Power switched off)	$\epsilon_{xx}$  $\epsilon_{yy}$

Time	Sample temperature	DIC images on the $x$ - $y$ plane
		
1188 s	43.2 °C ( $M_{stop}$ )	<p data-bbox="676 434 715 465"><math>\epsilon_{xx}</math></p>  <p data-bbox="676 667 715 698"><math>\epsilon_{yy}</math></p> 

## Appendix D. Algorithmic chart

